UCRL-TH-211400

LAWRENCE
LIVERMORE
NATIONAL
LABORATORY

Spin Distribution in Preequilibrium Reactions for ^{48}Ti + n

Dugersuren Dashdorj

April 12, 2005

A dissertation submitted to the Graduate Faculty of North Carolina State University, Raleigh, North Carolina

Disclaimer

This document was prepared as an account of work sponsored by an agency of the United States Government. Neither the United States Government nor the University of California nor any of their employees, makes any warranty, express or implied, or assumes any legal liability or responsibility for the accuracy, completeness, or usefulness of any information, apparatus, product, or process disclosed, or represents that its use would not infringe privately owned rights. Reference herein to any specific commercial product, process, or service by trade name, trademark, manufacturer, or otherwise, does not necessarily constitute or imply its endorsement, recommendation, or favoring by the United States Government or the University of California. The views and opinions of authors expressed herein do not necessarily state or reflect those of the United States Government or the University of California, and shall not be used for advertising or product endorsement purposes.

Auspices Statement

This work was supported in part by the Stewardship Science Academic Alliances Program, National Nuclear Security Administration of the U. S. Department of Energy Grants No. DE-FG03-03NA00076 and No. DE-FG02-97-ER41042 at North Carolina State University, and in part under the auspices of the U.S. Department of Energy by University of California, Lawrence Livermore National Laboratory and Los Alamos National Laboratory under Contracts W-7405-Eng-48 and W-7405-ENG-36. This work has benefited from the use of the Los Alamos Neutron Science Center at the Los Alamos National Laboratory. This facility is funded by the U. S. Department of Energy under contract No. W-7405-ENG-36.

DASHDORJ, DUGERSUREN. Spin Distribution in Preequilibrium Reactions for ^{48}Ti + n. (Under the direction of Dr. G. E. Mitchell and Dr. P. E. Garrett)

Cross section measurements were made of prompt γ-ray production as a function of incident neutron energy on a ^{48}Ti sample. Partial γ-ray cross sections for transitions in $^{45-48}$Ti, $^{44-48}$Sc, and $^{42-45}$Ca have been determined. Energetic neutrons were delivered by the Los Alamos National Laboratory spallation neutron source located at the LANSCE/WNR facility. The prompt-reaction γ rays were detected with the large-scale Compton-suppressed germanium array for neutron induced excitations (GEANIE). Neutron energies were determined by the time-of-flight technique. The γ-ray excitation functions were converted to partial γ-ray cross sections taking into account the dead-time correction, target thickness, detector efficiency and neutron flux (monitored with an in-line fission chamber). The data are presented for neutron energies E_n between 1 to 200 MeV. These results are compared with model calculations which include compound nuclear and preequilibrium emission. The model calculations are performed using the STAPRE reaction code for E_n up to 20 MeV and the GNASH reaction code for E_n up to 120 MeV. Using the GNASH reaction code the effect of the spin distribution in preequilibrium reactions has been investigated. The preequilibrium reaction spin distribution was calculated using the quantum mechanical theory of Feshbach, Kerman, and Koonin (FKK). The multistep direct (MSD) part of the FKK theory was calculated for a one-step process. The contribution from higher steps is estimated to be small. The spin distribution of the multistep compound (MSC) part of FKK theory is assumed to be the same as in the compound nucleus. The FKK preequilibrium spin distribution was incorporated into the GNASH calculations and the γ-ray production cross sections were calculated and compared with experimental data. The difference in the partial γ-ray cross sections using spin distributions with and without preequilibrium effects is found to be significant. Specifically, the probability of γ transitions from a high spin state is strongly suppressed because of the preequilibrium spin distribution. Preequilibrium reactions are found to be important for neutron energies above 10 MeV.

SPIN DISTRIBUTION IN PREEQUILIBRIUM REACTIONS FOR ^{48}Ti + n

by

DUGERSUREN DASHDORJ

A dissertation submitted to the Graduate Faculty of

North Carolina State University

in partial fulfillment of the

requirements for the Degree of

Doctor of Philosophy

Department of Physics

Raleigh

2005

APPROVED BY:

Mohamed A. Bourham

John H. Kelley

Gary E. Mitchell,
Co-chair of Advisory Committee

Paul E. Garrett,
Co-chair of Advisory Committee

Dedicated to my wife Undraa and son Baljinnyam

Biography

Dugersuren Dashdorj

Personal information

Born 10 March, 1972, Govi-Altai, Mongolia

Married with Undraa Agvaanluvsan, son Baljinnyam

Education

M.S. in Physics - 2002, North Carolina State University, USA

B.S. in Physics - 1994, National University of Mongolia, Mongolia

Awards and Honors

Recognition of Excellence, National Nuclear Security Administration, Department of Energy, Albuquerque, NM, March 2004

Travel award to participate in the 6-th LANSCE User Group meeting, LANL, Los Alamos, New Mexico, 2003

Professional Experience

Graduate Research Assistant, North Carolina State University,
January 2003 to present

Graduate Teaching Assistant, North Carolina State University,
August 2000 to January 2003

Research Assistant, Triangle Universities Nuclear Laboratory,
May 1999 to August 2000

Publications

^{48}Ti (n,xnp$\alpha\gamma$) reaction cross sections using spallation neutrons for E_n = 1 - 20 MeV D. Dashdorj, G. E. Mitchell, P. E. Garrett, U. Agvaanluvsan, J. A. Becker, L. A. Bernstein, J. R. Cooper, R. D. Hoffman, R. Macri, and W. Younes, Technical Report, UCRL-TR-209474.

High-Spin Rotational Structures in ^{76}Kr J.J. Valiente-Dobon, et al., Phys. Rev. C **71**, 034311 (2005).

Lifetimes of high-spin states in ^{76}Kr J.J. Valiente-Dobon et al., Acta Physica Polonica B **36**, 1339 (2005).

Production of a ^{76}Kr radioactive ion beam using a batch mode method J. R. Cooper, L. Bernstein, M. A. McMahan, J. Powell, D. Wutte, L. Ahle, N. Benczer-Koller, D. Dashdorj, G. Kumbartzki, T. J. Mertzimekis, A. Shiller, C. Silver, M. J. Taylor, Nuclear Instruments and Methods in Physics Research A553, 287-294 (2004).

^{48}Ti(n,xnypz$\alpha\gamma$) reactions for neutron energies up to 250 MeV D. Dashdorj, et al., In proceedings of International Conference on Nuclear Data ND2004, Santa Fe, NM, September 26 - October 1, 2004.

Schools and Workshops

The Second RIA Summer School August 2003, National Superconducting Cyclotron Labortory, Michigan State University, East Lansing, MI

Nuclear Reactions on Unstable Nuclei and the Surrogate Reaction Technique workshop January 12-15 2004, Asilomar Conference Grounds, Pacific Grove, CA

Acknowledgments

I am indebted to many people for making this dissertation possible. I owe a debt of gratitude to my adviser Prof. Gary E Mitchell for his guidance and support throughout the term of my PhD study. I am grateful for his wisdom, encouragement and for giving me an opportunity to work at the national laboratories. I gratefully thank my co-adviser Prof. Paul E Garrett for teaching me everyday jargon of nuclear physics and for many useful comments, advice, and his enthusiasm.

I would like to thank my other committee members Prof. Mohamed Bourham and Prof. John Kelley for kindly agreeing to serve on my thesis committee. I am deeply thankful to Dr. Walid Younes for his time and many helpful discussions. The analysis codes professionally written by Dr. Younes were extremely valuable for my data analysis. I would like to thank Dr. John Becker for his involvement in my research and for his advice and wisdom.

It has been a great privilege to work among scientists of N division at Lawrence Livermore National Laboratory. I want to thank all the members of the Experimental Nuclear Physics Group led by Dr. Rick Norman for hosting my graduate study. Their hospitality and friendly environment made my dissertation research both educational and enjoyable. I also would like to thank Dr. Rob Hoffman and Kevin Kelley for providing the theoretical calculation using the STAPRE code.

Many thanks are due to my collaborators Dr. Ron Nelson, Dr. Nick Fotiadis, and Dr. Matt Devlin at GEANIE group of the Los Alamos National Laboratory. I would like to express my gratitude to Dr. Toshihiko Kawano of Theoretical Group of LANL for his theoretical guidance, and Dr. Jerry Wilhelmy for his insights.

I would like to thank my family (in Mongolian). Hairt aav S. Dugersuren, eej Z. Lhamsuren bolon duu Purevjav, Dolgorsuren, Damdintsogt, Zagd-Ochir, Ichinhorloo nartaa nadad huleelgesen ih itgel naidvar, hair, demjlegt tani setgeliin ugaas bayarlaj baina. Mon

avga ah S. Jigjidsuren bolon tuunii ger bul, hadam aav agsan B. Agvaanluvsan, hadam eej B. Battogtokh, duu Hudree, Idree, Indraa nartaa bolon busad torol torogsod, erdemten bagsh nar, naiz nuhudduu erdemten boloh zamd mini uzuulsen huvi nemer, amjilt buteeliig mini chin setgeleesee huvaaltssand gun talarhalaa ilerhiilie.

I wish to thank my son Baljinnyam for his loving support and his independence. Thank you for making delicious dinners during my busy time working on the dissertation. I love you. Last but not least, I would like to thank my dear, lovely wife Undraa Agvaanluvsan, for everything she is and for making my life full.

This work was supported in part by the Stewardship Science Academic Alliances Program, National Nuclear Security Administration of the U. S. Department of Energy Grants No. DE-FG03-03NA00076 and No. DE-FG02-97-ER41042. This work was performed under the auspices of the U. S. Department of Energy by University of California, Lawrence Livermore National Laboratory and Los Alamos National Laboratory under contracts No. W-7405-ENG-48 and W-7405-ENG-36. This work has benefited from the use of the Los Alamos Neutron Science Center at the Los Alamos National Laboratory. This facility is funded by the U. S. Department of Energy under contract No. W-7405-ENG-36.

Contents

List of Tables **x**

List of Figures **xi**

Chapter 1 Introduction **1**

Chapter 2 Theoretical Background **5**

2.1 Introduction 5

2.2 Direct reactions 5

2.2.1 The phenomenological optical model 6

2.3 Compound nucleus reactions 9

2.3.1 Hauser-Feshbach theory 10

2.3.2 The width fluctuation correction 12

2.3.3 Nuclear level densities 15

2.3.4 γ-ray strength functions 17

2.4 Preequilibrium reactions 21

2.4.1 The exciton model 22

2.4.2 Feshbach, Kerman, and Koonin theory 26

2.4.3 Multistep compound reactions 27

2.4.4 Multistep direct reactions 31
2.4.5 Spin effects of the preequilibrium reactions 33

Chapter 3 Experimental Technique **37**

3.1 Measurement of prompt γ rays from neutron-induced reactions 37
3.2 Experimental devices 38
3.2.1 γ-ray detectors 39
3.2.2 The GEANIE array 41
3.2.3 Electronics and data acquisition system 44
3.3 Summary of experimental details 46

Chapter 4 Data Analysis Overview **51**

4.1 Introduction 51
4.2 Time-of-flight technique 52
4.3 Analysis of γ-ray spectra 55
4.3.1 Peak-shape and background fit parameters 55
4.3.2 Efficiency of Ge detectors 56
4.3.3 Beam-on γ-ray calibration 58
4.4 Extraction of the excitation functions 63
4.5 Analysis of $\gamma\gamma$ matrix 69
4.6 Threshold analysis 72
4.7 Iron line analysis 75
4.8 Doppler effects 75

Chapter 5 Theoretical Model Calculations **80**

5.1 Hauser-Feshbach statistical model 80
5.2 The STAPRE reaction code 82
5.2.1 Transmission coefficients 82
5.2.2 Width fluctuation corrections 87

5.2.3 Preequilibrium processes 89

5.3 The GNASH reaction code 91

5.3.1 Transmission coefficients 91

5.3.2 Width fluctuation corrections 93

5.3.3 Preequilibrium reactions 93

Chapter 6 Experimental results **96**

6.1 Channel cross sections of ^{48}Ti + n reactions for E_n = 1 to 20 MeV 96

6.1.1 Partial γ-ray cross sections for E_n = 1 to 20 MeV 96

6.1.2 Calculations using the STAPRE reaction code 96

6.1.3 Lower-limit estimates 97

6.1.4 Channel cross sections combined with Hauser-Feshbach model calculations 102

6.2 Partial γ-ray cross sections for E_n = 1 to 200 MeV 103

6.3 Spin distribution of the preequilibrium reactions 116

Chapter 7 Summary **129**

7.1 Conclusion 129

Bibliography **131**

Chapter A Partial γ ray cross sections **137**

List of Tables

3.1 Experimental details 49

3.2 Experimental details with iron foils 50

4.1 Planar-spectrum fit parameters 57

4.2 Coaxial-spectrum fit parameters 58

4.3 Beam-on γ rays used in the calibration of planar data 59

4.4 Beam-on γ rays used in the calibration of coaxial data 61

4.5 Reaction Q values and thresholds 74

6.1 Systematic uncertainties 102

List of Figures

2.1 Schematic representation of a reaction in the exciton model. 24

2.2 Multistep description of a nuclear reaction. 28

3.1 Coax detector surrounded by a Compton suppression system 42

3.2 Schematic diagram of the experimental setup 43

3.3 GEANIE detector circuit diagram 45

3.4 GEANIE beam RF circuit diagram 47

3.5 The flow of data 48

4.1 Time-of-flight spectrum 53

4.2 Coaxial-data sum spectrum 54

4.3 Fit to planar-data sum spectrum 56

4.4 Efficiency curve for planar detectors 59

4.5 Efficiency curve for coaxial detectors 61

4.6 γ-ray calibration curves for planar data 64

4.7 γ-ray calibration curves for coaxial data 65

4.8 Time-of-flight spectrum for fission chamber 67

4.9 Schematic diagram of $\gamma\gamma$ coincidence system 70

4.10 $\gamma\gamma$ coincidence spectra 71

4.11 Partial level scheme for ^{48}Ti. 73
4.12 Partial γ-ray cross section for ^{56}Fe transition measured in the planar detectors 76
4.13 Partial γ-ray cross section for ^{56}Fe transition measured in the coax detectors 77
4.14 Doppler effects on 943-keV transition 78

5.1 Schematic illustration of the energetics of reaction sequences 81
5.2 Adopted level scheme of ^{48}Ti for the STAPRE calculation 87
5.3 Adopted level scheme of ^{47}Ti for the STAPRE calculation 88
5.4 Adopted level scheme of ^{48}Sc for the STAPRE calculation 89
5.5 Adopted level scheme of ^{45}Ca for the STAPRE calculation 90

6.1 Lower limit for the ^{48}Ti(n,n$'\gamma$)^{48}Ti reaction cross section 98
6.2 Lower limit for the ^{48}Ti(n,2nγ)^{47}Ti reaction cross section 99
6.3 Lower limit for the ^{48}Ti(n,pγ)^{48}Sc reaction cross section 100
6.4 Lower limit for the ^{48}Ti(n,$\alpha\gamma$)^{45}Ca reaction cross section 101
6.5 Deduced channel cross section for the ^{48}Ti(n,n$'$)^{48}Ti reaction. 104
6.6 Deduced channel cross section for the ^{48}Ti(n,2n)^{47}Ti reaction. 105
6.7 Deduced channel cross section for the ^{48}Ti(n,p)^{48}Sc reaction. 106
6.8 Deduced channel cross section for the ^{48}Ti(n,α)^{45}Ca reaction. 107
6.9 Partial cross sections for E_γ = 983-keV, 1437-keV, 2421-keV, and 3737-keV transitions compared with GNASH prediction 109
6.10 Partial cross sections for E_γ = 159-keV, 1285-keV, 1825-keV, and 2260-keV transitions in ^{47}Ti 110
6.11 Partial cross sections for E_γ = 889-keV, 1120-keV transitions in ^{46}Ti and E_γ = 293-keV, 414-keV transitions in ^{45}Ti 111
6.12 Partial cross sections for E_γ = 121-keV, 131-keV, 371-keV, and 520-keV transitions in ^{48}Sc 113
6.13 Partial cross sections for E_γ = 808-keV, 1404-keV transitions in ^{47}Sc and E_γ = 228-keV, 295-keV transitions in ^{46}Sc 114

6.14 Partial cross sections for E_γ = 543-keV, 1056-keV transitions in ^{45}Sc and E_γ = 235-keV, 350-keV transitions in ^{44}Sc 115
6.15 Partial cross sections for E_γ = 174-keV transition in ^{45}Ca and E_γ = 1126-keV, 1157-keV transitions in ^{44}Ca 117
6.16 Partial cross sections for E_γ = 373-keV, 1021-keV transitions in ^{43}Ca and E_γ = 437-keV, 1525-keV transitions in ^{42}Ca 118
6.17 Dependence of spin distribution on outgoing neutron energy of 3 MeV. . . . 120
6.18 Dependence of spin distribution on outgoing neutron energy of 7 MeV. . . . 120
6.19 Dependence of spin distribution on outgoing neutron energy of 9 MeV. . . . 120
6.20 Dependence of spin distribution on outgoing neutron energy of 15 MeV. . . 120
6.21 Spin cut-off parameters 121
6.22 Partial cross section for 2^+ to 0^+ transition in yrast band of ^{48}Ti. 123
6.23 Partial cross section for 4^+ to 2^+ transition in yrast band of ^{48}Ti. 124
6.24 Partial cross section for 6^+ to 4^+ transition in yrast band of ^{48}Ti. 125
6.25 Partial cross section for $7/2^-$ to $5/2^-$ transition in ^{47}Ti. 126
6.26 Ratio of the partial cross section for 4^+ to 2^+ yrast transition and the total inelastic cross section 127
6.27 Ratio of the partial cross section for 6^+ to 4^+ yrast transition and the total inelastic cross section 128

A.1 Partial cross section for the E_γ = 983.5–keV transition in ^{48}Ti 138
A.2 Partial cross section for the E_γ = 2421.0–keV transition in ^{48}Ti 138
A.3 Partial cross section for the E_γ = 3371.2–keV transition in ^{48}Ti 138
A.4 Partial cross section for the E_γ = 3699.1–keV transition in ^{48}Ti 138
A.5 Partial cross section for the E_γ = 3738.1–keV transition in ^{48}Ti 139
A.6 Partial cross section for the E_γ = 159.4–keV transition in ^{47}Ti 139
A.7 Partial cross section for the E_γ = 1251.5–keV transition in ^{47}Ti 139
A.8 Partial cross section for the E_γ = 1549.9–keV transition in ^{47}Ti 139

A.9 Partial cross section for the $E_\gamma = 1793.9$–keV transition in ^{47}Ti 140
A.10 Partial cross section for the $E_\gamma = 1825.1$–keV transition in ^{47}Ti 140
A.11 Partial cross section for the $E_\gamma = 2259.3$–keV transition in ^{47}Ti 140
A.12 Partial cross section for the $E_\gamma = 2297.0$–keV transition in ^{47}Ti 140
A.13 Partial cross section for the $E_\gamma = 130.9$–keV transition in ^{48}Sc 141
A.14 Partial cross section for the $E_\gamma = 174.3$–keV transition in ^{45}Ca 141

Chapter 1

Introduction

Cross sections of many reactions, including preequilibrium reactions, have important practical applications, from the design of fission and fusion reactors to space and astrophysical research. It is often necessary to measure, or to estimate if measurement is not possible, nuclear cross sections both at low and high energies to moderate accuracy. The spin distribution transferred in preequilibrium neutron-induced reactions may play an important role in the predictions of reaction cross sections. The spin distributions can be deduced from a comparison of the relative population of low-lying states with different spins (measured using the GEANIE array), with the predictions from state-of-the-art Hauser-Feshbach codes incorporating preequilibrium models. Preequilibrium reactions are important when incident neutron energies are above $\approx$ 10 MeV, as evidenced by e.g., fast neutron emission. The transferred spin distribution is predicted by the theoretical calculations. However, there are no experimental data to compare with the theoretical calculations of the spin distribution in the residual nucleus in the region of the preequilibrium reactions. The powerful γ-ray array coupled with the intense neutron beam at WNR/LANSCE brings a new tool for the investigation of the preequilibrium process. The partial γ-ray cross sections for low-lying states with different J^π were measured as a function of neutron energy. These cross sections were interpreted with the aid of reaction modeling to determine the transferred spin distri-

bution. Increased understanding of the preequilibrium mechanism should improve reaction model predictions.

Preequilibrium reactions take place on a time scale that is between the direct and compound processes. Since preequilibrium emission occurs before the composite nucleus reaches its equilibrated state, on average the preequilibrium particles are emitted with more energy than the particles following the formation of a compound nucleus. Although the preequilibrium mechanism has been studied in the past, it is not completely understood. Measuring the prompt reaction γ rays as a function of incident neutron energy provides improved understanding of the spins populated by the preequilibrium reaction; this information is obtained by studying angular momentum information for the γ-ray cascades in the residual nucleus. Several models have been developed that describe the preequilibrium process: the cascade model [Ber63], the exciton model [Gri66], the FKK model [Fes80], the HMS [Bla96] model and the TUL [Tam82] model. The quantum-mechanical theory of Feshbach, Kerman, and Koonin (FKK) describes inelastic multistep processes in nucleon-induced reactions up to 200 MeV. This model allows a direct calculation of the spin distributions of residual nuclei remaining after preequilibrium emission. The magnitude of preequilibrium emission at various incident neutron energies affects the angular momentum distribution of the populated states in the entry region of the residual nucleus. This distribution is different from that arising from equilibrium neutron emission alone. To study the spin distribution of the residual nucleus in preequilibrium reactions, one needs to tag on states with specific angular momentum. An example would be to compare the population of 6^+ states to 2^+ states in the ground state band as a function of incident neutron energy in a region where preequilibrium is expected to dominate.

Neutron-induced reaction cross sections on natural titanium are important for radiochemical diagnostics used to monitor charged-particle flux. ^{48}Ti is the most abundant stable isotope (73.72%) in natural titanium. Charged-particle destruction cross sections on ^{48}Ti, for example (p,n), are measured with high accuracy (see e.g., West *et al.* [Wes93] and Gadioli *et al.* [Gad81]), but the neutron activation cross sections are poorly measured. The

amount of ^{48}V produced via (p, n) reactions on ^{48}Ti is somewhat sensitive to the neutron destruction cross sections of ^{48}Ti since it is in a neutron-rich environment. Data are available for the (n, p), $(n, 2n)$, and (n, α) cross sections via the activation technique, but they are mostly concentrated at E_n = 14 MeV. Furthermore, the data from different measurements are often contradictory. This leads to very different evaluations of the cross sections. For example, for the (n,α) reaction at E_n = 14 MeV, the ENDF/B-VI evaluation gives 18.5 mb, while the JENDL-3.3 evaluation gives 33 mb.

Prompt γ rays were produced from neutron-induced reactions on an enriched ^{48}Ti target. Partial cross sections have been measured using the spallation neutron beam and the Compton suppressed germanium detector array (GEANIE) at the Los Alamos Neutron Science Center (LANSCE). The majority of the known γ-ray transitions in low-lying discrete levels of the residual nucleus have been observed in the (n, n') and $(n, 2n)$ channels, and their γ-ray yields have been determined. A few of the prominent γ rays from transitions in low-lying excited levels for charged particles emission channels were also measured. The individual partial cross sections have been combined to produce an experimental lower limit on the ^{48}Ti(n,n$'\gamma$)^{48}Ti, ^{48}Ti(n,2nγ)^{47}Ti, ^{48}Ti(n,pγ)^{48}Sc and ^{48}Ti(n,$\alpha\gamma$)^{45}Ca cross sections for E_n = 20 MeV. The statistical Hauser-Feshbach calculation codes predict the partial cross sections for the unobserved contributions from the reaction. Measured lower limits were combined with Hauser-Feshbach calculations to produce a model-dependent estimate of the reaction channel cross sections.

This work consists of 7 chapters and an appendix. A brief theoretical background for the reaction mechanisms and an introduction to nuclear level densities and γ-ray strength functions are given in the following chapter. The experimental details of the measurement of prompt γ rays from neutron-induced reactions and a description of the experimental devices are presented in Chapter 3. In the Chapter 4 the analysis of the experimental data is described. The next chapter includes a description of the Hauser-Feshbach Statistical Model and its application to reaction model calculations. Chapter 6 contains experimental results on partial γ-ray cross sections of the ^{48}Ti + n reaction. Partial γ-ray cross sections and

channel cross sections are presented and compared with Hauser-Feshbach statistical model calculations. Also the spin distribution of states populated by the preequilibrium reactions and the comparison of experimental and theoretical predictions are discussed. Chapter 7 summarizes the results of this work, and provides suggestions for future research. An appendix presents the individual partial cross sections from prominent transitions included in the reaction channel cross sections.

Chapter 2

Theoretical Background

2.1 Introduction

In the interaction of a neutron with a nucleus, different types of processes may occur. These can be classified as three main types of reaction mechanisms: direct, compound nucleus, and preequilibrium (precompound) reactions [Hod97]. A direct reaction takes place on a short time scale which is of the order of the time taken by the projectile to traverse the target nucleus, typically around 10^{-22} s. On the other hand, a compound nucleus reaction happens in the relatively long time span $\approx 10^{-17}$ s, which is several orders of magnitude longer than the time scale of a direct reaction. The preequilibrium reaction is intermediate between direct and compound nuclear reactions. In this chapter, these three types of reactions are discussed and the relevant theoretical models presented.

2.2 Direct reactions

A direct reaction is a fast process. In a direct reaction the projectile interacts with a nucleon, a group of nucleons or the whole nucleus. Emission of one or more particles takes place immediately following the interaction. Direct reactions may excite many different types of nuclear states, and each provides a distinctive opportunity to learn more about

particular aspects of nuclear structure. The simplest direct interaction between an incident particle and a target nucleus is elastic scattering, with the particle's direction of motion and state of polarization changed without loss of energy. Direct or shape-elastic scattering occurs only when the incident particle interacts with the nucleus as a whole. When the energy of the reaction products, (but not their constituents), change as a result of interaction, this is called inelastic scattering. Inelastic scattering occurs when a projectile interacts with a nucleus and transfers some of its energy, raising the target nucleus to an excited state. This generally changes the direction of motion and state of polarization of the projectile. Other direct reactions are the stripping or pick-up reaction in which one or more nucleons are stripped or picked up from the projectile. These are also referred to as transfer reactions. The direct reaction mechanism can be described with the optical potential.

2.2.1 The phenomenological optical model

The direct reaction mechanism is described by the optical model which simulates the interaction between the projectile and the nucleons in the target nucleus by a nucleon-nucleus potential. Phenomenological optical model potentials are normally used to compare with and to fit experimental data. Practical calculations employ one-body phenomenological potentials which consist of a real term, $V(r)$, which describes the reflection of the particle flux, and an imaginary term, $W(r)$, which accounts for the removal of the particle flux from the incoming channel by the target nucleus. In $V(r)$ and $W(r)$, r is the distance between the incoming particle and the target. The general form of the phenomenological potential is given by:

$$\begin{aligned} U(r) &= V(r) + iW(r) \qquad (2.1) \\ &= V_c(r) \qquad \text{a Coulomb term} \\ &\quad -V(E_{inc})f_V(r) \qquad \text{a real volume term} \\ &\quad +V(E_{inc})g_V(r) \qquad \text{a real surface term} \\ &\quad -iW_s(E_{inc})g_w(r) \qquad \text{an imaginary surface term} \end{aligned}$$

$+iW_V(E_{inc})f_W(r)$ an imaginary volume term

$+d_{so}\hat{l}\cdot\hat{s}V_{so}h_{V_{so}}(r)$ a real spin-orbit term

$+id_{so}\hat{l}\cdot\hat{s}W_{so}h_{W_{so}}(r)$ and an imaginary spin-orbit term

where E_{inc} is the energy of the projectile in the laboratory system [Car00]. The Coulomb term is taken to be the interaction of a point charge with a uniformly charged sphere of radius R_c,

$$V_C(r) = \begin{cases} \left(\frac{3}{2} - \frac{r^2}{2R_c^2}\right) Z_p Z_t e^2/R_c, & r \leq R_c \\ Z_p Z_t e^2/r, & r > R_c \end{cases} \tag{2.2}$$

where Z_p and Z_t are the projectile and target charge. The Woods-Saxon potential is used for the real and imaginary volume terms $f_V(r)$ and $f_W(r)$. That is,

$$f_j(r) = \frac{1}{1 + exp[(r - R_j)/a_j]} \qquad j = V, W, \tag{2.3}$$

where $R_j = r_j A^{1/3}$ is the radius of the nucleus and a_j is the diffuseness parameter. The real volume potential reflects the average interaction of the projectile with the nucleons of the target nucleus. The Wood-Saxon form is quite similar in form to the nucleon density of a saturated nucleus. The strength of the real volume potential is roughly proportional to the mass of the projectile and decreases with incident energy. The imaginary volume potential takes account into the loss of projectile particles due to collisions with nucleons of the target.

The real and imaginary surface terms of the optical potential are taken to be proportional to the derivative of the volume potential. They peak at the surface of a nucleus and fall to zero within a distance of a few a_W, i.e.,

$$g_j(r) = -4a_j \frac{d}{dr} f_j(r) = 4\frac{exp[(r - R_j)/a_j]}{(1 + exp[(r - R_j)/a_j])^2} \qquad j = V, M. \tag{2.4}$$

The imaginary surface term of the optical potential takes into account the absorption due to the coupling to the quasi-bound compound nucleus states. The spin-orbit potentials are

assumed to be of a Thomas form:

$$h_j(r) = -\frac{1}{r}\frac{d}{dr}f_j(r) = \frac{1}{ra_j}\frac{exp[(r-R_j)/a_j]}{(1+exp[(r-R_j)a_j])^2} \qquad j = V_{so}, W_{so}. \tag{2.5}$$

The phenomenological optical model potential can be parametrized in terms of potential strengths and geometrical parameters. These parameters have been adjusted for many systems and values of the relative energy. For nucleons, typical values of the potential strengths are

$$\begin{aligned} V &\approx (45-55)\ \text{MeV} - (0.2-0.3)\ E(\text{MeV}), \\ W_s &\approx (2-7)\ \text{MeV} + (0.3-0.5)\ E(\text{MeV}), \qquad E < 8-10\ \text{MeV}, \\ V_{so} &\approx (4-10)\ \text{MeV}. \end{aligned} \tag{2.6}$$

Above 8 - 10 MeV, W_s is usually constant. The geometrical parameters, R_j and a_j, are assumed to be energy independent. Since inelastic scattering and nuclear reactions preferentially occur at the surface of a nucleus at low incident energies, the absorptive potential is typically constructed to have a surface component only when $E_{inc} \leq$10 MeV.

For elastic scattering, when the optical potential is inserted in the Schrödinger equation, and the wavefunction expanded into partial waves, the phase shifts for each partial wave can be obtained and hence the differential cross section. Inelastic scattering requires a more complicated model of the excited nuclear state constituting a set of coupled equations for the wavefunctions in the elastic and all inelastic channels in the reaction being considered. In principle, these equations can be solved for all of the wavefunctions. Since in practice the number of equations that can be solved in a practicable length of time is limited, it is necessary to seek a suitable approximate method of solution. Such approximation methods are coupled-channel equations and the distorted wave Born approximation. The coupled channels formalism is an extension of the optical model which allows the calculation of inelastic scattering to a few selected low-lying excited states. The calculation time increases rapidly with the number of states included, and thus it is necessary to restrict

the calculation to a few states. In the limit, when no inelastic channels are included, the formalism reduces to that of the simple optical model. The coupled-channels formalism has been extended to treat nucleon transfer reactions with inclusion of inelastic scattering in both the initial and final nuclei. The transfer itself is treated by the distorted wave Born approximation and so the whole calculation is called the coupled-channels Born approximation. This calculation has been successfully used to analyze a wide range of experimental data. As well as being fundamental for the calculation of direct reaction observables, optical model calculations are used to produce the transmission coefficients essential for the analysis of compound nucleus cross sections within the Hauser-Feshbach statistical theory.

2.3 Compound nucleus reactions

Many nuclear reactions take place by the capture of a projectile to form a compound nucleus in an excited energy state which subsequently decays by particle and gamma emission. Between formation and decay the excitation energy is shared statistically among its constituent nucleons so that all memory of its mode of formation is lost. The processes of formation and decay are thus independent of each other. This is the Bohr independence hypothesis [Boh36]. The independence of the processes of formation and decay of the compound nucleus can be tested experimentally by forming the same compound nucleus at the same excitation energy by different reactions and testing whether it decays in the same way in each case. It is useful to divide compound nuclear reactions according to whether or not the states in the compound nucleus and in the final nucleus are resolved. This depends both on the energy and target nucleus and on the energy resolution ΔE of the detecting apparatus. At low energies the reaction may go through a single state in the compound nucleus to a single state in the final nucleus. The cross sections of such reactions as a function of energy show a pronounced resonance structure that can be analyzed by the Breit-Wigner theory. For a reaction from channel a to channel b proceeding through well-separated compound nuclear resonances of spin J, the cross section can be expressed as a sum over individual

Breit-Wigner resonances:

$$\sigma_{ab}^{J}(E) = \pi \lambda\!\!\!^{-2} \sum_{\lambda} \frac{\Gamma_{\lambda a}\Gamma_{\lambda b}}{(E - E_{\lambda})^2 + \frac{1}{4}\Gamma_{\lambda}^2}, \tag{2.7}$$

where E is the incident energy, $\lambda\!\!\!^{-}$ is the reduced wavelength in the incident channel (inverse of the wave number k), $\Gamma_{\lambda a}$ and $\Gamma_{\lambda b}$ are the partial widths of resonance λ in the incident and exit channels, E_{λ} is the energy of the resonance and Γ_{λ} is its total width. The total width is the sum of the partial widths in all channels,

$$\Gamma_{\lambda} = \sum_{c} \Gamma_{\lambda c}. \tag{2.8}$$

When the level width Γ is larger than the level spacing D, the levels overlap strongly. In such situations, when the energy resolution $\Delta E < \Gamma$, the cross sections fluctuate strongly as a function of energy. However, because of overlapping resonances, fluctuation properties are rather complicated. Most theoretical considerations of compound nucleus cross sections use energy-averaged cross sections. If the energy spread $\Delta E \geq \Gamma$, many states in the compound nucleus are excited, but the fluctuations are no longer apparent. At low energies the reaction proceeds only to discrete states in each residual nucleus. As the energy increases it becomes possible to reach the unresolved continuum of states.

2.3.1 Hauser-Feshbach theory

Hauser-Feshbach theory describes reaction cross sections that involve a large number of compound nuclear states. The Bohr independence hypothesis allows the cross section to be written as the product of two factors, the cross section σ_a for formation of the compound nucleus and the probability P_b that it will decay into the channel b:

$$\sigma_{ab} = \sigma_a P_b. \tag{2.9}$$

The compound nucleus formation cross section for a particular orbital angular momentum is given by

$$\sigma_a = \pi \lambda\!\!\!^{-2}_{a}(2l + 1)T_a, \tag{2.10}$$

where $T_a = 1 - |S_{aa}|^2$ is the transmission coefficient in the a channel. The reciprocity theorem relates a cross section to its inverse:

$$\lambda\!\!\!^{-2}_b \sigma_{ab} = \lambda\!\!\!^{-2}_a \sigma_{\hat{b}\hat{a}}, \tag{2.11}$$

where $\hat{a}$ and $\hat{b}$ refer to time-reversed states. Combining these equations implies that

$$T_a P_b = T_{\hat{b}} P_{\hat{a}}. \tag{2.12}$$

Since this is true for all channels a and b,

$$\frac{P_{\hat{a}}}{T_a} = \frac{P_b}{T_{\hat{b}}} = \xi, \tag{2.13}$$

where ξ is a constant. Since the Ps are probabilities

$$\sum_a P_{\hat{a}} = \xi \sum_a T_a = 1. \tag{2.14}$$

Therefore

$$P_b = \xi T_{\hat{b}} = \frac{T_{\hat{b}}}{\sum_a T_a}. \tag{2.15}$$

Thus finally

$$\sigma_{ab} = \pi \lambda\!\!\!^{-2}_a (2l+1) \frac{T_a T_b}{\sum_c T_c}. \tag{2.16}$$

This is the simplest form of the Hauser-Feshbach formula. The T_a can be calculated from the appropriate optical model potentials. It can easily be applied to reactions to continuum states. This Hauser-Feshbach formula provides the cross section of a compound nuclear reaction from a single incident channel a to a single outgoing channel b, for a particular angular momentum l in the absence of spin. If the interacting particles have spin, the expression for the cross section must include the appropriate spin weighting factors. Suppose that the spins and angular momentum for the reaction T(a,b)R are defined as follows

$$\underbrace{\overset{i}{a} + \overset{I}{T}}_{s=i+I} \overset{l}{\rightarrow} (\overset{J}{CN})^* \overset{l'}{\rightarrow} \underbrace{\overset{i'}{b} + \overset{I'}{R}}_{s'=i'+I'}$$

The spin i of the incident particle and spin I of the target combine to form the channel spin s, which in turn combines with the orbital angular momentum l to form the total compound

nucleus angular momentum J, and similarly for the outgoing channel. The probability that the spins i and I combine to give a particular s is

$$P(s) = \frac{2s+1}{(2i+1)(2I+1)} \tag{2.17}$$

and similarly the probability of s combining with l to give J is

$$P(J) = \frac{2J+1}{(2s+1)(2l+1)} \tag{2.18}$$

Weighting the partial waves by $(2l+1)$ the cross section becomes

$$\sigma_{ab}^{HF}(E) = \pi \lambda\!\!\!^{-2}_a \sum_{J\Pi} \frac{2J+1}{(2i+1)(2I+1)} \frac{T_a T_b}{\sum_c T_c}. \tag{2.19}$$

where Π is the parity of the compound state and parity is conserved. The transmission coefficients depend on the angular momenta l, s, and J.

2.3.2 The width fluctuation correction

There are basically three ways of modifying the Hauser-Feshbach formula to take account of the correlations between the incident and outgoing waves in the elastic channel. These correlations may be taken into account formally by defining the corrected cross section to be

$$\sigma_{ab} = \pi \lambda\!\!\!^{-2}_a \left(\frac{T_a T_b}{\sum_c T_c} \right) W_{ab}, \tag{2.20}$$

where W_{ab} is the width fluctuation correction. This factor depends on the transmission coefficients T_i.

Moldauer width fluctuation correction

It is possible to obtain an explicit form for transmission coefficients dependence by assuming that all of the T_i are small [Mol61]. Since Hauser-Feshbach is a theory for the energy-averaged cross section, Eq. (2.7) needs to be averaged over an energy interval Δ large enough to contain many resonances; that is, $D/\Delta \leq 1$, where D is the average spacing

of resonances of spin J.

$$\int_0^\infty dE \frac{\Gamma_{\lambda a}\Gamma_{\lambda b}}{(E-E_\lambda)^2+\frac{1}{4}\Gamma_\lambda^2} = 2\pi\frac{\Gamma_{\lambda a}\Gamma_{\lambda b}}{\Gamma_\lambda}. \tag{2.21}$$

Using the expression the energy average of Eq. (2.7) then yields

$$\left\langle \sigma_{ab}^J(E)\right\rangle = \pi\lambda\!\!\!^{-2}\frac{2\pi}{D}\left\langle \frac{\Gamma_{\lambda a}\Gamma_{\lambda b}}{\Gamma_\lambda}\right\rangle. \tag{2.22}$$

Note that this expression does not contain the energy averages of the individual widths, but rather the average of the combination $\Gamma_a\Gamma_b/\Gamma$. This distinction is important because in general there are correlations between widths. To put this into a form comparable with the expressions for the Hauser-Feshbach formula, use the expressions for the transmission coefficient

$$T_a = 1 - |<S>|^2 \tag{2.23}$$

and for the average value of the S matrix element

$$<S>= e^{2i\delta}\left(1-\frac{\pi<\Gamma_a>}{D}\right). \tag{2.24}$$

Therefore

$$T_a = 1-\left(1-\frac{\pi<\Gamma_a>}{D}\right)^2 \simeq \frac{2\pi<\Gamma_a>}{D} \qquad \text{if} \quad <\Gamma_a>\leq D. \tag{2.25}$$

Moldauer has shown that several nuclear models give a relation of the form

$$T_a = 1 - exp\left(-\frac{2\pi<\Gamma_a>}{D}\right) \quad \text{for} \quad <\Gamma>\leq D. \tag{2.26}$$

Then the energy-averaged cross section can be expressed as

$$\left\langle \sigma_{ab}^J(E)\right\rangle = \pi\lambda\!\!\!^{-2}\frac{2\pi}{D}\frac{\langle\Gamma_a\rangle\langle\Gamma_b\rangle}{\langle\Gamma\rangle}W_{ab}, \tag{2.27}$$

where W_{ab} is a width fluctuation factor

$$W_{ab} = \left\langle\frac{\Gamma_a\Gamma_b}{\Gamma}\right\rangle\left(\frac{\langle\Gamma_a\rangle\langle\Gamma_b\rangle}{\langle\Gamma\rangle}\right)^{-1}. \tag{2.28}$$

In order to calculate W_{ab}, it is necessary to know the distribution of level widths in the compound nucleus. This distribution can be calculated from the statistical model. A χ^2

law with ν degrees of freedom is assumed for the distribution for the partial widths Γ, which are usually associated with transmission coefficients by

$$T = \frac{2\pi\Gamma}{D}, \tag{2.29}$$

where D is the mean level spacing. With this assumption, the width correction factor is

$$W_{ab} = \left(1 + \delta_{ab}\frac{2}{\nu_a}\right)\int_0^\infty dx \prod_c \left(1 + \frac{2T_c}{\nu_c \sum_i T_i}x\right)^{-\delta_{ac}-\delta_{bc}-\nu_c/2}, \tag{2.30}$$

where the number of degrees of freedom ν_i (proposed by Moldauer [Mol80]) is

$$\nu_i = 1.78 + (T_i^{1.212} - 0.78)exp\left(-0.228\sum_c T_c\right). \tag{2.31}$$

The HRTW approach

The next approach is the Hoffmann-Richert-Tepel-Weidenmüller (HRTW) method. It is based on the assumption that the main effect of the correlation between incident and outgoing waves is in the elastic channel. It is convenient to express the compound nuclear cross section as

$$\sigma_{ab} = \pi\lambda\!\!\!^{-2}_a \frac{V_a V_b}{\sum_c V_c}[1 + \delta_{ab}(W_a - 1)], \tag{2.32}$$

where the V_i's are effective transmission coefficients that take into account the correlations. The V_i values can be determined from the flux conservation condition

$$\sum_b \sigma_{ab} = \pi\lambda\!\!\!^{-2} T_a, \tag{2.33}$$

which yields

$$T_a = V_A + (W_a - 1)\frac{V_a^2}{\sum_c V_c}, \tag{2.34}$$

or

$$V_a = \frac{T_a}{1 + \frac{(W_a-1)V_a}{\sum_c V_c}}. \tag{2.35}$$

The only required information is thus the expression for W_a, which can be derived from Random Matrix theory. The width correction factor gives

$$W_a = 1 + \frac{2}{1 + T_a^F} + 87\left(\frac{T_a - \bar{T}}{\sum_c T_c}\right)^2\left(\frac{T_a}{\sum_c T_c}\right)^5, \tag{2.36}$$

where

$$\bar{T} = \frac{\sum_c T_c^2}{\sum T_c} \tag{2.37}$$

and the exponent

$$F = 4\frac{\bar{T}}{\sum_c T_c}\left(1 + \frac{T_a}{\sum_c T_c}\right) / \left(1 + \frac{3\bar{T}}{\sum_c T_c}\right). \tag{2.38}$$

The Gaussian orthogonal ensemble (GOE) approach

The GOE method does not explicitly define the width fluctuation correction factor W_{ab}, but rather σ_{ab} as function of the S-matrix elements,

$$\sigma_{ab} = \pi \lambda\!\!\!^{-}{}_a^2 [\overline{S_{ab} S_{ab}^*} - \overline{S_{ab}}\,\overline{S_{ab}^*}]. \tag{2.39}$$

After complicated algebraic transformations one obtains a complicated triple integral [Hil03]. The method to calculate this triple integral depends on the number of channels that must be considered in a nuclear reaction. More precisely, two different methods have been developed, depending on the value of the sum of all the transmission coefficients, the small sum region ($\sum_c T_c < 20$) and large sum region ($\sum_c T_c \geq 20$).

2.3.3 Nuclear level densities

Nuclear level densities play an important role in estimating nuclear reaction cross sections in general. The nuclear level density is the number of levels per unit energy. The nucleus can be divided into two regions. Up to a certain excitation energy (typically between 1 and 2 MeV) the number of levels is limited, and they are relatively well separated. In this energy region the levels are relatively simple in structure, and often can be understood on the basis of nuclear models. With increasing excitation energy, the number of levels increases, the spacing between them reduces, and the nature of the excitations becomes very complicated. Therefore, at high excitation energies the only way to describe them is using a statistical procedure. A level density function ρ is introduced

$$\rho(E) = \frac{dN(E)}{dE}, \tag{2.40}$$

where $N(E)$ is the cumulative number of levels up to the excitation energy E. From observation of the distribution of low-energy levels, an empirical formula can be obtained. This is the well-known Bethe formula for nuclear level densities: the Constant Temperature Formula (CTF) based on the Fermi gas model of the nucleus

$$\rho(E,J) = \frac{f(J)}{T} exp\left(\frac{E-E_0}{T}\right), \tag{2.41}$$

where E_0 and T (the nuclear temperature) can be adjusted to fit Eq. (2.41) to experimental data; $f(J)$ is the spin distribution factor

$$f\,(E,J) = \frac{2J+1}{2\sigma_c^2} exp\left(\frac{-(J+1/2)^2}{2\sigma_c^2}\right), \tag{2.42}$$

where σ_c is the spin cut-off parameter. In the simplest approach, the nucleus can be considered as a system of fermions which can occupy levels equidistant in energy. The density of excited levels is

$$\rho(E) = \frac{exp(2\sqrt{aE})}{4\sqrt{3}E} \tag{2.43}$$

where the parameter a is known as the level density parameter. A more realistic extension of this model considers the fact that fermions have the tendency to form pairs, and that it takes an extra amount of energy to separate them. By introducing a shift E_1 in the excitation energy this process can be taken into account. In general E_1 is considered as an adjustable parameter, which leads to the Back-Shifted Fermi Gas model(BSFG)

$$\rho(E,J) = f(J)\frac{e^{2\sqrt{a(E-E_1)}}}{\sigma_c 12\sqrt{2}a^{1/4}(E-E_1)^{5/4}}. \tag{2.44}$$

In this case the spin cut-off factor has the form [Gil65]

$$\sigma_c^2 = 0.0888A^{2/3}\sqrt{a(E-E_1)}. \tag{2.45}$$

The parameters a and E_1 are different from nucleus to nucleus, and can be adjusted in order to agree with the values of the level density at lower energies, and at the nucleon separation energy. This model can describe experiments in a narrow energy interval around the nucleon binding energy, where most experimental data are obtained from resonance

measurements. However, the BSFG model does not permit extrapolation to higher-energy regions, and shell effects are not properly taken into account. Extensions of the BSFG model exist. The model proposed by Gilbert and Cameron [Gil65] is a combination of the CTF and BSFG models: up to a cut-off energy E_x (around 2-3 MeV) the CTF formula is used; above this energy, the BSFG model is applied by using the pairing force V_0 instead of the back-shift E_1. All of these models have been developed under the assumption of no parity dependence of the level density.

2.3.4 γ-ray strength functions

In general for a γ transition of type and multipolarity XL from an initial state i to a final state f, the average partial radiation width is

$$\langle \Gamma_{\gamma if}^{XL} \rangle = \frac{f_{XL}(E_\gamma) E_\gamma^{2L+1}}{\rho(E_i, J_i^{\pi_i})} \tag{2.46}$$

where $\rho(E_i, J_i^{\pi_i})$ is the average level density at energy E_i of levels with the same spin and parity. Eq. (2.46) defines $f_{XL}(E_\gamma)$ as the photon strength function for transitions of type and multipolarity XL.

E1 photon strength functions

The simplest model for the E1 photon strength function is the single-particle model, which is energy independent:

$$f_{E1}^{SP} = \frac{3}{4}\left(\frac{1}{\hbar c}\right)^3 \frac{\bar{e}^2 R^2}{D_s} = C \cdot \frac{A^{2/3}}{D_s}, \tag{2.47}$$

where $C = 6.8 \times 10^{-8}$ MeV^{-2}, $\bar{e}$ is the effective charge of a single particle in a system of particles, R is the nuclear radius and D_s is the spacing of the single particle states with l=0. The value of D_s is 0.5 MeV [Bla79]; however, it is usually treated as a free parameter in order to fit the experimental data. It has been shown that the single-particle model overestimates the experimental data.

A more realistic approach makes use of the giant dipole resonance (GDR). Giant dipole resonances are directly observed in photonuclear reactions. The principle of detailed

balance for the (n,γ) and (γ,n) reactions, together with the assumption of the spin independence of the photon strength function, leads to the Lorentzian GDR photon strength function

$$f_{E1}(E_\gamma) = \frac{1}{3(\pi\hbar c)^2}\frac{\sigma_0 E_\gamma \Gamma_G^2}{(E_\gamma^2 - E_G^2)^2 + E_\gamma^2\Gamma_G^2}, \tag{2.48}$$

where σ_0, E_G, and Γ_G are the usual giant resonance parameters derived from photoabsorption experiments and E_γ is the γ-ray energy. The GDR can be explained as collective dipole vibrations of proton and neutron fluids inside the nucleus. The supposed independence of this collective motion from the intrinsic nuclear excitations leads to the important consequence (Brink's hypothesis) [Bri55] that giant resonances built on the ground state are similar in shape and size to those built on any excited state. A consequence of Brink's hypothesis is that the photon strength function depends only on the energy of the transition: it is not dependent on the excitation energy. At γ-ray energies corresponding to the neutron binding energy the Lorentzian GDR is often approximated by the Axel expression [Axe62], which has a E^5 dependence. Eq. (2.48) is valid for spherical nuclei. For deformed nuclei, the experimental data can be represented using a photon strength function given by the sum of two Lorentzians. Accurate measurements of the primary $E1$ radiation from neutron resonances indicate that the GDR model describes the experimental data much better than the single-particle model. Nevertheless, the simple Lorentzian shape of the absorption cross section seems to be inadequate at energies close to the neutron binding energy. Some extensions of the GDR model exist. The Lorentzian with an energy- and temperature-dependent damping width includes an energy dependent spreading width [Dov72] which is also dependent on the nuclear temperature of the state on which the giant resonance is built [Kad83]. The suggested damping width has the form

$$\Gamma(E_\gamma, T) = \Gamma_G \frac{E_\gamma^2 + 4\pi^2 T^2}{E_G^2}, \tag{2.49}$$

while the nuclear temperature is evaluated from the relation

$$T = \sqrt{(S_n - E_\gamma - \Delta)/a}, \tag{2.50}$$

where Δ is the correction for energy pairing (equal to zero for odd-odd nuclei) and a the Fermi gas level density parameter. The resulting formula for the GDR [Kop89] is

$$f_{E1}(E_\gamma, T) = \frac{1}{3(\pi\hbar c)^2} \frac{\sigma_0 E_\gamma \Gamma_G \Gamma(E_\gamma, T)}{(E_\gamma^2 - E_G^2)^2 + E_\gamma^2 \Gamma(E_\gamma, T)^2}. \tag{2.51}$$

Another model, proposed by Kadmenskij, Markushev and Furman (KMF) [Kad83], derived in the framework of the theory of Fermi liquids, attempts to describe the behavior of the E1 photon strength function in the lower energy region. This leads to a non-zero limit of f_{E1} as the transition energy E_γ tends to zero; evidence of this has been observed [Kop89]. The KMF formula is

$$f_{E1}(E_\gamma, T) = \frac{1}{3(\pi\hbar c)^2} 0.7 \frac{\sigma_0 E_G \Gamma_G \Gamma(E_\gamma, T)}{(E_\gamma^2 - E_G^2)^2}. \tag{2.52}$$

This model is valid only in the low-energy tail of the GDR (corresponding to the energy region below the neutron binding energy), while it diverges for $E_\gamma \to E_G$.

M1 photon strength functions

The $M1$ strength function is less well known than the $E1$ strength function. In general, experimental information can be obtained from high-energy transitions, for which the $M1$ strength function is about 1/7 of the $E1$ strength. At lower energies the experimental information is very limited.

As in the case of the $E1$ photon strengths, the first model developed for the $M1$ photon strength function was the single-particle model, which gives a constant strength function

$$f_{M1}^{SP} = \frac{\text{const}}{D_s}. \tag{2.53}$$

The value of f_{M1}^{SP} may be evaluated by measuring the intensity of high-energy γ rays of $M1$ character [Coc94]. A typical average value for medium nuclei is 6×10^{-9} MeV^{-3}. A Lorentzian model [Boh75] for the $M1$ strength exists, the Bohr-Mottelson function, which can be interpreted as due to collective motion of spin-up nucleons against spin-down nucleons. This collective $M1$ giant resonance, called the spin-flip resonance, is usually de-

scribed by a Lorentzian centered near the neutron binding energy with resonance parameters $E_G = 41A^{-1/3}$ MeV, $\Gamma_G = 4$ MeV, and a value of σ_0 that is usually adjusted to fit experimental data at the neutron binding energy. Although these two models are very different, controversial experimental results exist that make it difficult to decide which model should be preferred.

Recently, new models have been developed to explain observed strong $M1$ transitions. One model concerns the scissor mode which apply to bands in deformed nuclei. An even more recent model involves the shear mechanism to explain bands in spherical nuclei for high spin states.

E2 photon strength functions

Very limited experimental data are available for $E2$ photon strength functions. In fact, γ rays after neutron capture are found to be mainly of dipole character [Pos81]. Estimates of the strength of high-energy transitions in heavy nuclei indicate that the $E2$ strength is only a few per cent of the $E1$ strength. Also in this case the single-particle model gives an estimate of the $E2$ strength

$$f_{E2} = \text{const}\frac{A^{4/3}}{D_s} \tag{2.54}$$

where const $= 4.9 \times 10^{-14}$ MeV^{-4}.

A giant resonance model has also been used to fit the data, with parameters.

$$E_G = 63 \times A^{-1/3} \text{ MeV}, \quad \Gamma_G = 6.11 - 0.012 \times A \text{ MeV}, \tag{2.55}$$
$$\sigma_0 = 1.5 \times 10^{-4} Z^2 E_G^2 A^{-1/3}/\Gamma_G \text{ mb}.$$

Transitions of $M2$ electromagnetic character, or of higher multipolarities, are very rare in the γ-ray decay of the compound nucleus, and are difficult to observe in neutron capture γ-ray spectra. Emission of radiation with higher multipolarities can sometimes be observed at low excitation energies, if the spin difference between low-energy levels is such that γ-decays with lower multipolarities are forbidden.

2.4 Preequilibrium reactions

After the first interaction of the projectile with the nucleus, when one or more particles may be emitted, the energy is carried by only one or two nucleons. They soon interact with other nucleons, spreading the energy throughout the nucleus. At incident energies above about 10 MeV it is possible for particle emission to take place after the direct reaction, but long before the attainment of statistical equilibrium. These processes are called preequilibrium or sometimes pre-compound reactions. Their time scale is intermediate between the fast direct reactions and the relatively slow compound nucleus reactions. Evidence for such reactions is provided by studies of the fluctuations in the excitation functions of several reactions to a well-defined residual nucleus state and these show coherence widths considerably larger than those characterizing the fluctuations of compound nuclear processes. More direct evidence for preequilibrium reactions is provided by the energy spectra of the emitted particles. These observations may be understood by assuming that the transition from the initial to the final reaction channel occurs through the formation of an intermediate composite nucleus whose excitation takes place in a number of stages. The energy of the projectile is shared among the nucleons of the target by a cascade of nucleon-nucleon interactions that excites particle-hole states of increasing complexity. The nucleus is excited by a series of nucleon-nucleon collisions between the projectile and the target nucleons. These are considered to take place in a series of stages, beginning with the projectile in the continuum. The first interaction creates a particle-hole pair called a exciton, giving a two-particle one-hole ($2p1h$) state. There are a large number of possible $2p1h$ states. Subsequent interactions create additional particle-hole pairs, giving $3p2h$ states, and again there are very many $3p2h$ states for each $2p1h$ state. This process continues until the excitation is spread through the nucleus [Gad92].

Most preequilibrium reactions take place at energies high enough for it to be no longer possible to resolve the individual final states. The cross sections are those of reactions to a continuum of final states, and the absence of fluctuations in these continuum spectra

shows that to a high degree of accuracy one may assume that there are no interference effects. Then preequilibrium cross sections can be evaluated by adding the contributions incoherently from each stage of the nucleon-nucleon interaction cascade. The total cross section for preequilibrium emission is then the sum of the cross sections for emission from each state of the cascade. Thus if σ_C is the cross section for the formation of the composite nucleus in its initial configuration, which may be assumed to be equal to the reaction cross section, and P_1 is the emission probability from this stage, then the first contribution to preequilibrium emission is $\sigma_C P_1$. These processes may be considered direct reactions together with other processes. Now the probability for transition from the first stage to the second is λ_{12}, the probability of emission from the second stage is P_2, the cross section for a second stage preequilibrium process is $\sigma_C \lambda_{12} P_2$, and so on. Thus the total direct and preequilibrium cross section is

$$\begin{aligned} \sigma_{Di+PE} &= \sigma_C P_1 + \sigma_C \lambda_{12} P_2 + \sigma_C \lambda_{12} \lambda_{23} P_3 + \dots \\ &= \sigma_C \sum_N P_N \prod_{k=1}^{N} \lambda_{k-1,k}, \end{aligned} \tag{2.56}$$

where $\lambda_{0,1} = 1$.

Several theoretical models are developed for preequilibrium reactions such as the exciton model and the quantum mechanical FKK [Fes80] theory. In the next sections, the exciton model and FKK theory are discussed.

2.4.1 The exciton model

In this model [Gri66] the hypothesis is made that the incoming projectile, by interacting with the target nucleus, gives rise to a simple initial configuration characterized by a small number of excited particles and holes called excitons. Successive two-body residual interactions give rise to an intranuclear cascade which, through a sequence of states characterized by an increasing exciton number, eventually leads to a fully equilibrated residual nucleus. Restriction to two-body residual interactions leads to the following selection rules

concerning the possible variation of the number n of excitons, of particles p, and holes h:

$$\Delta n = 0, \pm 2 \quad \Delta p = 0, \pm 1 \quad \Delta h = 0, \pm 1. \tag{2.57}$$

The states which are excited in this interaction cascade are very unstable. Two possible sequences of events considered in the exciton model are shown in Fig. 2.1. In the first sequence the incident particle, as well as the excited particles, are all bound, while in the second sequence the incident particle or one struck nucleon which attained a high energy are in the continuum. At each stage of this equilibrium process there is a competition between two decay modes of the composite nucleus: the decay by exciton-exciton interactions to more complex configurations and the decay by emission of particles into the continuum.

The exciton model assumes that (1) at each stage of the cascade all of the states with the same configuration and the same total energy are equiprobable, and (2) at each stage of the cascade all the processes which may occur are also equiprobable.

The first assumption gives the energy distribution of the excitons. The number $dN_p(p, h, E, \varepsilon)$ of the excitons with energy between ε and $\varepsilon + d\varepsilon$ in a configuration of p particles and h holes with total energy E is given by the ratio between the number of states in which one particle has energy between ε and $\varepsilon + d\varepsilon$ and the remaining $p-1$ particles and h holes have the energy $E-\varepsilon$ and the number of states of the p particle, h hole configuration with energy E. If $\rho_{p,h}(E)$ is the density of states of the configurations of p particles and h holes at the energy E, $\rho_{p-1,h}(E-\varepsilon)$ is the density of states of the configurations of $p-1$ particles, h holes with energy $E-\varepsilon$, then $dN_p(p, h, E, \varepsilon)$ is given by

$$dN_p(p, h, E, \varepsilon) = \frac{\rho_{p-1,h}(E-\varepsilon) g d\varepsilon}{\rho_{p,h}(E)}. \tag{2.58}$$

where $g = 1/d$ the density of single-particle states (for which one usually assumes the Fermi gas model $g = 3A/2\varepsilon_F$).

The second assumption gives the simplification of the evaluation of the cross sections of the various reactions. Define an escape width $\Gamma^{\uparrow}(\nu, \varepsilon_\nu | E, p, h) d\varepsilon_\nu$ for emission into the continuum of one unbound particle ν with energy ε_ν and a spreading width $\Gamma^{\downarrow}_{n,n'}$ for a

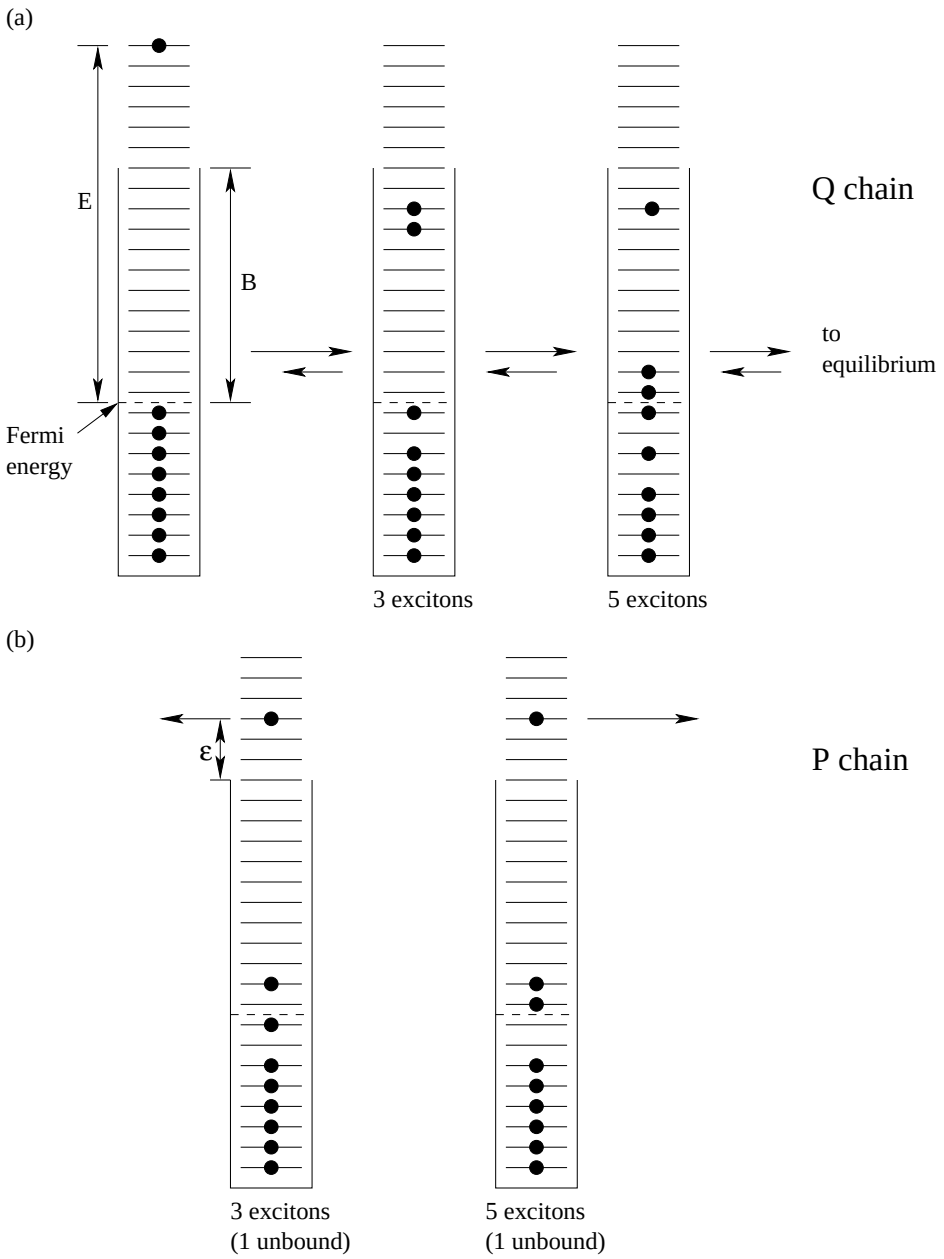

Figure 2.1: Schematic representation of the first few stages of a nucleon-induced reaction in the exciton model and the Feshbach, Kerman and Koonin (FKK) theory. The horizontal lines indicate equally spaced single-particle states in the potential well. The particles are shown as solid circles. E is the initial excitation energy. B is the average nucleon binding energy. Part (a) shows nucleon-nucleon interactions leading to the equilibrium process, in this case all particles are bound. In FKK theory this sequence of processes is called the Q chain. Part (b) shows interactions leading to configurations in which at least one particle is unbound and thus may be emitted into the continuum with energy ε leaving a residue with energy $U = E - B - \varepsilon$. In FKK theory this sequence is called the P chain.

nucleon-nucleon interaction which in most cases spreads the excitation energy among an increasing number of excitons. These widths are related to the probabilities per unit time (or decay rates) for the corresponding processes, $W^{\uparrow}$ and $W^{\downarrow}$, by the relation $\Gamma = W\hbar$.

When a particle is emitted, a residual nucleus with $p-1$ excited particles and h holes is created. If $\rho_{p,h}(E)$ and $\rho_{p-1,h}(U)$ are the composite and the residual nucleus state densities, the detailed balance principle gives for the escape width for emission of a particle ν with energy between ε_ν and $\varepsilon_\nu + d\varepsilon_\nu$:

$$\begin{aligned}\Gamma^{\uparrow}(\nu,\varepsilon_\nu|E,p,h)d\varepsilon_\nu &= \hbar W(\nu,\varepsilon_\nu|E,p,h)d\varepsilon_\nu \\ &= \frac{\hbar}{\rho_{p,h}(U)}\left(\frac{v_\nu\sigma_{\text{inv}}(\varepsilon_\nu)}{V}\right)\rho_{p-1,h}(U)\rho_c(\varepsilon_\nu)d\varepsilon_\nu, \end{aligned} \tag{2.59}$$

where v_ν is the emitted nucleon velocity, $\sigma_{\text{inv}}(\varepsilon_\nu)$ the inverse process cross section, and

$$\rho_c(\varepsilon_\nu) = \frac{1}{\pi^2\hbar^3}\frac{(2s_\nu+1)m_\nu\varepsilon_\nu V}{v_\nu} \tag{2.60}$$

is the density of the translational continuum states of the emitted particle as predicted by the Fermi gas model. V is the laboratory volume.

The estimate of the spreading width $\Gamma^{\downarrow}_{n,n'}$ is obtained by using time-dependent perturbation theory which gives

$$\Gamma^{\downarrow}_{n,n'}(E) = 2\pi\overline{|M|^2}\rho_f, \tag{2.61}$$

for a transition from the states of a configuration of n excitons to states of a configuration of n' excitons. ρ_f is the density of the states which may be excited in the nucleon-nucleon interaction and M is the transition matrix element. Considering only two-body interactions, by selection rules $n' = n$ or $n \pm 2$ at low energies,

$$\Gamma^{\downarrow}_{n,n+2} \geq \Gamma^{\downarrow}_{n,n} \geq \Gamma^{\downarrow}_{n,n-2}. \tag{2.62}$$

The dominant $n \to n+2$ transition spreading width is given by

$$\Gamma^{\downarrow}_{n,n+2}(E) = 2\pi\overline{|M|^2}\frac{g^3E^2}{2(n+1)} = 2\pi\overline{|M|^2}\frac{(3A/2\varepsilon_F)^3E^2}{2(n+1)}. \tag{2.63}$$

The average squared matrix for two-body interactions is given by

$$\overline{|M|^2} = KA^{-3}E^{-1}, \tag{2.64}$$

where the value of K varies between 100 and 700 MeV.

When the spreading and the escape widths are known, the preequilibrium cross section may be calculated using the expression Eq. (2.56). The total escape width for stage N

$$\Gamma_N^{\uparrow} = \sum_{\nu} \int_0^{\varepsilon_\nu^{max}} \Gamma_N^{\uparrow}(\nu, \varepsilon_\nu | E, p, h) d\varepsilon_\nu, \tag{2.65}$$

and, since

$$P_N(\varepsilon_\nu) d\varepsilon_\nu = \frac{\Gamma_N^{\uparrow}(\nu, \varepsilon_\nu | E, p, h) d\varepsilon_\nu}{(\Gamma_N^{\uparrow} + \Gamma_N^{\downarrow})} = \frac{\Gamma_N^{\uparrow}(\nu, \varepsilon_\nu | E, p, h) d\varepsilon_\nu}{\Gamma_N}, \tag{2.66}$$

where $\Gamma_N^{\downarrow} \approx \Gamma_{N+2}^{\downarrow}$ and the total width Γ_N equals $\Gamma_N^{\uparrow} + \Gamma_N^{\downarrow}$ and

$$\lambda_{k-1,k} = \frac{\Gamma_{k-1}^{\downarrow}}{\Gamma_{k-1}}, \tag{2.67}$$

it follows that

$$\sigma_{Di+PE}(\varepsilon_\nu) d\varepsilon_\nu = \sigma_C \sum_N \frac{\Gamma_N^{\uparrow}(\nu, \varepsilon_\nu | E, p, h) d\varepsilon_\nu}{\Gamma_N} \prod_{k-1}^{N} \frac{\Gamma_{k-1}^{\downarrow}}{\Gamma_{k-1}}, \tag{2.68}$$

with $\Gamma_0^{\downarrow}/\Gamma_0 \equiv 1$. Usually after a few stages the preequilibrium emission becomes negligible and further interactions lead to an equilibrated compound nucleus.

The exciton model provides in most cases a very reasonable reproduction of the experimental data, despite its extreme simplicity.

2.4.2 Feshbach, Kerman, and Koonin theory

Several quantum mechanical theories of preequilibrium emission have been proposed, and the one by Feshbach, Kerman and Koonin has been most extensively compared with experimental data. The theory distinguishes between two types of processes, the multistep compound and multistep direct reactions. In a multistep compound reaction all the particles remain bound during the equilibration cascade, while in multistep direct reactions at least

one particle is always in the continuum. Thus the two processes involve states of the Q and P chains shown in Fig. 2.1. As in the case of the exciton model, the reaction is considered to proceed through stages of increasing complexity. At each interaction stage it is useful to consider separately the states with at least one particle in the continuum and the states with all particles bound. These may be formally described by the projections P and Q acting on the total wavefunction Ψ, with $P + Q = 1$. The set of states $P\Psi$ contributes to the multistep direct process and the complementary set of states $Q\Psi$ to the multistep compound process [Fes80]. Two assumptions are made: the first, the chaining hypothesis, assumes that the residual interaction can induce transitions from the nth stage only to the $(n \pm 1)$th stages; the second is that the relative phases of certain matrix elements are assumed to be random [Gad92]. In multistep compound reactions the phases of the competing processes interfere so that multistep compound reactions have energy-averaged cross sections that are symmetric about 90°. Multistep direct reactions take place rapidly and have cross sections that are generally peaked in the forward direction. The multistep description of a nuclear reaction is sketched in Fig. 2.2. Preequilibrium reactions can take place directly from each stage of the P chain, or indirectly from the Q chain. The emissions from the Q chain take place through states in the P chain, and this can take place in three ways as shown in the figure. The more energetic particles come from the early stages of the chains and the less energetic from the later stages.

2.4.3 Multistep compound reactions

In the multistep compound theory, the cross section for emission from each stage is expressed as in the exciton model by product of three factors: (1) the cross section for the formation of the composite nucleus; (2) the probability of reaching the nth stage; and (3) the probability of preequilibrium emission from the nth stage. The total cross section for the preequilibrium emission is then given by the sum of these products over all stages before the formation of the fully equilibrated compound nucleus. The cross section for the

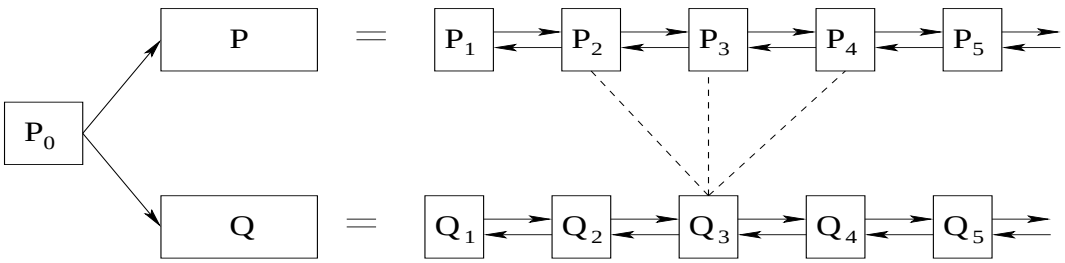

Figure 2.2: Multistep description of a nuclear reaction, according to Feshbach et al. [Fes80].

formation of the composite nucleus is

$$\sigma_a = \pi \lambda\!\!\!^{-2} \sum_J (2J+1) \frac{2\pi < \Gamma_{1J} >}{< D_{1J} >} \tag{2.69}$$

where $2\pi < \Gamma_{1J} > / < D_{1J} >$ is the strength function for the initial reaction stage. The probability of reaching the nth stage through a particular sequence of stages without preequilibrium emission is given by the product of the probabilities of passing through the intervening $n-1$ stages. Assuming the chaining and the never-come-back approximations, the total probability of reaching the nth stage is given by

$$\prod_{k=1}^{n-1} \frac{< \Gamma_{kJ}^{\uparrow} >}{\Gamma_{kJ}}, \tag{2.70}$$

where the total width $< \Gamma_{kJ} >$ is the sum of the total escape width $\Gamma_{kJ}^{\uparrow}$ and the damping width $< \Gamma_{kJ}^{\downarrow} >$, referring to emission and internal transitions respectively:

$$< \Gamma_{kJ} > = < \Gamma_{kJ}^{\uparrow} > + < \Gamma_{kJ}^{\downarrow} > . \tag{2.71}$$

The probability of emission of a particle into the continuum from the nth stage is given by the sum of the decay rates for all possible emission processes divided by the total decay rate. The sum of the decay rates for all possible emission processes is proportional

to the products of the emission widths $\Gamma_{nJ}^{\uparrow lsv}$ and the densities $\rho_s^{\nu}(U)$ of the final states at excitation energy U which may be reached from a compound state of spin J, and the total decay rate is proportional to the width Γ_{nJ}.

Thus the required probability is

$$\sum_{\nu} \frac{< \Gamma_{nJ}^{\uparrow lsv}(U)\rho_s^{\nu}(U) >}{< \Gamma_{nJ} >}, \tag{2.72}$$

where ν labels the three exit modes corresponding to $\Delta n = 0, \pm 2$. Putting these factors together and using the random phase approximation for all channel quantum numbers gives for the double-differential cross section for preequilibrium emission

$$\begin{aligned} \frac{d^2\sigma}{d\Omega d\varepsilon} &= \pi \lambda\!\!\!^{-2} \sum_J (2J+1) \left[\sum_{n=1}^{r} \sum_{ls\lambda} C_{lsJ}^{\lambda} P_{\lambda}(cos\theta) \right. \\ &\quad \left. \times \sum_{\nu=n-1}^{n+1} \frac{< \Gamma_{nJ}^{\uparrow lsv} \rho_s^{\nu}(U) >}{< \Gamma_{nJ} >} \prod_{k=1}^{n-1} \frac{< \Gamma_{kJ}^{\downarrow} >}{< \Gamma_{kJ} >} 2\pi \frac{< \Gamma_{1J} >}{D_{1J}} \right], \end{aligned} \tag{2.73}$$

where C_{lsJ}^{λ} is the angular momentum coupling coefficient and equals

$$C_{lsJ}^{\lambda} = (-)^s \left(\frac{2\lambda+1}{4\pi} \right)^{1/2} \begin{pmatrix} J & J & \lambda \\ 0 & 0 & 0 \end{pmatrix} \bar{Z}(lJlJ; s\lambda) \tag{2.74}$$

with $\lambda = 0, 2, 4, \cdots$, ensuring the symmetric emission characteristic of quasi-equilibrium processes. Integration over all angles gives the energy spectrum

$$\frac{d\sigma}{d\varepsilon} = \pi \lambda\!\!\!^{-2} \sum_J (2J+1) \sum_{n-1}^{r} \sum_{ls\nu} \frac{< \Gamma_{nJ}^{\uparrow lsv} \rho_s^{\nu}(U) >}{< \Gamma_{nJ} >} \prod_{k=1}^{n-1} \frac{< \Gamma_{kJ}^{\downarrow} >}{< \Gamma_{kJ} >} 2\pi \frac{< \Gamma_{1J} >}{D_{1J}}. \tag{2.75}$$

The cross section for preequilibrium emission falls quite rapidly from stage to stage. As the excitation spreads through the whole compound nucleus, the rate of increase in level density with the stage number falls so that the rate of backward transitions increases. When these rates become the same, full statistical equilibrium has been established. The total cross section for emission after the truncation of the preequilibrium chain is called the residual or r-stage cross section and is given by

$$\frac{d\sigma_r^{(f)}}{d\varepsilon} = \pi \lambda\!\!\!^{-2} \sum_J (2J+1) \frac{\pi < \Gamma_{1J} >}{< D_{1J} >} \left(\prod_{k=1}^{r-1} \frac{\Gamma_{kJ}^{\downarrow}}{\Gamma_k} \right) \frac{\Gamma_{rJ}^{(f)}}{\Gamma_{rJ}}. \tag{2.76}$$

Since the r-stage is the last stage in the chain,

$$\Gamma_{rJ} = \Gamma_{rJ}^{\uparrow} = \sum_c \Gamma_{rJ}^{(c)} \tag{2.77}$$

and the r-stage cross section becomes

$$\sigma_r = \pi \lambda\!\!\!^{-2} \sum_J (2J+1) \frac{T_i T_f}{\sum_c T_c}, \tag{2.78}$$

where

$$T_i = \frac{2\pi < \Gamma_1 >}{D_1} \left(\prod_{k=1}^{k=r-1} \frac{\Gamma_{kJ}}{\Gamma_{kJ}} \right) \tag{2.79}$$

and

$$T_f = \frac{2\pi \Gamma_{rJ}^{(f)}}{D_r}. \tag{2.80}$$

Eq. (2.75) is similar to the Hauser-Feshbach formula, but there are important differences. All of the factors in the expressions are calculated quantum-mechanically or, as in the case of the level density function, obtained from known systematics of nuclear properties.

Preequilibrium emission occurs as a result of nucleon-nucleon interactions during the early stages of a nuclear reaction. At each stage there are three possibilities: excitation of an additional particle-hole pair, de-excitation of a particle-hole pair, and emission into continuum state. In order to evaluate the cross section for the emission of particles by the multistep compound process it is necessary to evaluate the escape and damping widths. To calculate these widths it is necessary to consider in detail the interactions involved in the emission process, and the density of states available in the residual nucleus. The escape width is expressed as a product of the energy-dependent width $\Gamma_{nJ}^{ls\nu}$ and the final state level density ρ_s^{ν}, and this product may itself be factorized into a term $\mathrm{X}_{nJ}^{ls\nu}(U)$ containing the angular momentum dependence due to the nucleon-nucleon interaction and the spin distribution of single-particle states and a term $\mathrm{Y}_n^{\nu}(U)$ containing all the U dependence due to final state level density,

$$\Gamma_n = \sum_{\nu=n-1}^{n+1} \Gamma_{n\nu} = \sum_{\nu=n-1}^{n+1} < \Gamma_{nJ}^{ls\nu}(U) \rho_{\nu}^{s}(U) >= \mathrm{X}_{nJ}^{ls\nu}(U) \mathrm{Y}_n^{\nu}(U). \tag{2.81}$$

The damping width is also given by

$$< \Gamma_{nJ}^{\downarrow} >= \mathrm{X}_{nJ}^{\downarrow n+2} \mathrm{Y}_{n}^{\downarrow n+2}(E). \tag{2.82}$$

In order to calculate the X and Y functions we need to know the density of a p particle, h hole configuration at an excitation energy E. This is obtained from the equidistant spacing model. It takes into account the Pauli principle correction and the limitation of the particle energy to bound states and the hole energy to the depth of the potential. The X functions contain angular momentum coupling factors and the radial overlap integrals in the matrix element for the transition. It is only the angular momentum component of the initial and final state densities that enters the X functions, since the energy-dependent component is included in the Y functions. The Y function gives the accessible phase space and is obtained when the matrix element for a certain transition squared, averaged over initial states, and summed over final states. It is computed by considering the state densities of the initial and final particle-hole configurations, and is angular momentum independent.

2.4.4 Multistep direct reactions

At lower incident energies all of the particles in the intra-nucleus cascade remain bound, and the reaction may be described by the multistep compound theory discussed in the previous section. As the incident energy increases it becomes more likely that one particle remains in the continuum and so retains a strong memory of the original direction of the projectile. The timescale of the reaction is much shorter than in the multistep compound reaction. The theory of multistep direct reactions has been developed by Feshbach, Kerman, and Koonin [Fes80], by Tamura, Udagawa and Lenske [Tam82] and by Nishioka, Weidenmüller and Yoshida [Nis88], using somewhat different statistical assumptions. In this section, the FKK theory is discussed.

The interaction of a projectile with a target nucleus takes place by a series of nucleon-nucleon interactions, and at each of these interactions preequilibrium emission can take

place. The total double differential cross section for preequilibrium emission is thus the sum of the cross sections for emission from each stage

$$\frac{d^2\sigma}{dUd\Omega} = \left(\frac{d^2\sigma}{dUd\Omega}\right)_1 + \left(\frac{d^2\sigma}{dUd\Omega}\right)_M \tag{2.83}$$

where the subscript 1 indicates the first stage, and M the subsequent multistep stages. The cross section for the first stage is evaluated using the distorted wave theory, assuming the spectroscopic factors to be unity, and is given by

$$\left(\frac{d^2\sigma}{dUd\Omega}\right)_1 = \sum_l (2l+1)\omega(U,l) \left\langle \left(\frac{d^2\sigma_1}{dUd\Omega}\right)_{DW} \right\rangle_l . \tag{2.84}$$

where $< (d^2\sigma/dUd\Omega)_{DW} >$ is the first order distorted wave Born approximation differential cross section averaged over all energetically possible $1p1h$ states in the residual nucleus that corresponds to a particular angular momentum transfer, and $\omega(U,l)$ is the density of $1p1h$ levels in the residual nucleus.

The multistep cross section is the sum of the cross sections from all of the subsequent stages, and each of these is given by the folding integral of transition probabilities:

$$\begin{aligned}\left(\frac{d^2\sigma}{dUd\Omega}\right)_M &= \sum_n \sum_{m=n-1}^{n+1} \int \frac{d\mathbf{k_1}}{(2\pi)^3} \int \frac{d\mathbf{k_1}}{(2\pi)^3} \cdots \int \frac{d\mathbf{k_n}}{(2\pi)^3} \frac{d^2W_{mn}(\mathbf{k_f},\mathbf{k_n})}{dUd\Omega} \\ &\times \frac{d^2W_{n,n-1}(\mathbf{k_n},\mathbf{k_{n-1}})}{dU_n d\Omega_n} \cdots \frac{d^2W_{21}(\mathbf{k_2},\mathbf{k_1})}{dU_2 d\Omega_2} \left(\frac{d^2\sigma(\mathbf{k_1},\mathbf{k_i})}{dUd\Omega}\right)_1 ,\end{aligned} \tag{2.85}$$

where m labels the exit mode and n the stage. The transition probability for the $(n-1)$th to nth stage, when the particle momentum changes from $\mathbf{k_{n-1}}$ to $\mathbf{k_n}$ is

$$\frac{d^2W_{n,n-1}(\mathbf{k_n},\mathbf{k_{n-1}})}{dU_n d\Omega_n} = 2\pi^2 \rho(\mathbf{k_n})\rho_\mathbf{n}(\mathbf{U}) < |\nu_{\mathbf{n},\mathbf{n-1}}(\mathbf{k_n},\mathbf{k_{n-1}})|^\mathbf{2} >, \tag{2.86}$$

where $\rho(\mathbf{k}_n) = m\mathbf{k}_n/(2\pi)^3\hbar^2$ is the density of states of the particle in the continuum, $\rho(U)$ is the level density of the residual nucleus at excitation energy U, and $\nu_{n,n-1}(\mathbf{k_n},\mathbf{k_{n-1}})$ is the matrix element for the transition from a state $n-1$ to a state n when the particle in the continuum changes its momentum from $\mathbf{k_{n-1}}$ to $\mathbf{k_n}$. The matrix element can be evaluated by the distorted wave Born approximation expression

$$\nu_{a,b}(\mathbf{k_i},\mathbf{k_f}) = \int\int \chi_b^{(-)*} < \psi_f|V(r)|\psi_i > \chi_a^{(+)} dr_a dr_b \tag{2.87}$$

where $V(r)$ is the effective interaction for the transition, $\chi_a^{(+)}$ and $\chi_b^{(-)*}$ are the incoming and outgoing distorted waves, and ψ_i and ψ_f the wavefunctions of the initial and final nuclear states. In the FKK theory it is assumed that the interference terms cancel and the different partial waves contribute incoherently, so that the average value of the squared matrix element becomes

$$< |\nu(\mathbf{k_i}, \mathbf{k_f})|^2 >= \sum_l (2l+1) < |\nu_l(\mathbf{k_i}, \mathbf{k_f})|^2 > R(l) \tag{2.88}$$

where $R(l)$ is the spin distribution function of the residual nuclear levels. This is the same for all stages in the reaction.

To calculate the cross section for the first stage the inelastic cross section $(d\sigma/d\Omega)_{DW}$ is evaluated microscopically as a function of angle for each transferred l value for all possible pairs of initial and final bound states compatible with energy conservation. The single particle shell model is used to describe the nuclear states. To obtain the first stage cross section, the density of levels

$$\omega(U, l) = \rho_n(U) R_n(l) \tag{2.89}$$

can be obtained from the Ericson formula

$$\rho_n(U) = \frac{g(gU)^{n-1}}{p!h!(n-1)!} \tag{2.90}$$

and the spin distribution function

$$R_n(l) = \frac{2l+1}{\sqrt{\pi} 2^{3/2} \sigma^3} \exp\left(-\frac{(l+\frac{1}{2})^2}{2\sigma^2}\right), \tag{2.91}$$

where σ^2 is the spin cut-off parameter.

2.4.5 Spin effects of the preequilibrium reactions

The FKK theory distinguishes multistep compound and multistep direct preequilibrium reactions, and at incident energies below about 50 MeV both types of reactions contribute. The FKK theory was originally formulated with assumption of zero intrinsic projectile, ejectile, and target spin. But calculations of observables sensitive to spins

require a more accurate treatment. The work of Herman et al. [Her84] and Chadwick et al. [Cha89], [Bon91] removed this assumption in MSC reactions. Also the work of Chadwick et al. [Cha94b] showed the effects of nonzero intrinsic spins in MSD reactions. MSD theory represents an extension of distorted-wave-Born-approximation theory (DWBA) into the continuum. Chadwick et al. [Cha94b] removed the original FKK spin-zero approximation in MSD by treating the $1p1h$ states excited in the interaction as absorbing the transferred angular momentum, after which their angular momentum couples with the intrinsic "core" spin of the target. It accounted for nonzero intrinsic spins while being able to use existing MSD calculation formalism. For projectile and ejectile spins i and a target spin I, leaving a residual nucleus with spin J after inelastic scattering with an orbital angular momentum transfer l, the 1-step MSD cross section is given by

$$\frac{d^2\sigma(E,\Omega \leftarrow E_0,\Omega_0)}{d\Omega dE}_{1step} = \sum_J \frac{2J+1}{(2I+1)(2i+1)} \sum_{S_f=0}^{1} \frac{1}{2S_f+1}$$
$$\times \sum_{S=|I-S_f|}^{I+S_f} \sum_{l=|J-S|}^{J+S} \rho(1p,1h,E_0-E,l) \left\langle \left[\frac{d\sigma(E,\Omega \leftarrow E_0,\Omega_0)}{d\Omega}\right]_l^{DWBA} \right\rangle \tag{2.92}$$

where S_f is the spin flip. In the limit of zero intrinsic spins this expression reduces to the usual FKK 1-step MSD result.

$\rho(1p,1h,E_0-E,l)$ is the density of $1p1h$ states with energy E_0-E and angular momentum l. The density of states for a p particle, h hole system can be partitioned into the energy dependent density multiplied by a spin distribution,

$$\rho(p,h,E,l) = \omega(p,h,E)R_n(l), \tag{2.93}$$

where, using the finite-well-depth restricted Williams [Wil71] expression,

$$\omega(p,h,E) = \frac{g^n}{p!h!(n-1)!} \sum_{j=0}^{h} \begin{pmatrix} h \\ j \end{pmatrix} (-1)^j (E - A_{ph} - j\varepsilon_F)^{n-1} \Theta(E - A_{ph} - j\varepsilon_F), \tag{2.94}$$

with $n = p+h$, and the singe-particle spacing $g = A/13$. The Pauli-blocking factor is $A_{ph} = [p^2+h^2+p-3h]/4g$, and ε is the Fermi energy. The function Θ is unity if

its argument is greater than zero, and zero otherwise. The spin dependent function, a Gaussian angular momentum distribution assumed, given by Eq. (2.91) with recommended Gruppelaar-Facchini spin cut-off parameter, $\sigma_n^2 = 0.24nA^{2/3}$.

$\left\langle \left[\frac{d\sigma(E,\Omega\leftarrow E_0,\Omega_0)}{d\Omega}\right]_l^{DWBA} \right\rangle$ is the average of DWBA cross sections exciting $1p1h$ states of energy $E_0 - E$, consistent with angular momentum and parity conservation. The $1p1h$ states can be obtained from a spherical Nilsson model.

MSD multistep cross sections obtained from a convolution of normal DWBA matrix elements, which give a contribution from the Nth stage,

$$\frac{d^2\sigma^(N)(E,\Omega \leftarrow E_0,\Omega_0)}{d\Omega dE} = \frac{m}{4\pi^2\hbar^2}\int d\Omega_{N-1}\int dE_{N-1}E_{N-1}$$
$$\times\frac{d^2\sigma^(1)(E,\Omega \leftarrow E_{N-1},\Omega_{N-1})}{d\Omega dE}\frac{d^2\sigma^{(N-1)}(E_{N-1},\Omega_{N-1} \leftarrow E_0,\Omega_0)}{d\Omega_{N-1}dE_{N-1}}. \tag{2.95}$$

At above 10 MeV energies of the incident neutrons preequilibrium emission is dominated by 1-step scattering which, from phase space considerations, contains a large MSD component. Recently, a MSD formalism was presented [Cha94b] which accounts for nonzero spins, and developed a new and easily applicable method for including spin effects in the exciton model. The exciton model spin distributions are derived by considering links with the FKK MSD theory. The exciton and MSD models have in common the use of leading particle quantum statistics, the on-shell approximation, and the independent-particle limit [Akk90, Kon91]. Furthermore, it is possible to see how the cross sections for 1-step and multistep processes in the exciton model can be obtained from the FKK theory. The exciton model spin dependence of residual nuclei can be obtained from the FKK MSD results in Eqs. (2.92) and (2.95) by replacing the l-dependent DWBA matrix elements by l-independent global energy averaged values, and also assuming an energy-angle factorization of the DWBA matrix elements, realizing that the resulting convolution of $1p1h$ densities yield $NpNh$ densities. This leads to a conclusion that the exciton model spin distribution of residual nuclei from a preequilibrium stage $N, P_N(J)$, can be estimated as

$$P_N(J) = \frac{(2J+1)}{(2I+1)(2i+1)}\sum_{S_f=0}^{1}\frac{1}{(2S_f+1)}\sum_{S=|I-S_f|}^{I+S_f}\sum_{l=|J-S|}^{J+S}R_n(l), \tag{2.96}$$

where $n = p + h = 2N$ and $\sum_J P_N(J) = 1$. If the FKK assumption of zero spins is made, this reduces to $P_N(J) = (2J+1)R_n(l)$. But using exact spins, and particular coupling in the target spin, results in a spin distribution boosted to higher spins than obtained with the zero-spin approximation.

Chapter 3

Experimental Technique

3.1 Measurement of prompt γ rays from neutron-induced reactions

The γ rays following particle emission from highly-excited compound nuclei formed by nuclear reaction processes contain important detailed information about the nuclei. The intensity of the γ rays, which can be measured directly, following particle emission is determined by the preceeding particle width. By changing the energies of the incident particles and observing the change of the intensities of the γ rays one can put the transitions into their proper location in the nuclear level scheme. The excitation energies of the states are usually available to fairly good accuracy from observation and measurement of the spectrum of the outgoing particle. The γ-ray data, which give us gamma-decay properties, are valuable for estimating, making, or checking the spin-parity assignments, and also can be converted into partial cross sections. γ-ray measurements are also useful for isolating the population of individual levels that could not be separated in the analysis of particle spectra. Measuring the intensities of γ rays resulting from the compound and continuum reactions gives the population of levels reached by the outgoing particle.

One experimental method to study neutron-induced reactions over a wide incident

neutron energy range up to several hundred MeV is the use of a pulsed "white" spallation neutron source and high-resolution γ-ray spectroscopy. The incident neutron energy is determined by the time-of-flight method and the prompt gamma-radiation emitted by neutron-induced reactions is detected by a high-resolution Ge detector array. In general, neutron-induced reactions leave the residual nucleus in a highly excited state which may subsequently decay via particle emission and a γ-ray cascade to the ground state. The initial intensity distribution over a very large number of highly excited levels is collected in the first few excited levels which then decay to the ground state. Such transitions between low-lying levels are identified in the prompt γ-ray emission spectrum by their characteristic γ-ray energies, and production cross sections for several transitions in a number of residual nuclei can be measured simultaneously over a wide incident neutron energy range in a single experiment. Because of the low neutron flux, relative to charged particle fluxes in ion-beam experiments, a fairly large amount of target material is required for this type of measurement.

3.2 Experimental devices

The very exciting progress of nuclear structure and nuclear reaction studies relies on the improved understanding of the microscopic aspects of nuclei, and the newly-developed experimental methods and devices have played an important, and sometimes decisive role. The highly-advanced accelerator technology has provided a variety of high-quality, high-intensity beams, such as light ions, heavy ions, polarized beams, etc. The in-beam γ-ray spectroscopic studies of nuclear properties benefited greatly from the development of new detection techniques in the last few decades. The use of multi-detector systems (a device composed of many detectors) in the 80s has made it possible to measure efficiently the multiplicity of the γ rays, their angular distributions, and coincidence relationships in the cascades. The Compton-suppression technique used on Ge detectors has significantly reduced the background in the γ-ray energy spectrum and allows the measurement of very

weak γ rays. The coverage of nearly 4π solid angle by a multi-detector system enables the measurement of the total energy of cascade γ rays.

The powerful computers for both on-line and off-line applications have been another aspect of recent developments in the experimental techniques. Advanced computer techniques have been used to control the operation of very complicated data-acquisition systems and to perform experiments with very high counting rates. It is also possible to perform sophisticated off-line data analysis, such as handling multi-dimensional matrix data. In the following subsections we will outline the γ-ray detectors and concentrate mainly on the discussion of detecting systems and data-acquisition systems at the Weapons Neutron Research (WNR) facility at the Los Alamos Neutron Science Center (LANSCE).

3.2.1 γ-ray detectors

An X-ray or γ-ray photon is uncharged and creates no direct ionization or excitation of the material through which it passes. The detection of γ rays is therefore dependent on causing the photon to undergo an interaction that transfers all or part of the photon energy to an electron in the absorbing material. In the field of γ-ray spectroscopy, there are two types of commonly-used detectors: sodium iodide (NaI) and germanium (Ge). The NaI scintillator has quick time response to the photons induced by incident γ rays, and therefore has good time resolution ($\approx$3 ns). The photons emitted in the NaI crystal are collected and converted into photoelectrons by an attached phototube. The induced photoelectrons are then amplified in the phototube and produce the energy-time signals whose shape carries collecting time information and whose magnitude is proportional to the corresponding γ-ray energy deposited in the crystal. Due to the many complicated process on the formation of the photo-signals in the crystal, conversion to photoelectrons in the phototube, and fluctuations in the amplifying process, the NaI detector has poor energy resolution (10-15%). Using modern technology, one can build a very large volume NaI crystal with a relatively high detection efficiency for γ rays up to a few MeV.

A Ge detector is composed of a germanium crystal operating under high voltage

and at liquid nitrogen temperature. The incident γ rays are absorbed by electrons in the Ge crystal and produce a large number of electron-hole pairs. These electron-hole pairs are collected by the corresponding electric poles and produce sizeable pulses which then can be recorded as events. As in the NaI spectrum, the height of the collected pulses is proportional to the γ-ray energy lost in the crystal, but the time information carried by the pulses is related to the drifting time of electron-hole pairs in the crystal. Normally this time feature is much worse than that of a NaI detector. However, the energy resolution is much better due to the significant reduction of statistical fluctuations of the electron-hole pairs collected.

The earlier version of Ge detectors was a Ge(Li) (lithium drifted) which had to be kept at liquid nitrogen temperature all of the time, in order to avoid the redistribution of lithium atoms in the germanium crystal and to reduce the noise level. Since the early 1980's the High-Purity Germanium (HPGe) detector has been widely used since it can be stored at room temperature and only cooled during the experiment. Due to the limitation of available Ge crystal size, the peak efficiency cannot be made as large as that for NaI; a typical Ge crystal often used in detectors may have, for example, up to 50% of that for a 3×3 in NaI(Tl) crystal at a distance of 25 cm. The detection efficiency also depends on the γ-ray energy: a decrease of efficiency is expected for high-energy γ rays, while the detector has less sensitivity to very low-energy γ rays as well, due to absorption by extra materials (such as aluminum) covering the detector crystal. A coaxial-shape Ge detector has better efficiency than a planar shape, especially for high-energy γ rays. However, due to the unevenness of the drift time of electron-hole pairs to the electronic poles, especially for interaction events occuring near the front of the detector, the coaxial detector has worse time resolution than the planar.

Many incident γ rays undergo Compton scattering, and escape from the Ge crystal as a result of size limitation. This causes a large continuum background (Compton background) below the full-energy photopeak. One way to overcome this disadvantage is to surround the Ge detector with a high-efficiency crystal which detects the escaped photons from the Ge

crystal and subsequently provides a veto signal to all those cases (so-called anti coincidence). NaI(Tl) scintillators have been extensively used as anti-Compton shields for a long time, but the high-density bismuth germinate ($Bi_4Ge_3O_{13}$ or BGO) crystal is more favored for the use in a multi-detector system because of its large absorption coefficient for γ rays. Therefore a similar suppression effect can be achieved by using a smaller size of BGO crystal in comparison with NaI. However, since the light output for a given γ ray is much larger in NaI than in BGO, sometimes a combination of NaI and BGO shields is used to obtain an optimal suppression effect: NaI for absorbing low-energy photons (normally at backward angles) and BGO for high-energy photons (forward angles).

Figure 3.1 illustrates an example of a coax detector unit of GEANIE array surrounded by a Compton suppression system made up of NaI(Tl) and BGO scintillators. The Compton shield is composed of several optically isolated segments, each with a photomultiplier tube to collect the escaped photons. The coaxial Ge detector is inserted in the BGO unit and cooled through a cold finger in the middle.

When Ge detectors are used under conditions in which fast neutrons may be present as a background, account must be taken of their effect on the recorded pulse height spectrum. The most obvious contribution is the appearance of spurious peaks that arise due to excitation of germanium nuclei by inelastic neutron scattering, followed by the emission of de-excitation γ rays or X-rays. The neutron-induced peaks ("neutron bumps") are usually identified easily in the spectrum because their width is much larger than that of gamma-induced peaks. This peak broadening takes place because a fraction of the excitation energy goes into the recoiling germanium nucleus, which subsequently contributes a variable yield of electron-hole pairs, adding to those created by the de-excitation radiation.

3.2.2 The GEANIE array

The experimental data were obtained at the Los Alamos Neutron Science Center (LANSCE) Weapons Neutron Research (WNR) facility. A schematic diagram of the experimental setup is shown in Fig. 3.2.

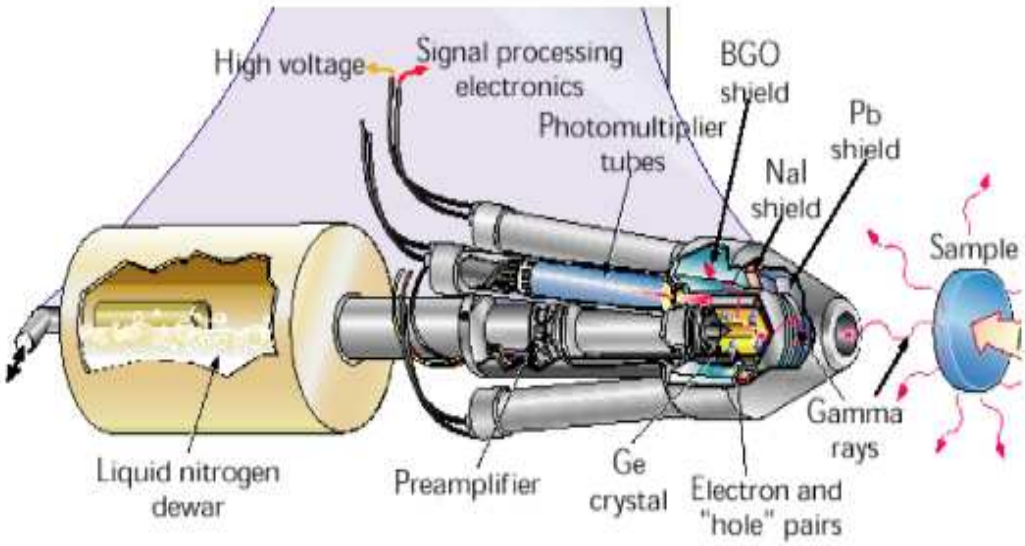

Figure 3.1: Coax detector surrounded by a Compton suppression system made up of NaI(Tl) and BGO scintillators.

At the WNR facility, spallation neutrons are produced by bombarding a natural tungsten target with an 800-MeV pulsed proton beam from the LANSCE linac. The pulsed proton beam consists of micropulses 1.8 μs apart, bunched into macropulses 625 μs in duration. Spallation neutrons with energies ranging from a few keV to nearly 800 MeV are produced. The intensity of the "white" neutron spectrum decreases nearly exponentially with increasing neutron energy. Beam-hardening material (1.5 cm of lead) was placed in the neutron flight path. The neutrons were collimated to a circular beam spot about 1.5 cm in diameter at the scattering-sample position. The scattering sample consisted of 3.3 grams of TiO_2 in the form of disks 2.4 cm diameter, enriched to 99.81% ^{48}Ti. The γ rays were detected with the GEANIE (GErmanium Array for Neutron Induced Excitations) spectrometer, located about 20 m from the neutron source on the 60° right flight path. For

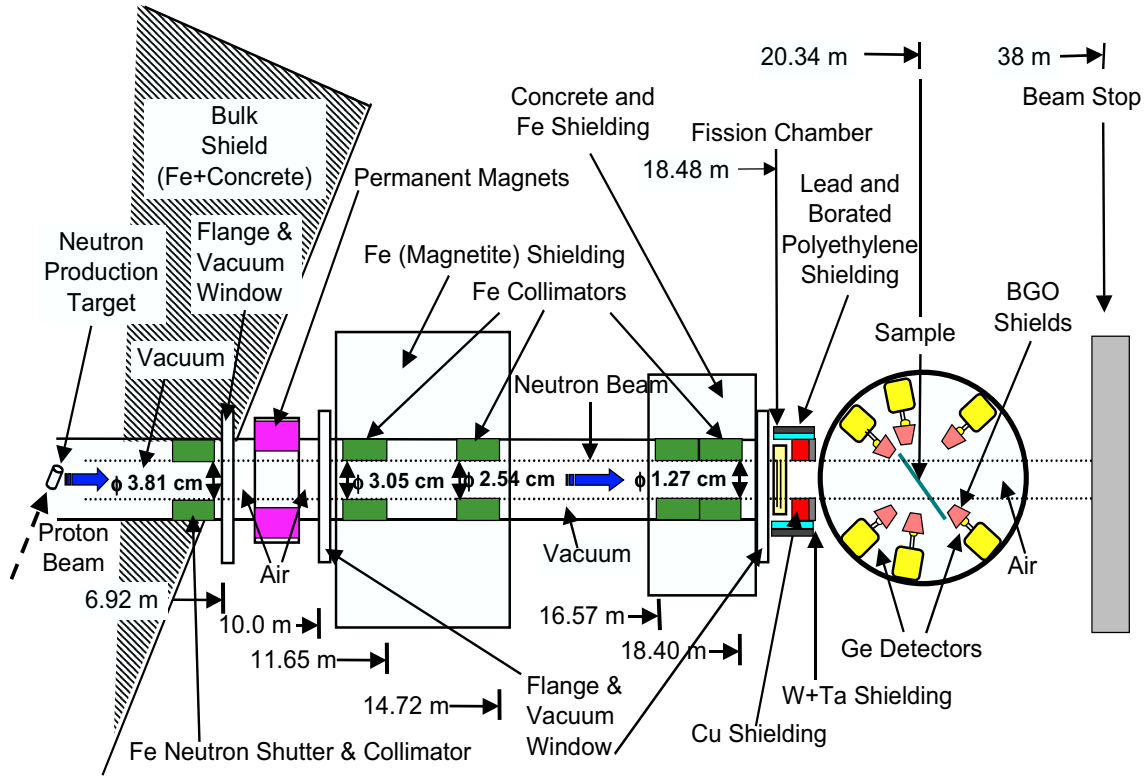

Figure 3.2: Schematic diagram of the experimental setup used in the experiment described in this thesis. The drawing is not to scale. Distances indicated by arrows are measured from the neutron production target.

this experiment, the GEANIE spectrometer consisted of 11 planar and 15 25% High-purity Ge (HPGe) coaxial detectors. All of the planars and 9 of the coaxial detectors were equipped with Compton suppression shields. The detectors were situated at a distance of ≈14 cm from the focal point where the scattering sample is located. The planar detectors were used to measure γ rays with energies less than 1 MeV and the coaxial detectors measured γ rays with energies up to 4 MeV. The planar detectors were arranged in rings at angles of 27.4° (four detectors), 58.4° (two detectors), 128.0° (one detector), and 142.7° (four detectors) with respect to the neutron beam direction. The coaxial detectors were arranged in rings at angles of 56.6° (two detectors), 77.7° (two detectors), 100.5° (four detectors), and 129.5° (one detector). The six remaining coaxial detectors were unsuppressed and their events

were only analyzed in $\gamma\gamma$ coincidence mode. The efficiency of the array has been calibrated through a series of source measurements, supplemented by detailed modeling [McN99] using the transport code MCNP [Bri86].

A fission chamber consisting of ^{235,238}U foils [Wen93] was located 2 m upstream from the GEANIE spectrometer. The neutron flux was determined using these fission foils. Neutron energies were determined by the time-of-flight (TOF) technique, using the detection time of the "flash" of γ rays caused by the spallation reaction with respect to the beam rf signal as a reference marker. The detection time of γ rays produced by neutrons interacting with the sample was used to calculate the TOF of the neutrons relative to the γ-flash detection time. Similarly, signals from the fission chamber were used to provide a flight time relative to the γ-flash detection time (also observed in the fission chamber). More extensive discussions of the LANSCE/WNR facility and the GEANIE spectrometer are given in references [Lis90] and [Bec97], and a summary of the experimental conditions is supplied in Section 3.3.

3.2.3 Electronics and data acquisition system

The data acquisition system consists of (1) electronic modules that perform hardware manipulations of experimental information such as time and energy signals from detectors, (2) the Xamine computer code that performs low-level software manipulations of the data events on fast CAMAC and VME bases, and (3) the VME interface that connects with the host computers where on-line and off-line data can be stored and analyzed. The schematic diagram of the electronics for the GEANIE array are shown in Fig. 3.3. The power supply for NaI phototubes and BGO shields is controlled by a multichannel high-voltage power supply, while for Ge detectors the high-voltage power is offered from a dialed module adjusted manually. Negative bias is added to detectors, about -1200 V on NaI shields, -1050 to -1200 V on BGO shields, and -2800 to -3000 V on Ge detectors. The pulses from Ge detectors are first preamplified and then sent to timing-filter amplifiers (TFA) to produce time signals and to linear amplifiers to provide energy signals. The energy signals

are digitalized through ADCs, while the TFA outputs are processed by constant fraction discriminators (CFD) to generate timing logic signals. The CFD fast signals are delayed and sent to a multiplicity logic unit. The analog signals from individual elements of an anti-Compton shield are summed and the output is sent to a discriminator to provide a logic signal. This logic signal is then sent to a logic unit together with the corresponding Ge signal to perform the Compton suppression.

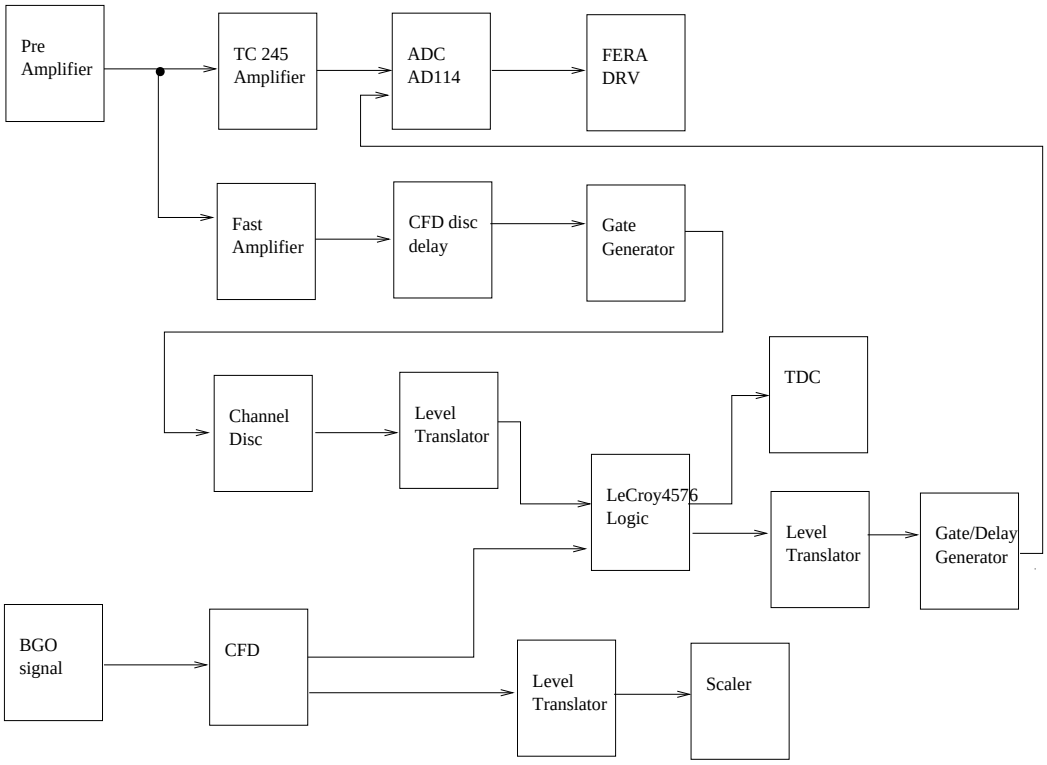

Figure 3.3: GEANIE detector circuit diagram.

The GEANIE detector trigger logic and RF circuit is shown in Fig. 3.4.

The data from the suppressed detectors were collected in singles-and-higher-fold mode, resulting in a total array rate of 2-3 kHz. For each unsuppressed γ-ray event, a master gate window of 20 μs was opened during which all unsuppressed pulses from the Ge detectors were processed. The data stream consisted of a bit determining whether the event occurred in or out of the macropulse, the time relative to the start of the macropulse (recorded in 100 ns intervals), energy E_γ, and (if in beam) time t_γ relative to the proton

micropulse for each detector which recorded an event.

Xamine is the Michigan State University data acquisition system used to access the shared memory in order to perform some online analysis and histogramming. Xamine is also used to store event data that include the escape-suppressed γ-ray pulse height and incident neutron TOF information for each detector. It consists of the various programs which form the software portion of the GEANIE acquisition system. Some of the programs are essential for the correct processing and recording of data to tape, others are useful to control and monitor the data flow. The essential programs are transsrc (establishes a link with the transputer board and passes data to router), router (routes data buffer to any programs which request them), iserver (provides a command I/O interface to the transputer) and taper (writes data from router to the tape in standard format). Other, useful programs for control and monitoring are geanie_xamine.v7, share, dumbclient, and parse. geanie_xamine.v7 histograms and displays data buffers from router. It also provides additional functions which include automated diagnostics and monitoring of data rates, beam status, selection of sort method for online data and reading and writing of spectra and matrices to a variety of formats. share is a tool which allows programs, which otherwise accept I/O only from the controlling terminal, to communicate with other programs via shared memory. dumbclient works in conjunction with share to display output from and send input to a program launched by share. parse is a debugging tool which interprets a list of hexadecimal words from the data buffer and displays the meaning of each word. Fig.3.5 describes the arrangement of these programs to control the flow of data. The arrows indicate the direction of flow of data and commands. Multiple copies of the client programs which communicate via share can be launched and run at the same time.

3.3 Summary of experimental details

The details of the n + ^{48}Ti experiment using GEANIE discussed in this dissertation are summarized in the tables below for easy reference. The data were acquired in two

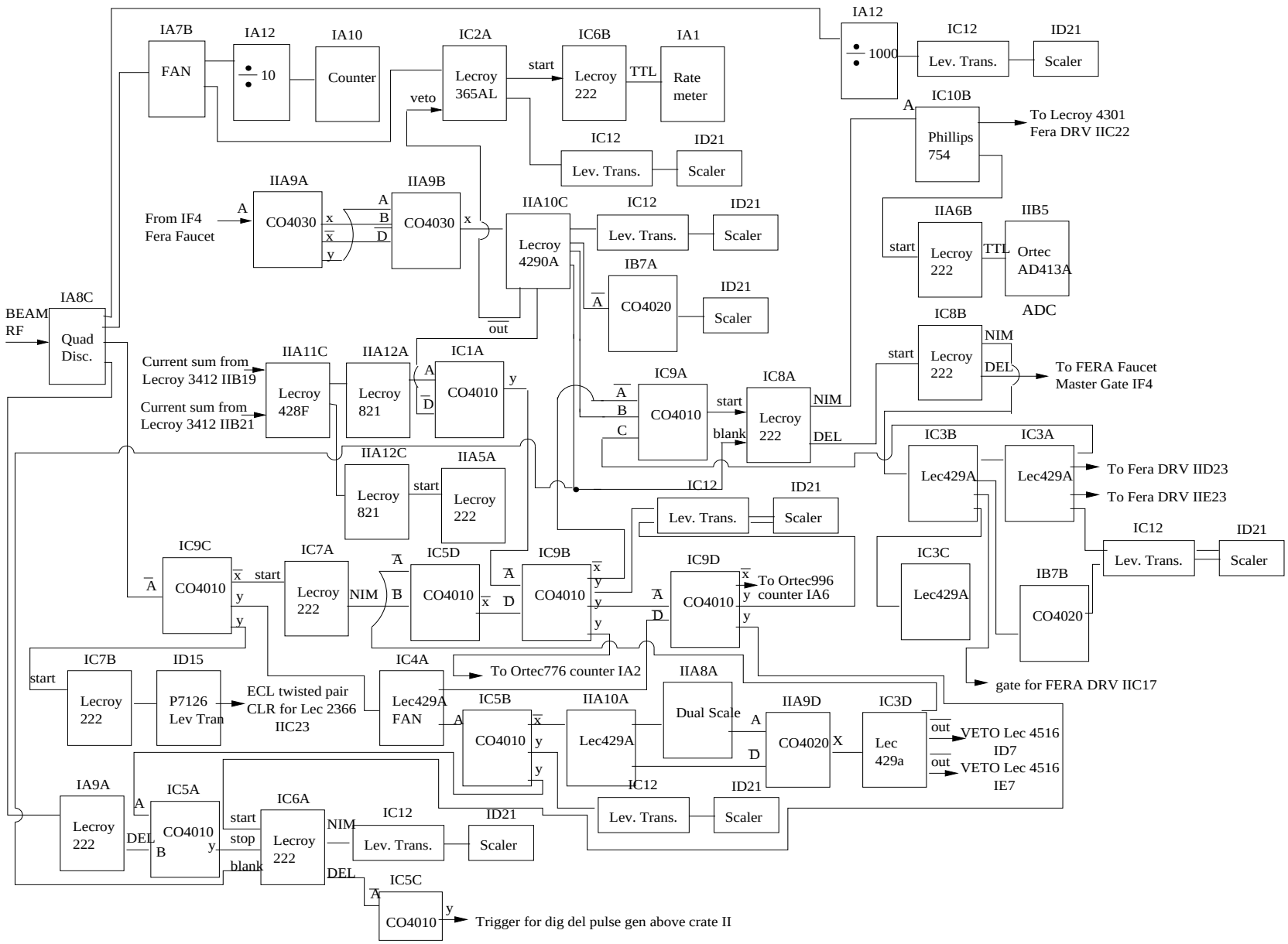

Figure 3.4: GEANIE beam RF circuit diagram.

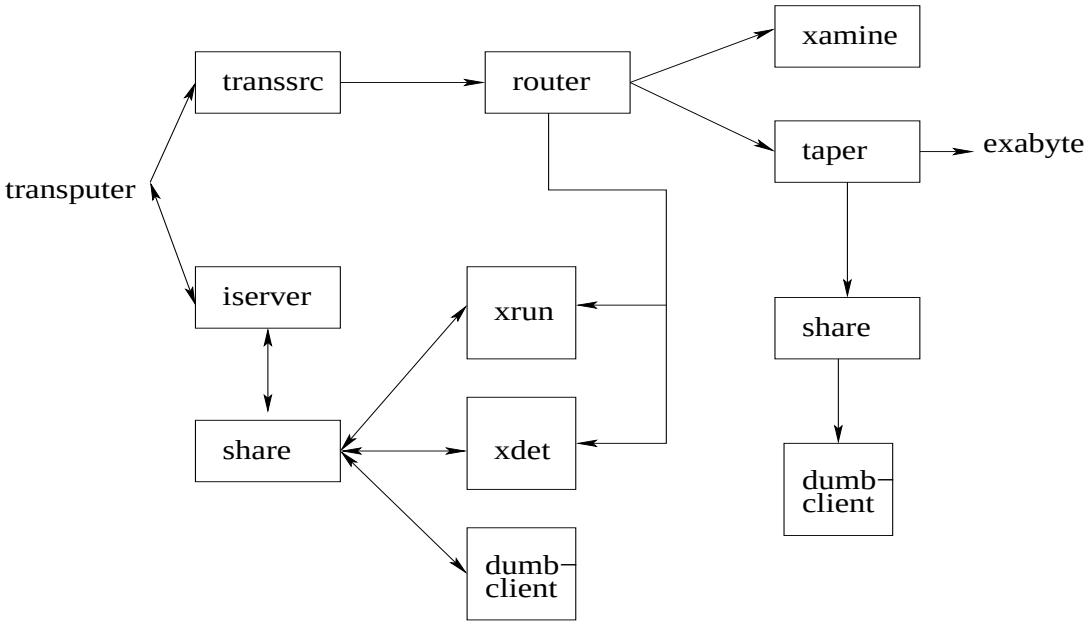

Figure 3.5: The flow of data.

separate sets of experimental runs: one with a ^{48}Ti sample, the other with a ^{48}Ti sample sandwiched between ^{Nat}Fe foils. The experimental parameters are summarized in Tables 3.1 and 3.2, respectively.

Table 3.1: Summary of experimental details for the n + ^{48}Ti experiment.

Quantity	Value
Data label	**48Ti01**
Run dates	10/10/01-10/15/01
Beam structure	
Rep. rate	100 Hz
Micropulse spacing	1.8 μs
Beam gate length	625 μs
Typical proton current	4.0 μA
Beam absorbers	0.6″ Pb
Sample areal density	0.7285 g/cm^2 (uncertainty unknown)
Sample thickness	$\approx$ 1.7 mm
Sample atomic assay	99.81% ^{48}Ti
Sample orientation	251° on dial (109° with respect to beam)
Detector absorbers	none
Deadtimes	
Planar-data sum	62.0%
Coaxial-data sum	58.0%
^{235}U fission foil	52.0%
^{238}U fission foil	50.9%
Typical array rate	2100 Hz (total γ-or rate)
Total counts:	4.6×10^8

Table 3.2: Summary of experimental details for the n + ^{48}Ti experiment with iron foils.

Quantity	Value
Data label	**48Ti03**
Run dates	08/28/03-08/31/03
Beam structure	
Rep. rate	100 Hz
Micropulse spacing	1.8 μs
Beam gate length	625 μs
Typical proton current	3.2 μA
Beam absorbers	0.75″ black poly, 0.5″ Pb
Sample areal density	0.7285 g/cm^2 (uncertainty unknown)
Sample thickness	$\approx$ 1.7 mm
Sample atomic assay	99.81% ^{48}Ti
Sample orientation	251° on dial (109° with respect to beam)
Detector absorbers	none
Deadtimes	
Planar-data sum	60.8%
Coaxial-data sum	55.4%
^{235}U fission foil	60.0%
^{238}U fission foil	50.1%
Typical array rate	2900 Hz (total γ-or rate)
Total counts:	4.4×10^8

Chapter 4

Data Analysis Overview

4.1 Introduction

Due to the development of more advanced experimental techniques, researchers now can measure more and more complicated γ-ray spectra by using high-resolution germanium detectors and multi-detector arrays. The use of Compton-suppressed Ge detectors is a new technique in studying the reaction dynamics of neutron-induced reactions. The use of partial γ-ray cross sections to determine reaction cross sections for actinide nuclei is superior to other techniques because the production of neutrons from fission interferes with direct measurements of (n,xn) [x=1,2,3,...] reactions. The good peak-to-total ratio of the GEANIE detectors assists in observing individual low-lying γ-ray lines above the continuum from fission and other γ rays, and the good energy resolution of the detectors allows unique transition assignments. At the same time the question arises how to handle and analyze these complicated γ-ray spectra.

A typical γ-ray spectrum from neutron-induced reactions contains hundreds of peaks. The identification of these γ rays in GEANIE data can be complicated due to the large number of open reaction channels. The analysis of threshold energies in the γ-ray excitation functions is helpful in identifying and placing γ rays. Also the coincidence requirement of Ge detectors in the experiment and the off-line creation of two-dimensional

$\gamma\gamma$ coincidence matrices are very useful, especially for reaction channels that open up at high neutron energy (>20 MeV). From the coincidence relationships of γ rays, which are observed by common "gating" techniques, one is able to establish the decay scheme of the nucleus.

Before describing the details of the extraction of the partial cross sections, first consider the time-of-flight technique used to determine incident neutron energies. Then the analysis of γ-ray spectra will be considered.

4.2 Time-of-flight technique

Neutron energies were determined using the technique discussed in Section 3.2; the TOF spectrum for planar data is shown in Fig. 4.1. The distance traveled by both neutrons and γ rays from the spallation source to the focal point of the GEANIE spectrometer is d = 20.34 m. The time-of-flight (TOF) relative to the γ flash is determined relativistically. The γ-ray TOF is simply d/c, where $c \approx 0.300$ m/ns is the speed of light in vacuum. Similarly, the TOF of a neutron with kinetic energy E_n is d/v, where classically

$$E_n = \frac{1}{2}mv^2, \tag{4.1}$$

and m is the neutron rest mass. The TOF of the neutron relative to the γ ray is given by

$$\delta t = \frac{d}{v} - \frac{d}{c} = \frac{d}{c}\left(\sqrt{\frac{mc^2}{2E_n}} - 1\right). \tag{4.2}$$

Using the neutron rest energy $mc^2 = 939.56$ MeV, one obtains, for example, the TOFs

$$E_n = 1.0\ MeV \Rightarrow \delta t = 1401.72\ ns \tag{4.3}$$

$$E_n = 20\ MeV \Rightarrow \delta t = 260.80\ ns. \tag{4.4}$$

In the TOF spectrum, the γ flash can be seen at channel position $x_{flash} = 202$ (each channel corresponds to 0.5 ns). The TOFs calculated in equations 4.3 and 4.4 correspond to channel positions:

$$x_{min} = (202 + 1401.72/0.5) = 3005 \tag{4.5}$$

$$x_{max} = (202 + 260.80/0.5) = 724, \tag{4.6}$$

where the x-channel number is rounded to the nearest integer. These classical values are in good agreement with the relativistic values $x_{min} = 3007$ and $x_{max} = 737$. The relativistic values were used to set the time condition on the TOF spectra to obtain the corresponding pulse-height spectra [You01]. Fig. 4.2 shows the spectrum obtained with the coaxial HPGe detectors after selecting time gates corresponding to E_n = 1-20 MeV neutrons. There is a large background present from interactions in the Ge crystals that obscure γ rays in these regions.

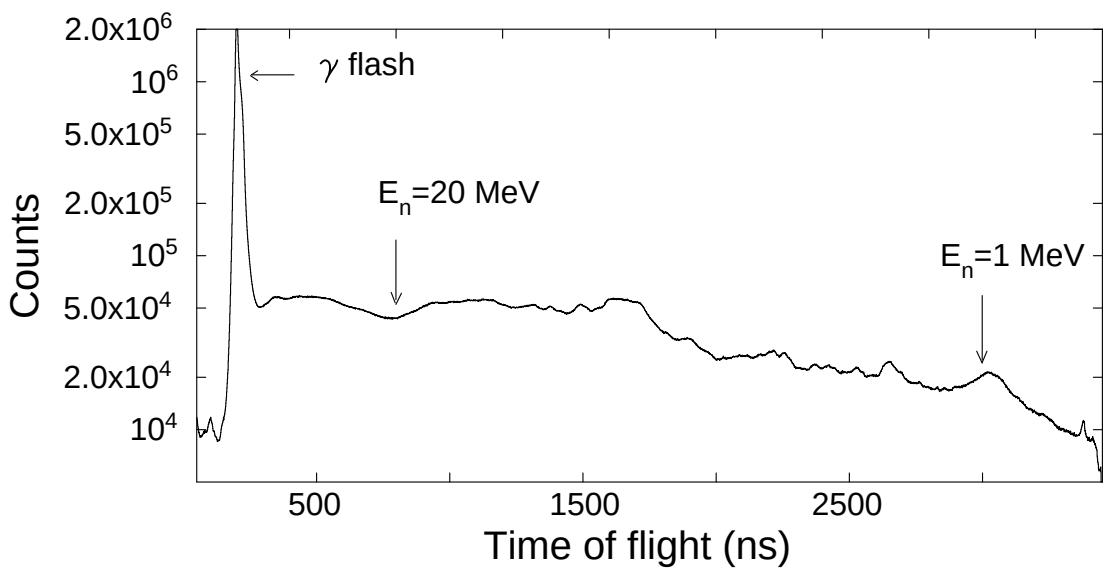

Figure 4.1: Time-of-flight spectrum.

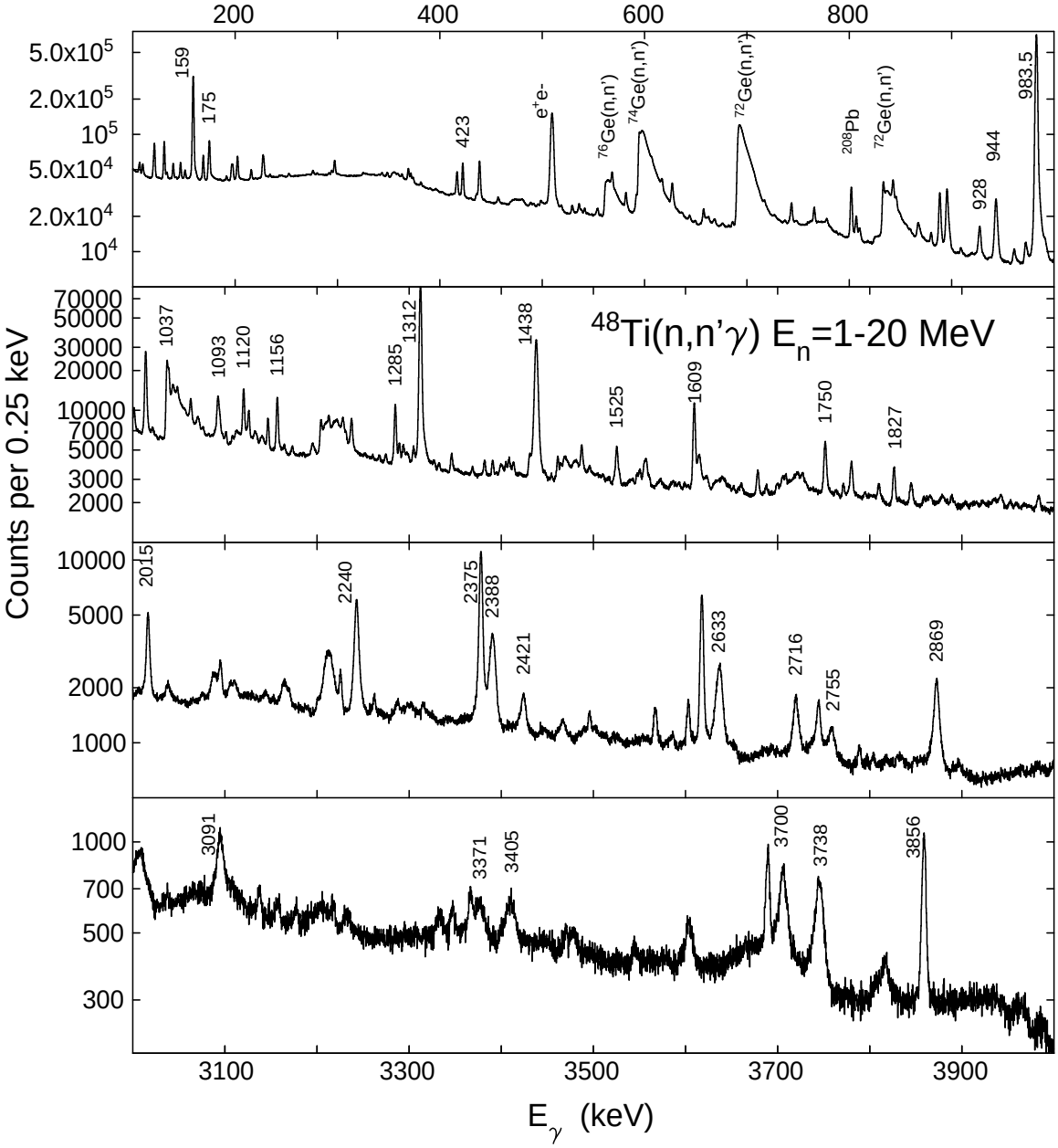

Figure 4.2: Spectrum obtained from the sum of the coaxial detectors for the ^{48}Ti(n,n$'\gamma$) reaction. The condition on the time of flight corresponds to E$_n$=1-20 MeV neutrons. Some of the more prominent transitions in ^{48}Ti are labeled with their energies.

4.3 Analysis of γ-ray spectra

4.3.1 Peak-shape and background fit parameters

The analysis of γ-ray and particle spectra through peak-fitting is an important part of all nuclear experimental work. Over the years, the field has seen the development of a variety of computer programs for the analysis of γ-ray spectra. The γ-ray spectra analyzed were fit using a new peak-fitting code, XGAM [You]. The code was developed specifically to process complex GEANIE spectra which result from neutron-induced reactions, by constraining peak shapes through a consistent fit of the entire spectrum at once. In order to enable global fits, XGAM provides an unlimited number of peaks, complex peak-shapes to model γ- and x-rays as well as neutron bumps with high- and low-energy tails and Gaussian asymmetries. The parameters used in the fit to the sum of planar data are summarized in Table 4.1, and the corresponding fit to the $E_n = 1-20$ MeV projection is shown in Fig 4.3. Similarly, the parameters for the coaxial-sum fit are given in Table 4.2.

The peak shapes are parameterized as a Gaussian function with an energy-dependent width given by

$$w(x) = \sqrt{w_0^2 + w_1^2 \left(\frac{x}{1000}\right) + w_2^2 \left(\frac{x}{1000}\right)^2}, \tag{4.7}$$

where x is the channel position of the peak centroid, related to the γ-ray energy through the calibration discussed in Section 4.3.3. Further components are added to the Gaussian shapes to simulate the realistic response of the germanium detectors. A high-energy tail is produced using a Gaussian function convoluted with an exponential decay. The magnitude of the high-energy tail is given by R_h, and the decay constant is β_h. A smoothed step function simulates Compton effects, with a magnitude set by the parameter S. A Gaussian asymmetry term, discussed in [Ker70], is also included with a magnitude set by the energy-dependent parameters p_3 and p_4.

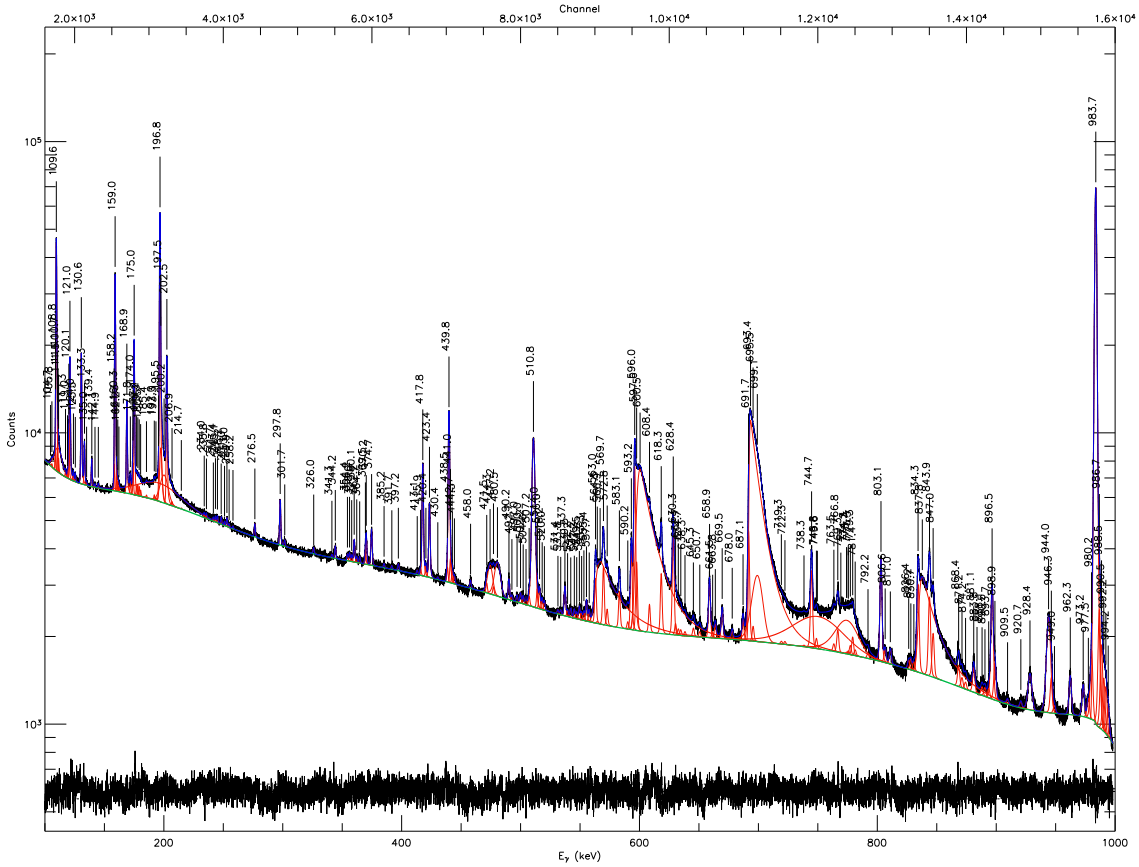

Figure 4.3: Plot of fit **planar** to planar-data sum spectrum (see Table 4.1). The data are shown as a black histogram, the fit is plotted as a blue line, and the background (polynomial + Compton step) is shown in green, the residual spectrum is plotted at the bottom. Individually-fitted peaks are plotted in red.

4.3.2 Efficiency of Ge detectors

The efficiency of a Ge detector depends on the physical and electronic configuration during the experiment. If X-ray absorbers are used in front of the Ge detectors, the detecting efficiency for low-energy γ rays will be reduced and the amount of reduction depends on the type of absorber used. The high-energy efficiency, however, is little affected; for the same types of detectors (coaxial shapes in the current work), this part of the efficiency curve as a function of energy should be quite similar. The γ-ray absolute efficiency curves for planar and coaxial detectors were calculated for GEANIE data using a Monte-Carlo simulation

Table 4.1: Parameters used in the fit to the planar-data sum spectrum. The peak-shape parameters are explained in the text. The last row gives the χ^2 per degree of freedom for the fit.

Parameter	Value
Fit label	**planar**
E_n range	1–20 MeV
Channel range fitted	x = 1600–15970
Background polynomial order	12
Number of peaks	192
w_0	10.80
w_1	4.70
w_2	1.68
R_h	15.12
β_h	15.05
S	0.00131
p_3	$4.12 \times 10^{-3} + 1.76 \times 10^{-6}x$
p_4	$1.28 \times 10^{-6} + 5.87 \times 10^{-11}x$
χ^2/ν	1.53

of the array [Bri86, McN99]. Calculated absolute efficiency curves for planar and coaxial detector sets are shown in Figs. 4.4 and 4.5, respectively. The calculated efficiency curves are corrected for beam-profile and target-geometry effects. The Monte-Carlo simulation for coaxial detectors was performed for γ ray energies between 300 keV and 1800 keV. The efficiency curve for coaxial detectors was extrapolated to high energies and verified with γ-ray reference sources. The calculated efficiencies can be checked against efficiencies exctracted from measured branching ratios. Known branching ratios of γ-ray decays from planar-detector data were fitted using a 7-parameter relative-efficiency formula

$$\epsilon(E_\gamma) = exp\left\{-\left[(A + Bx + Cx^2)^{-G} + (D + Ey + Fy^2)^{-G}\right]^{-1/G}\right\}, \tag{4.8}$$

where A, B, C, D, E, F, and G are adjustable parameters. The empirical efficiency curve obtained in this manner is compared to the calculated efficiencies for planar-detector data.

Table 4.2: Parameters used in the fit to the coaxial-data sum spectrum. The peak-shape parameters are explained in the text. The last row gives the χ^2 per degree of freedom for the fit.

Parameter	Value
Fit label	**coax**
E_n range	1–20 MeV
Channel range fitted	x = 600–16000
Background polynomial order	12
Number of peaks	472
w_0	6.21
w_1	0.05
w_2	1.20
R_h	13.98
β_h	8.84
S	0.017
p_3	$1.01 \times 10^{-2} + 1.90 \times 10^{-6}x$
p_4	$1.73 \times 10^{-7} + 2.35 \times 10^{-10}x$
χ^2/ν	1.87

The agreement between experimental and calculated efficiency curves was excellent [You03].

4.3.3 Beam-on γ-ray calibration

The γ-ray energy calibration is performed using beam-on γ-ray transitions with well-known energies. These include transitions produced by the n+^{48}Ti reaction, as well as standard background transitions observed in all GEANIE experiments. A summary of the calibration transition used for the planar and coaxial data can be found in Tables 4.3 and 4.4, respectively. The relationship between accepted energies, E_γ^{true}, and the channel position in the GEANIE spectrum is fit with a straight line. The residual of this fit, E_γ^{true}-E_γ^{lin}, is then fit using a polynomial of order 6 for planar and coaxial data. The calibration curves are shown in Figs. 4.6 and 4.7 for planar and coaxial data, respectively.

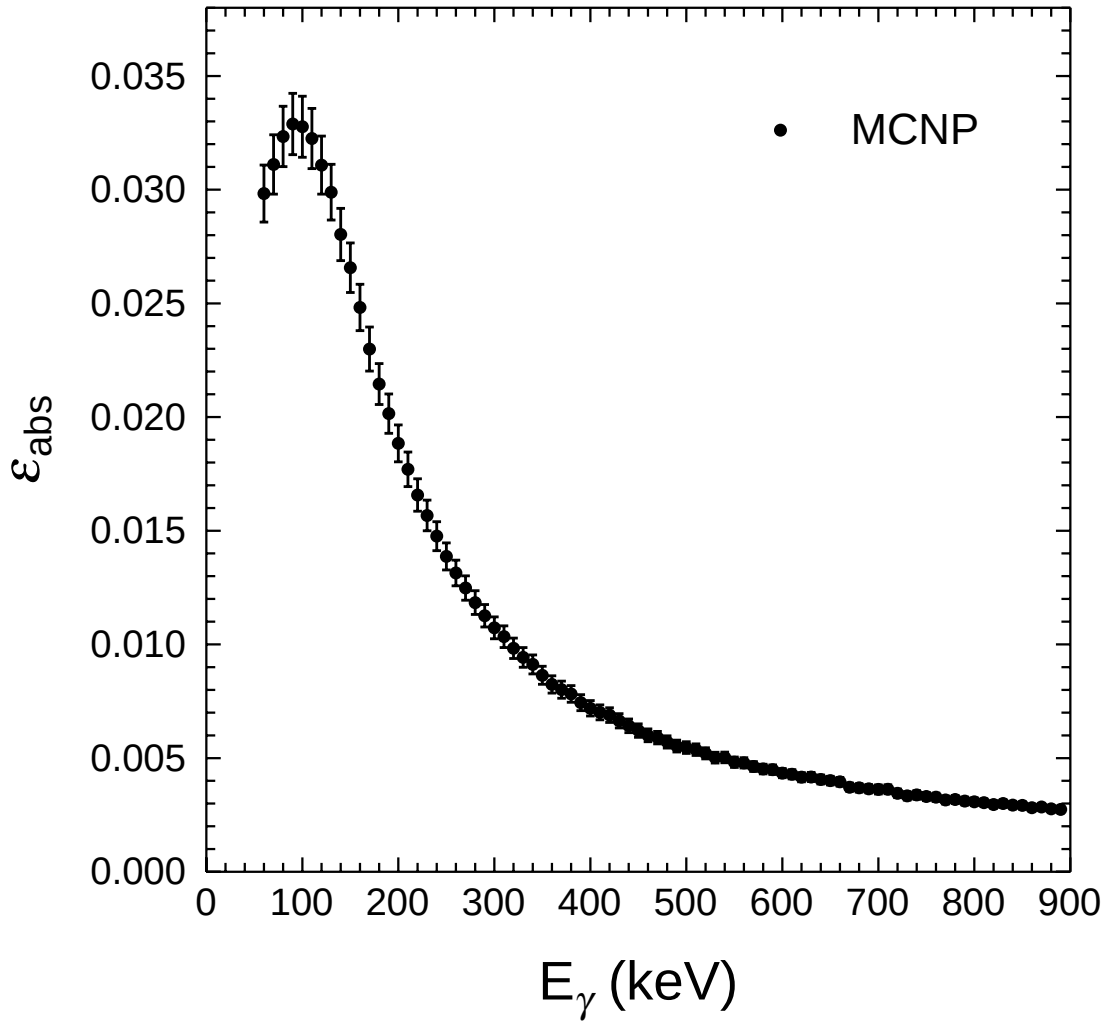

Figure 4.4: Efficiency curve for the sum of planar data, calculated using the code MCNP [Bri86, McN99].

Table 4.3: Calibration transitions used in the planar fit. The average deviation from the accepted energy is 8 eV, with a standard deviation of 146 eV.

$E_\gamma^{(true)}$ (keV)	$E_\gamma^{(cal)}$ (keV)	$E_\gamma^{(true)}$-$E_\gamma^{(cal)}$ (keV)	Identification
109.894(5)	109.891(7)	0.003	`19F@109.9`

Table 4.3: (Continued.)

$E_\gamma^{(true)}$ (keV)	$E_\gamma^{(cal)}$ (keV)	$E_\gamma^{(true)}$-$E_\gamma^{(cal)}$ (keV)	Identification
121.410(40)	121.503(8)	-0.093	`48Sc@252.35`
130.940(40)	131.092(10)	-0.152	`48Sc@130.94`
159.369(20)	159.321(11)	0.048	`47Ti@159.4`
175.361(50)	175.420(8)	-0.059	`48Ti@3508.5`
197.143(4)	197.141(5)	0.002	`19F@197.1`
202.860(10)	202.872(6)	-0.012	`127I@202.9`
370.290(50)	370.230(30)	0.060	`48Sc@622.64`
423.629(9)	423.631(13)	-0.002	`48Ti@3782.44`
458.450(160)	458.159(66)	0.291	`48Ti@4196.83`
537.470(40)	537.510(42)	-0.040	`206Pb@1340.5`
669.600(70)	669.540(56)	0.060	`207Bi@669.6`
744.700(90)	744.624(36)	0.076	`127I@744.7`
803.060(30)	803.080(30)	-0.020	`206Pb@803.0`
811.198(18)	810.897(159)	0.301	`48Ti@4035.115`
896.280(60)	896.669(38)	-0.389	`209Bi@896.3`
928.290(11)	928.331(103)	-0.041	`48Ti@3223.9`
944.104(7)	943.897(100)	0.207	`48Ti@3239.7`
972.910(30)	972.980(114)	-0.070	`48Ti@4196.8`
983.517(5)	983.518(8)	-0.001	`48Ti@983.5`

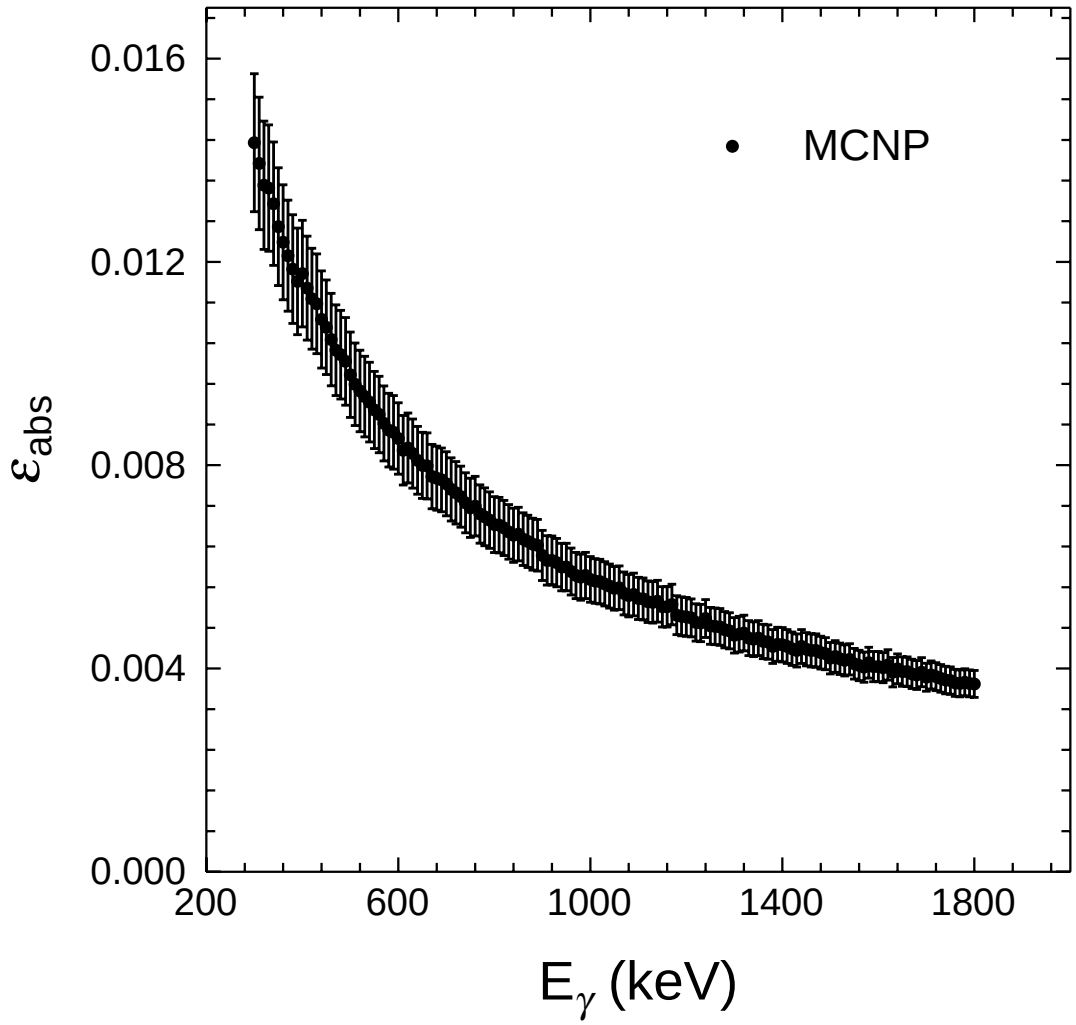

Figure 4.5: Efficiency curve for the sum of coaxial data, calculated using the code MCNP [Bri86, McN99].

Table 4.4: Calibration transitions used in the coax fit. The average deviation from the accepted energy is -34 eV, with a standard deviation of 350 eV.

$E_\gamma^{(true)}$ (keV)	$E_\gamma^{(cal)}$ (keV)	$E_\gamma^{(true)}$-$E_\gamma^{(cal)}$ (keV)	Identification
159.369(20)	158.945(13)	0.424	`47Ti@159.4`

Table 4.4: (Continued.)

$E_\gamma^{(true)}$ (keV)	$E_\gamma^{(cal)}$ (keV)	$E_\gamma^{(true)}$-$E_\gamma^{(cal)}$ (keV)	Identification
175.361(50)	174.906(11)	0.455	`48Ti@3508.5`
197.143(4)	197.384(14)	-0.241	`19F@197.1`
423.629(9)	423.558(10)	0.071	`48Ti@3782.44`
458.450(160)	458.045(32)	0.405	`48Ti@4196.83`
811.198(18)	811.266(28)	-0.068	`48Ti@4035.115`
928.290(11)	928.278(12)	0.012	`48Ti@3223.9`
944.104(7)	944.105(13)	-0.001	`48Ti@3239.7`
972.910(30)	972.941(18)	-0.031	`48Ti@4196.8`
983.517(5)	983.538(5)	-0.021	`48Ti@983.5`
1037.599(26)	1037.553(9)	0.046	`48Ti@3333.178`
1063.190(50)	1063.270(19)	-0.080	`48Ti@3358.8`
1195.830(60)	1195.671(72)	0.159	`48Ti@3616.784`
1312.096(6)	1312.073(6)	0.023	`48Ti@2295.6`
1430.220(40)	1430.827(96)	-0.607	`47Ti@2682.31`
1437.487(11)	1437.448(9)	0.039	`48Ti@2421.023`
1479.339(18)	1479.329(112)	0.010	`48Ti@4719.1`
1486.820(30)	1486.809(29)	0.011	`48Ti@3782.436`
1614.041(19)	1614.140(36)	-0.099	`48Ti@4035.1`
2013.660(45)	2014.607(21)	-0.947	`48Ti@2997.19`
2036.349(13)	2036.520(146)	-0.171	`48Ti@4457.42`

Table 4.4: (Continued.)

$E_\gamma^{(true)}$ (keV)	$E_\gamma^{(cal)}$ (keV)	$E_\gamma^{(true)}$-$E_\gamma^{(cal)}$ (keV)	Identification
2161.759(14)	2161.873(129)	-0.114	48Ti@4457.4
2240.375(19)	2240.306(23)	0.069	48Ti@3223.924
2375.211(19)	2375.058(19)	0.153	48Ti@3358.8
2387.249(26)	2387.530(37)	-0.281	48Ti@3370.842
2633.200(30)	2633.167(40)	0.033	48Ti@3616.784
2715.810(130)	2716.216(59)	-0.406	48Ti@3699.45
2868.590(40)	2868.581(54)	0.009	48Ti@3852.23
3090.820(60)	3090.605(145)	0.215	48Ti@4074.5
3403.830(70)	3404.952(247)	-1.122	48Ti@4387.654
3699.110(120)	3699.160(180)	-0.050	48Ti@3699
3738.350(240)	3738.027(179)	0.323	48Ti@3738
3808.580(70)	3807.934(551)	0.646	48Ti@4792.25

4.4 Extraction of the excitation functions

The excitation functions were obtained by applying TOF gates 15 ns wide on the γ-ray events in the interval to $E_n = 1$ to 20 MeV. For each TOF bin, a 1D γ-ray pulse-height spectrum was generated and fitted with the computer code XGAM [You] with peak shape parameters and background levels determined from a global fit to the spectrum. These parameters are listed in Section 4.3.1. XGAM extracts γ-ray peak areas from a spectrum. Fitted peaks in the spectrum were identified by comparison with accepted γ-ray energies,

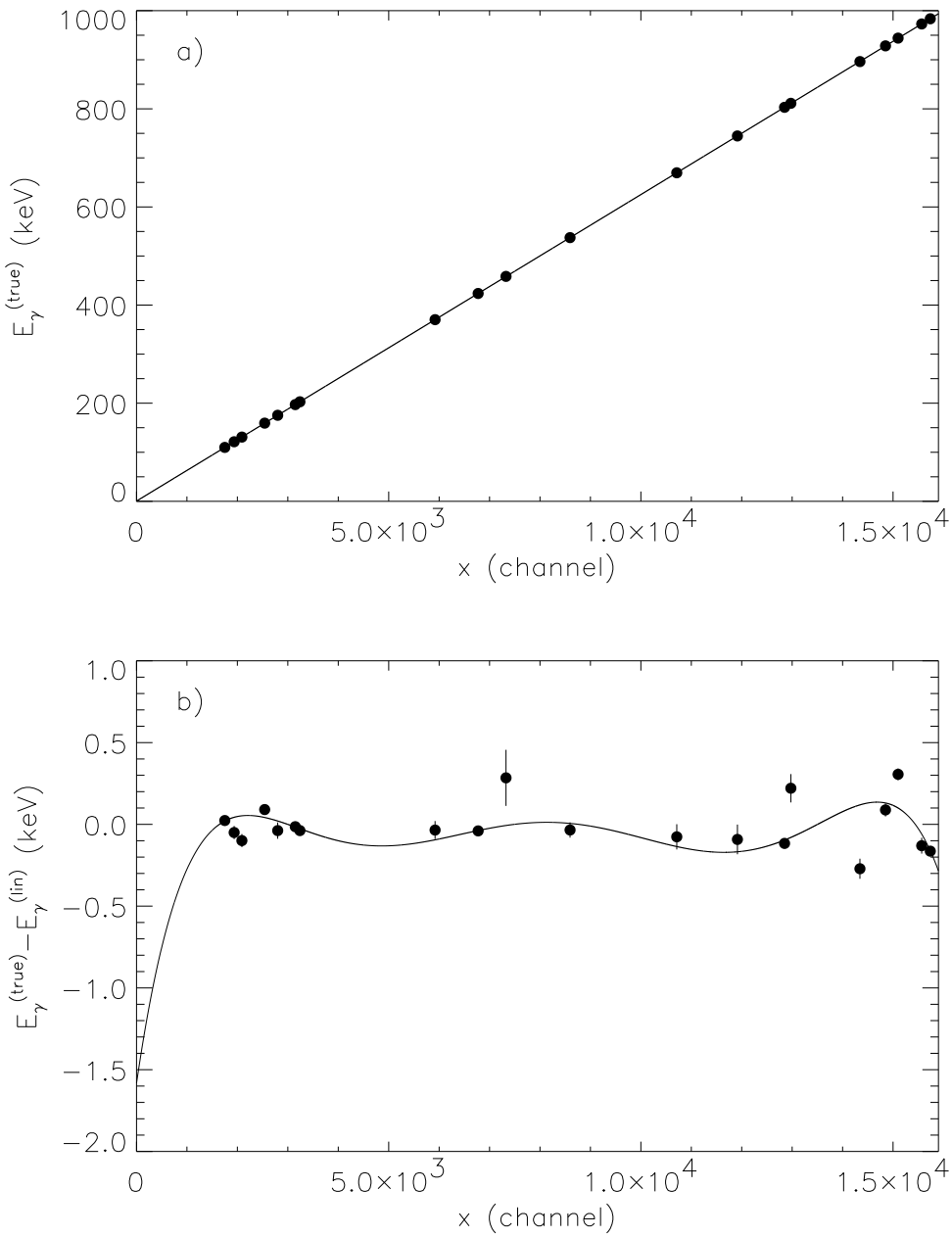

Figure 4.6: γ-ray energy calibration for the planar-detector data: a) linear calibration and b) sixth-order polynomial non-linearity correction.

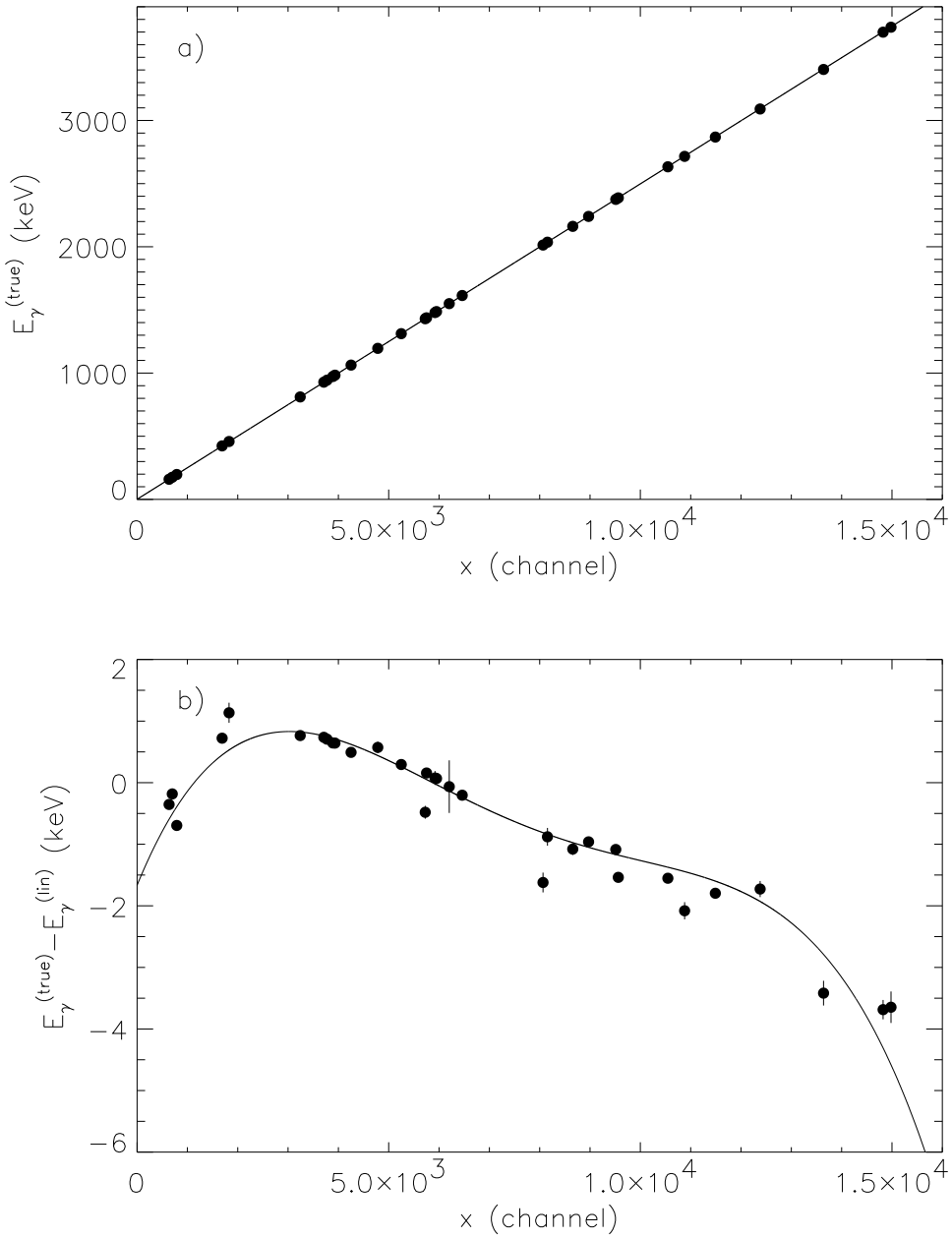

Figure 4.7: γ-ray energy calibration for the coaxial-detector data: a) linear calibration and b) sixth-order polynomial non-linearity correction.

tabulated in the NUDAT database [nud]. Partial γ-ray cross sections for transitions were obtained using the following formula

$$\sigma_\gamma(E_n) = (1+\alpha_\gamma) * \frac{\epsilon_{fc}}{\epsilon_{Ge}} * \frac{LT_{fc}}{LT_{Ge}} * \frac{1}{a_s}\frac{A_\gamma}{N_n}, \tag{4.9}$$

where α_γ is the internal conversion coefficient, ϵ_{Ge} and ϵ_{fc} are the detection efficiency of the Germanium detectors and fission chamber (respectively), LT_{Ge} and LT_{fc} are the live times of the Germanium detectors and fission chamber, a_s is the areal density of the ^{48}Ti sample, A_γ the γ-ray peak area, and N_n the number of neutrons counted in the fission chamber.

The internal conversion coefficients are taken from the NUDAT [nud] database. The neutron flux used in Eq. (4.9) can be determined from either the ^{235}U or the ^{238}U foil in the fission chamber. The ^{238}U foil has been used consistently to extract partial γ-ray cross sections, in order to avoid the wrap-around problem arising in the incident neutron beam structure (since the flight path is long enough that low energy neutrons arrive at the target location at the same time as high-energy neutrons from a later pulse). The pulse height and time-of-flight data from the ^{238}U fission chamber are shown in Fig. 4.8. In Fig. 4.8(a), the pulse height spectrum is shown as determined from the beam-on data. The vertical line indicates the lower limit of the gate taken on the pulse height in order to separate "α" events from fission events. In this case, "α" events include those resulting from the natural α decay of ^{238}U and those originating from neutron-induced reactions on the backing material. Fig. 4.8(b) shows the raw TOF spectrum obtained without any gating conditions placed on the pulse height spectrum. The TOF spectrum in Fig. 4.8(c) is fission gated, and is converted to a neutron intensity spectrum by using the known ^{238}U(n,f) cross sections [end91], and taking the efficiency for the fission detector to be $\epsilon = 0.97$ [McN99]. The TOF bins correspond to the same neutron energies as for the γ-ray events, with the photofission events used as the reference time. The fission-chamber live time is determined by taking the ratio of beam-on ADC events to the total number as given by a scaler-module count, gated by the beam envelope.

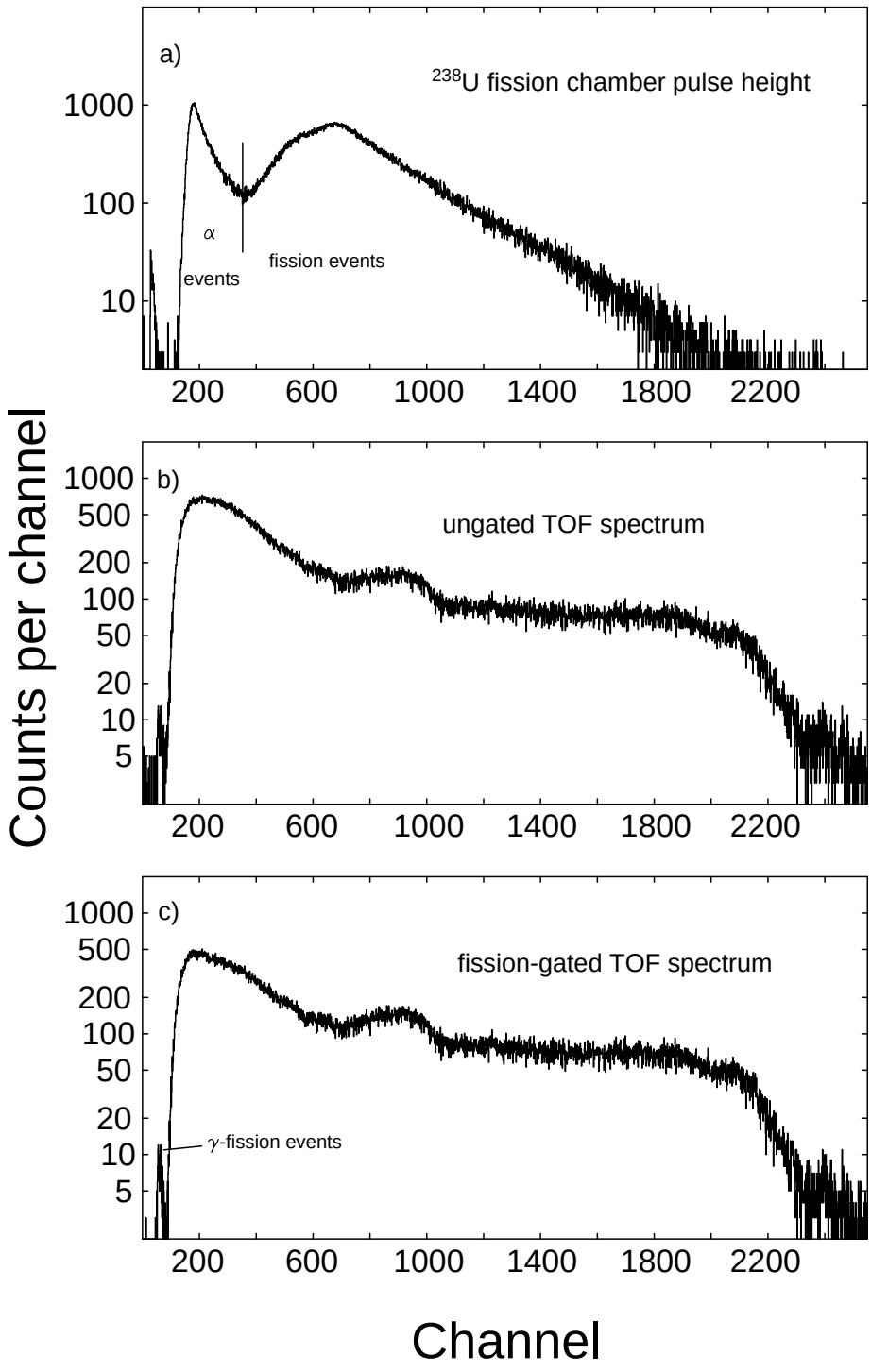

Figure 4.8: Data obtained from the ^{238}U fission foil used to determine neutron intensity at the GEANIE spectrometer. In panel (a), the pulse height spectrum is shown. The vertical line corresponds to the lower limit on the pulse-height gate for a signal to be considered a fission event. In panel (b), the raw TOF spectrum is shown, defined as the time of the events in measured relative to the proton beam burst. In panel (c) the TOF spectrum resulting from the condition imposed in panel (a) is shown.

The number of neutrons in a time bin from T^L to T^H is given by [You01]

$$N_n([T^L, T^H]) = \sum_{\tau=T^L}^{T^H} N_n(\tau) \int_0^\infty \frac{1}{\sqrt{2\pi}\sigma_\tau} \times exp(-\frac{(\tau-\tau')^2}{2\sigma_\tau^2}) d\tau', \tag{4.10}$$

where τ is the time of flight, $N_n(\tau)$ is a flux normalization parameter which is calculated from the neutron count in each TOF channel, and σ_τ is the detection timing uncertainty, determined in our experiment to be 15 ns FWHM ($\Rightarrow \sigma_\tau = 6.37$ ns) [You00]. The effect due to the finite time resolution is taken into account and assumed to be Gaussian distributed. Since the neutron spectrum is not constant, the mean energy $\bar{E}_n$ of the neutrons in the bin from time T^L to T^H is determined from

$$\bar{E}_n = \frac{\sum_{\tau=T^L}^{T^H} E_n(\tau) N_n(\tau) \int_0^\infty \frac{1}{\sqrt{2\pi}\sigma_\tau} exp(-\frac{(\tau-\tau')^2}{2\sigma_\tau^2}) d\tau'}{\sum_{\tau=T^L}^{T^H} N_n(\tau) \int_0^\infty \frac{1}{\sqrt{2\pi}\sigma_\tau} exp(-\frac{(\tau-\tau')^2}{2\sigma_\tau^2}) d\tau'}, \tag{4.11}$$

and the variance

$$\sigma_{E_n}^2 = \frac{\sum_{\tau=T^L}^{T^H} \left[E_n(\tau) - \bar{E}_n\right]^2 N_n(\tau) \int_0^\infty \frac{1}{\sqrt{2\pi}\sigma_\tau} exp\left(-\frac{(\tau-\tau')^2}{2\sigma_\tau^2}\right) d\tau'}{\sum_{\tau=T^L}^{T^H} N_n(\tau) \int_0^\infty \frac{1}{\sqrt{2\pi}\sigma_\tau} exp\left(-\frac{(\tau-\tau')^2}{2\sigma_\tau^2}\right) d\tau'}. \tag{4.12}$$

It should be noted that in the plots of excitation functions, the horizontal E_n error bars are derived from the variance and thus represent the width of the neutron energy distribution, rather than the uncertainty on the mean neutron energy for the bin.

The deadtime fractions (1−livetime) in Eq. (4.9) were calculated from the ratio of measured ADC and scaler counts. Total deadtimes of 62.0% and 58.0% were determined for the planar and coaxial sums, respectively, and deadtimes of 52.0% and 50.9% were obtained for the ^{235}U and ^{238}U fission foils. The systematic extraction of angular distributions for γ rays in GEANIE data is an exceedingly difficult task. The 20 detectors in the array occupy only 5 distinct angles, and corrections due to differences in efficiency and deadtime must be taken into account. We examined the angular distribution for $E_\gamma = 983.5$ keV (the transition between 2^+ to 0^+ states in ^{48}Ti) and there was no significant angular distribution effect in the corresponding (n, n') cross section.

4.5 Analysis of $\gamma\gamma$ matrix

A coincidence experiment can be performed by selecting γ rays in one detector and measuring time-related events in other detectors within a given time window. The coincidence information, i.e., the number of fired detectors, time signals, and γ-ray energies, is recorded in an event-by-event mode. For the GEANIE array, the measured γ-ray energy and multiplicity can be recorded at the same time. A $\gamma\gamma$ (E_γ-E_γ) matrix is created by sorting the γ-ray energy from one detector on one axis and the correlated detector on another axis. Multiplicity two-and-higher coincidences from both the planar and coaxial detectors were sorted into a $4k\times4k$ $\gamma\gamma$ matrix. Prompt coincidence events were considerably fewer compared to single-fold data, and to maximize statistics the data from both planar and coaxial detectors were combined after converting them to the same energy range. A TOF gate corresponding to neutron energies between 1 to 12 MeV was imposed to minimize background from other reactions. To build the coincidence matrix, $\gamma\gamma$ resolving-time windows of 30 ns, 35 ns, and 40 ns were set for planar-planar, planar-coaxial, and coaxial-coaxial detector coincidences, respectively. The $\gamma\gamma$ matrix is used to establish the coincidence relations of transitions in a level scheme. Coincidences between γ rays provide an additional tag to eliminate extraneous information in the spectra. A generalized background subtraction was applied to the $\gamma\gamma$ matrix that was processed using the code ESCL8R [Rad95]. Taking a slice at an energy (on a narrow range of channels) from one axis of a $\gamma\gamma$ matrix and projecting the spectrum onto the other axis is equivalent to measuring a coincidence spectrum of the selected γ ray, i.e., setting a gate. A decay scheme is established by first analysing the coincidence relationships of different γ rays. A schematic $\gamma\gamma$ coincidence relationship is shown in Fig. 4.9. By gating on γ_1, one should see γ_2 and γ_3 in the gated spectrum since they are in a cascade with γ_1. On the other hand γ_2 or γ_3 should not appear in its counterpart gate, because they are not time-related. To place a γ ray in a decay scheme, one must use the intensity pattern as a second criterion. The intensity within a band should decrease as spin increases since at higher spins or excitation energies the level density becomes large and

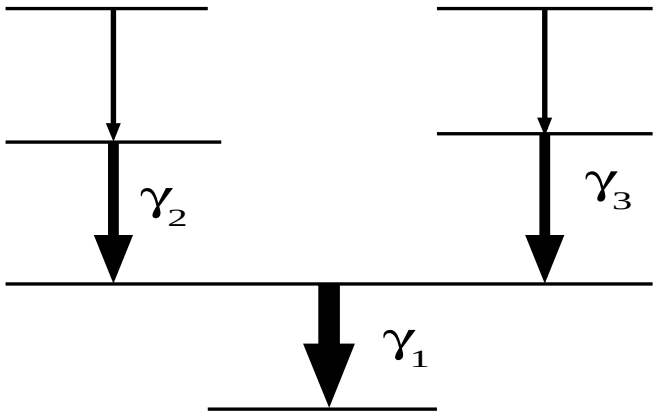

Figure 4.9: Schematic diagram of $\gamma\gamma$ coincidence relationship; $\gamma_1 - \gamma_2$, $\gamma_1 - \gamma_3$ are time-related, but $\gamma_2 - \gamma_3$ are not.

the feeding of intensity spreads over many levels, resulting in only those relatively strong branches being observed. In a gated spectrum, any transition feeding into the gated γ-ray level should follow the above intensity rule, while the decay-out intensity should roughly be a constant for any succeeding transitions. These rules were followed in the establishment of the level scheme of ^{48}Ti.

Fig. 4.10 displays portions of selected coincidence spectra, showing some of the stronger transitions in the ^{48}Ti(n,n$'\gamma\gamma$)^{48}Ti reaction. The resulting partial level scheme is shown in Fig. 4.11. In total, over 60 γ rays were identified with existing transitions in the NUDAT [nud] database, and placed in the level scheme.

Due to the low statistics, γ rays with energy above 3.0 MeV are constructed from single-fold events in Fig. 4.11. Examples of the $\gamma\gamma$ coincidence technique are shown in Fig. 4.10. In the upper panel, the coincidence spectrum gated on the 175-keV transition between the 3508.5-keV and 3333.2-keV levels gives the transitions which belong to the same

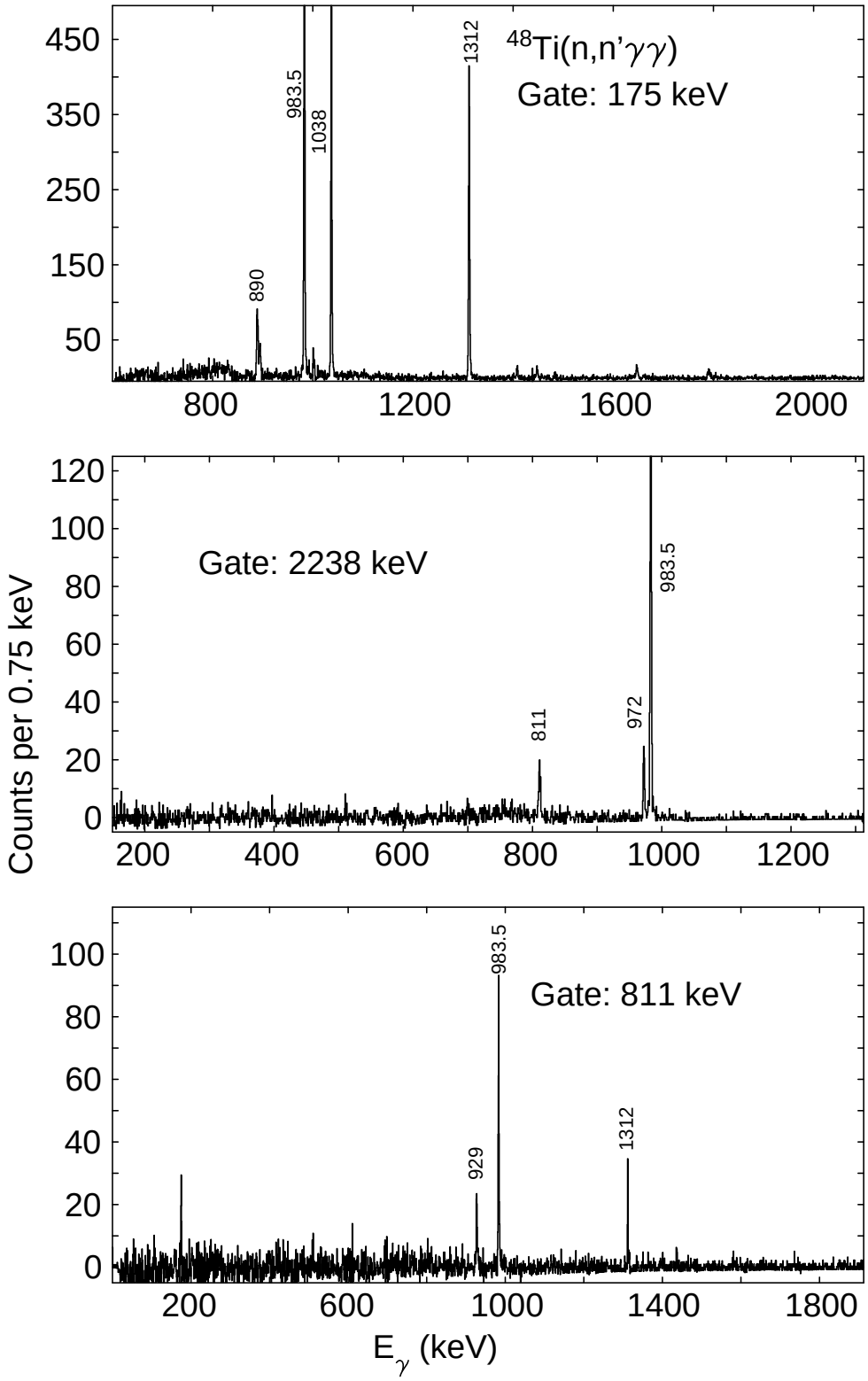

Figure 4.10: Examples of $\gamma\gamma$ coincidence spectra used to place γ's following the ^{48}Ti(n,n$'$) reaction.

cascade as the 175-keV transition. In this case, the coincident transitions are the 890-keV transition from the decay of the 4398.0-keV level to the 3508.5-keV level and subsequent 1038-keV, 1312-keV, and 983.5-keV transitions from the decay of the 3333.2-keV level to the ground state. In the middle panel, the coincidence spectrum gated on the 2238-keV transition between the 3223.9-keV and 983.5-keV levels yields the 811-keV and 972-keV transitions from decays of higher lying levels to the 3223.9-keV level, and the subsequent 983.5-keV transition from the decay of the 983.5-keV level to the ground state. Similarly in the lower panel, the coincidence spectrum gated on the 811-keV transition between the 4035.1-keV and 3223.9-keV levels gives the 929-keV, 983.5-keV, and 1312-keV transitions which can also be placed in the level scheme. The intensities in the level schemes (the thickness of the arrows) are based on the GEANIE data. In general, these intensities argee with NUDAT. The spin and parity assignments are from the NUDAT [nud].

4.6 Threshold analysis

The threshold neutron energy for observing a given γ ray can sometimes help confirm or reject the placement of that transition in the corresponding level scheme. In principle, for a micropulse spacing of 1.8 μs, it should be possible to extract the excitation function for a γ down to $E_n \approx 620$ keV within one micropulse. In practice, the data from slower neutrons are contaminated by the γ flash from the next micropulse, and excitation functions can realistically be extracted for $E_n \geq 1$ MeV.

Also it is important to know the reaction Q value and reaction threshold excitation energy to identify a given γ ray. To calculate the reaction Q value and threshold energies for n + ^{48}Ti reactions, we used the computer code Qtool [qto]. This code computes reaction Q values and thresholds using experimental and theoretical nuclear masses. Qtool is implemented on a webpage, prepares a table of Q values and reaction thresholds for channels open up to desired energy. The calculation is based on the Audi-Wapstra experimental masses [Aud95] when available, otherwise on the FRDM (1992) mass model. In Table 4.5,

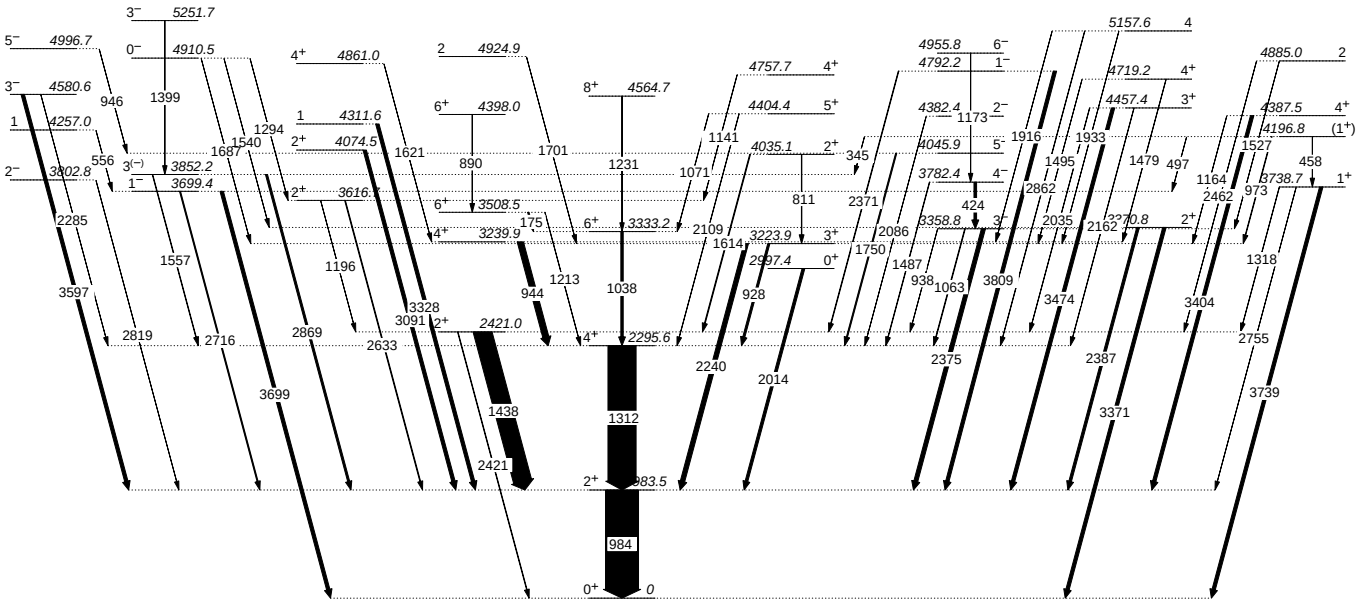

Figure 4.11: Partial level scheme for ^{48}Ti determined from the inelastic channel.

some example of the reaction Q values and thresholds up to incident neutron energy 40 MeV.

Table 4.5: Reaction Q values and thresholds: Open channels for the n + ^{48}Ti reaction at 40 MeV.

Reaction Products	Q value (MeV)	Threshold (MeV)
^{49}Ti + γ	8.12243	0.0000
^{48}Ti + n	0.0000	0.0000
^{45}Ca + α	-2.02807	2.07074
^{48}Sc + p	-3.21186	3.27942
^{44}Ca + n + α	-9.44290	9.64155
^{47}Sc + n + p	-11.44443	11.68518
^{47}Ti + 2n	-11.62669	11.87127
^{41}Ar + 2α	-12.19834	12.45495
^{47}Ca + 2p	-12.65402	12.92022
^{46}Ti + 3n	-20.50447	20.93582
^{43}Ca + 2n + α	-20.57496	21.00779
^{43}K + n + p + α	-21.60801	22.06257
^{46}Sc + 2n + p	-22.08883	22.55351
^{42}Ca + 3n + α	-28.50802	29.10774
^{45}Ca + 2n + 2p	-30.32397	30.96189
^{45}Sc + 3n + p	-30.84953	31.49850
^{45}Ti + 4n	-33.69433	34.40315

4.7 Iron line analysis

As a validation of the experiment and the analysis technique, the partial cross section of the $2_1^+ \rightarrow 0_1^+$ transition in ^{56}Fe has been extracted from a series of runs with the ^{48}Ti sample sandwiched between 5-mil ^{nat}Fe foils. The partial γ-ray cross section for the 847-keV transition in n+^{56}Fe has been extracted from both planar and coaxial data, and is plotted in Figs. 4.12 and 4.13, respectively. These data are compared to the cross section of 705 $\pm$ 56 mb at E_n = 14.5 MeV, evaluated by Nelson *et al.* [Nel04].

4.8 Doppler effects

When a nuclear reaction occurs, the recoiling excited nucleus is traveling through a surrounding medium and slows down. ^{48}Ti is a light nucleus and therefore Doppler effects should be investigated for the n+^{48}Ti reaction. The Doppler-shifted energy of a γ ray detected at angle θ with respect to the recoil direction of the nucleus emitting it is given by

$$E_\gamma(\theta) = E_\gamma^0 \left[1 + F(\tau)\beta_0 cos\theta\right], \tag{4.13}$$

where E_γ^0 is the γ-ray energy in the rest frame of the recoiling nucleus, the attenuation factor F(τ) varies between 0 and 1 and is a function of the level lifetime τ, β_0 is the initial velocity of the recoiling nucleus, relative to the speed of light, in the lab frame. For reactions in an extended sample, the Doppler shifts must be averaged over different scattering angles. For low-energy (n,n$'\gamma$) reactions and assuming that F(τ) does not depend on the recoil velocity, β_0 in Eq. (4.13) must be replaced by β_{CM}, the velocity of the center of mass in the lab frame [Bel96]

$$\beta_{CM} = 0.04635 \left(\frac{A_n}{A_n + A_T}\right) \sqrt{\frac{E_n}{A_n}}, \tag{4.14}$$

where A_n is the neutron mass in atomic mass units (1.00866497 u), A_T is the target mass in atomic units (47.9479463 u, for ^{48}Ti), and E_n is the incident neutron energy in MeV. Thus, for example, 2-MeV neutrons incident on ^{48}Ti nuclei will result in $\beta_{CM} = 0.00165$. A

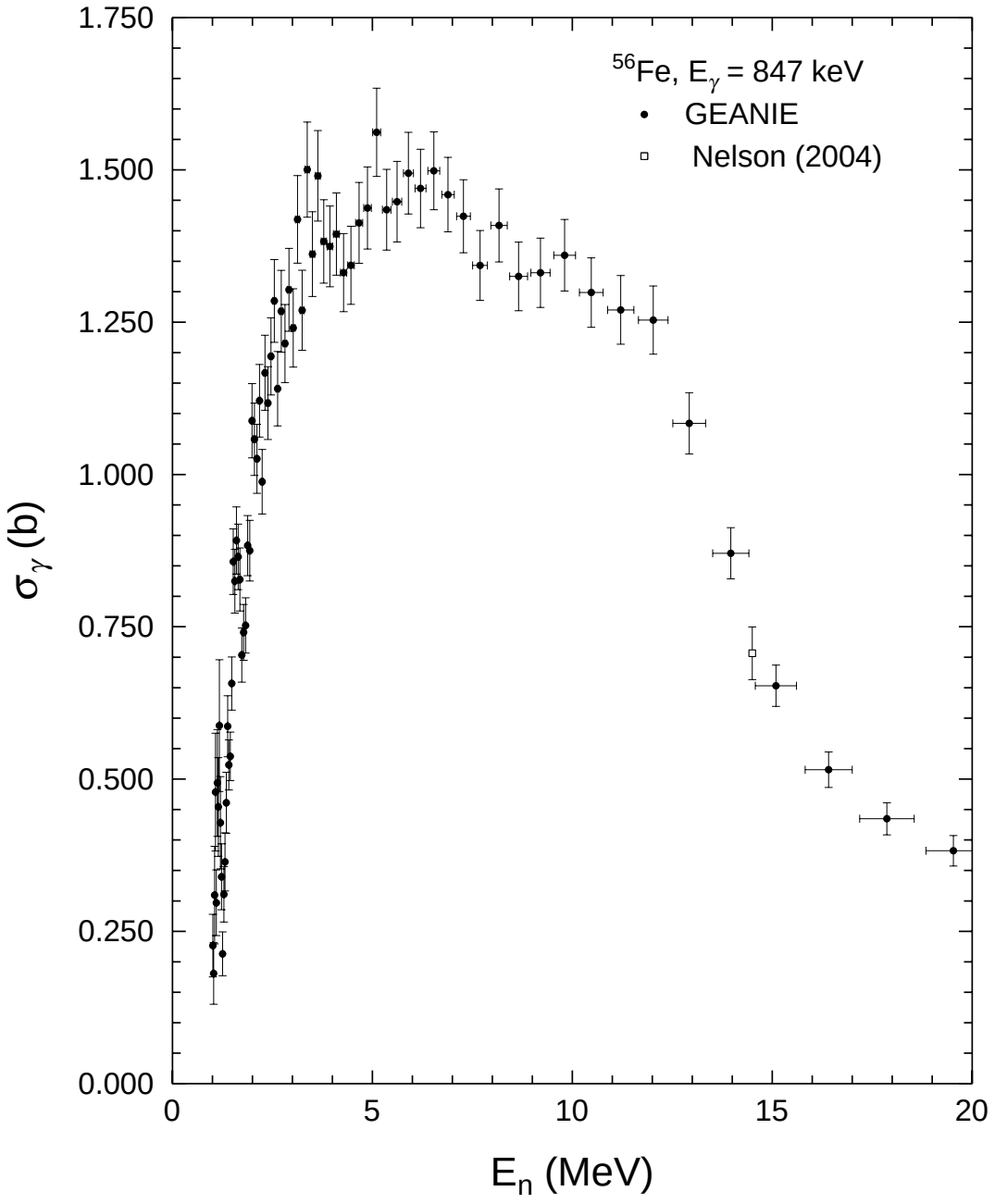

Figure 4.12: Partial γ-ray cross section for the ^{56}Fe 847-keV transition measured in the planar detectors, and compared with an evaluation at E_n=14.5 MeV by Nelson [Nel04].

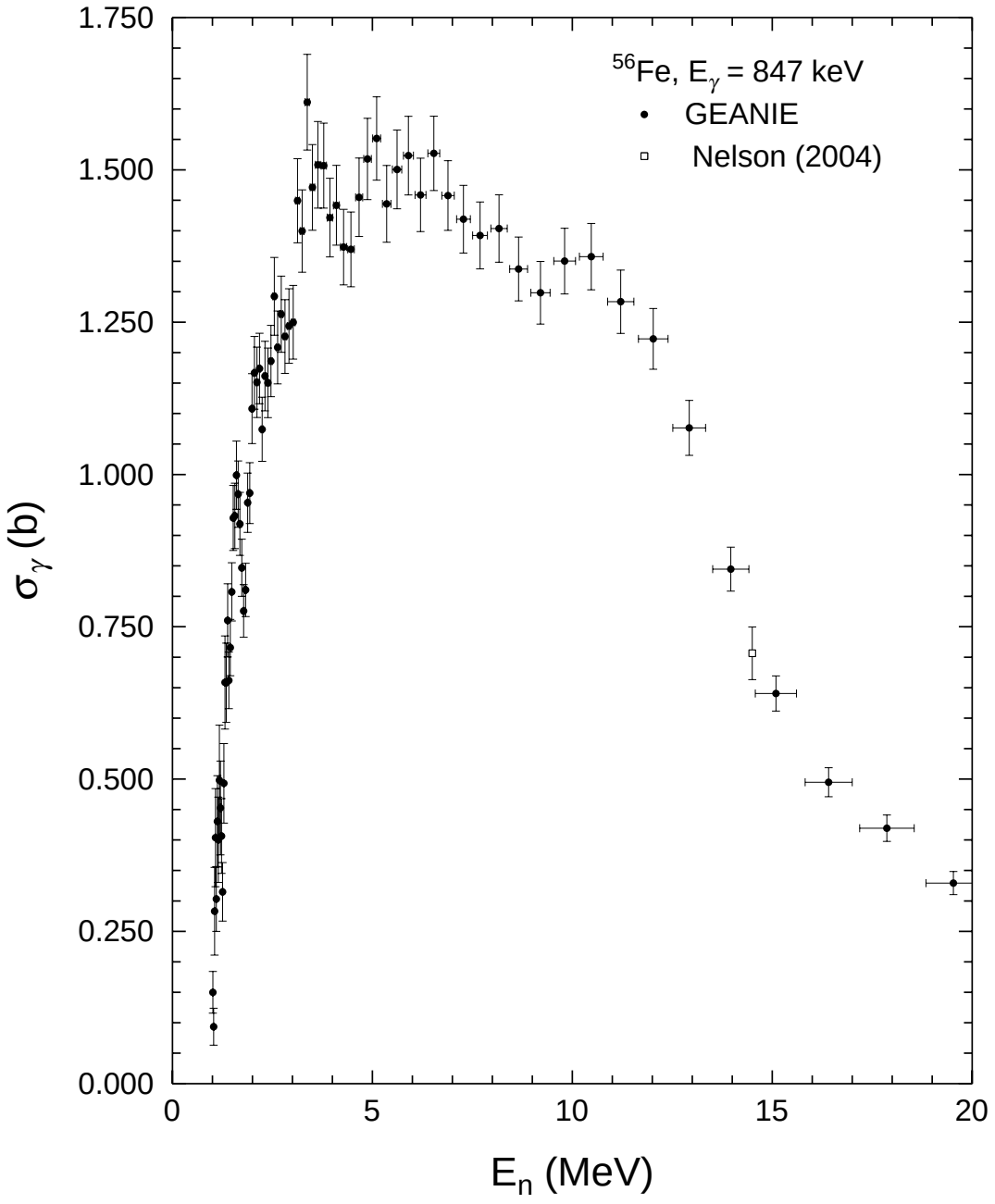

Figure 4.13: Partial γ-ray cross section for the ^{56}Fe 847-keV transition measured in coaxial detectors, and compared with an evaluation at E_n=14.5 MeV by Nelson [Nel04].

0.983-MeV γ ray produced in this reaction will experience a Doppler shift of at most 1.6 keV (assuming $F(\tau) = 1$ and $\theta = 180°$), which is less than the observed width of 2.2 keV for γ-ray peaks at this energy. For higher-energy neutrons, the situation is more complicated. In order to investigate the potential effects of Doppler shifts in the present data set, attenuation factors $F(\tau)$ have been extracted by fitting individual-detector γ-ray spectra, corresponding to the range $E_n = 1-20$ MeV. Attenuation factors have been inferred for many transitions in the ^{48}Ti$(n, n'\gamma)$ channel by fitting γ-ray energies with Eq. (4.13). There are no general reliable trends that can be extracted.

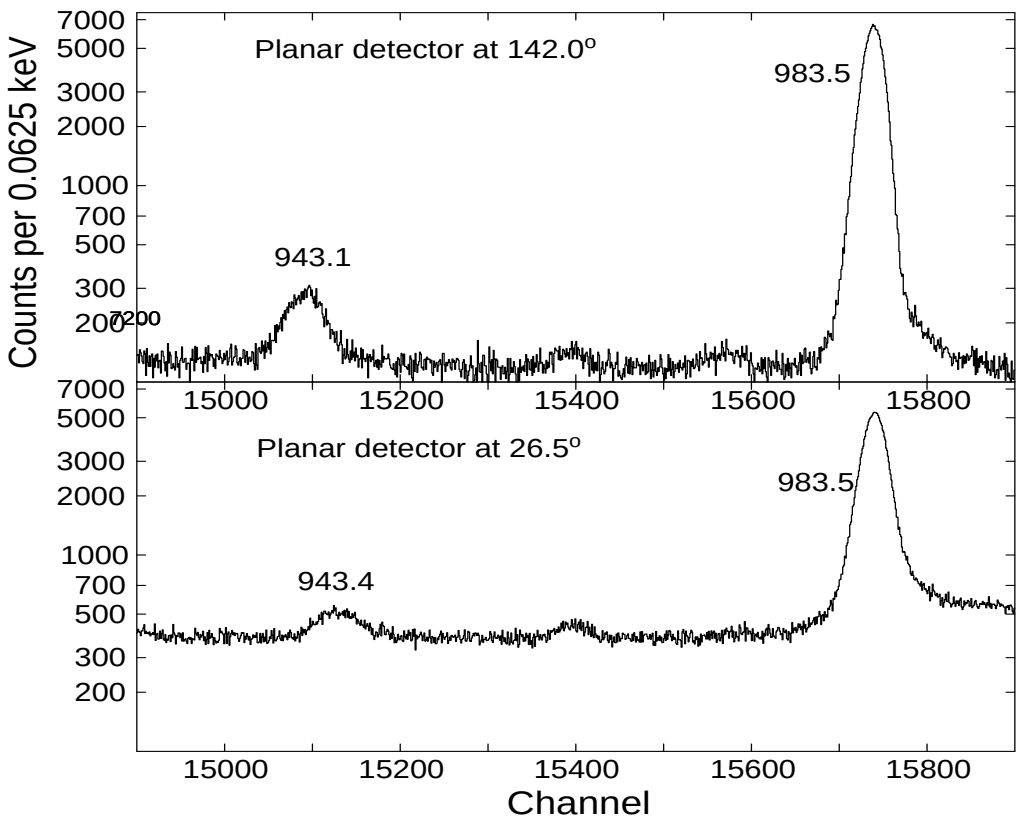

Figure 4.14: Part of the individual planar detector spectrum. These spectra are aligned using $E_\gamma = 803.06$ keV transition from ^{206}Pb, for which we assumed no Doppler shift.

In Fig. 4.14, part of the spectra from planar detectors at the most forward angle

26.5° and at the most backward angle 142.0° are shown. A γ ray of $E_\gamma = 983.5$ keV from the 0.983 MeV level, with a level lifetime of 4.27 ps has no Doppler shift, but a γ ray of $E_\gamma = 944.0$ keV from the 3.239 MeV level (with a level lifetime of 46 fs), a Doppler shift of ≈ 0.3 keV is deduced from Fig. 4.14. Reliable Doppler shifts for individual transitions are very difficult to extract from these data because (i) the spectra are very complex, (ii) only 4 distinct detector angles are available for the planar data, and (iii) the statistics in individual-detector spectra are limited.

The GEANIE data seem to suggest that the attenuation factors for the present experiment are very weak in general, and therefore it is unlikely that Doppler shifts will significantly affect the γ-ray analysis.

Chapter 5

Theoretical Model Calculations

5.1 Hauser-Feshbach statistical model

A traditional theoretical approach to compound nuclear reactions is the statistical, Hauser-Feshbach model. This model is valid only for high level densities in the compound nucleus, allowing one to use energy-averaged transmission coefficients T, which describe absorption via an imaginary term in the (optical) nucleon-nucleus potential. Theoretical details are given in Chapter 2. The principal assumption made in the calculation of cross sections and emission spectra from complex reaction processes is that the reaction proceeds in a series of binary reaction stages; at each stage particle and γ-ray emission are calculated. The energetics of this process are illustrated schematically in Fig. 5.1. An initial compound nucleus is formed with excitation energy U, spin J, and parity Π. This process and all others occurring in the calculation are subject to constraints imposed by the following energy, spin, and parity conservation laws:

$$\begin{aligned} \varepsilon + B_a &= \varepsilon' + E' + B_{a'} = U \\ i + I + l &= i' + I' + l' = J \\ pP(-1)^l &= p'P'(-1)^{l'} = \Pi \end{aligned} \tag{5.1}$$

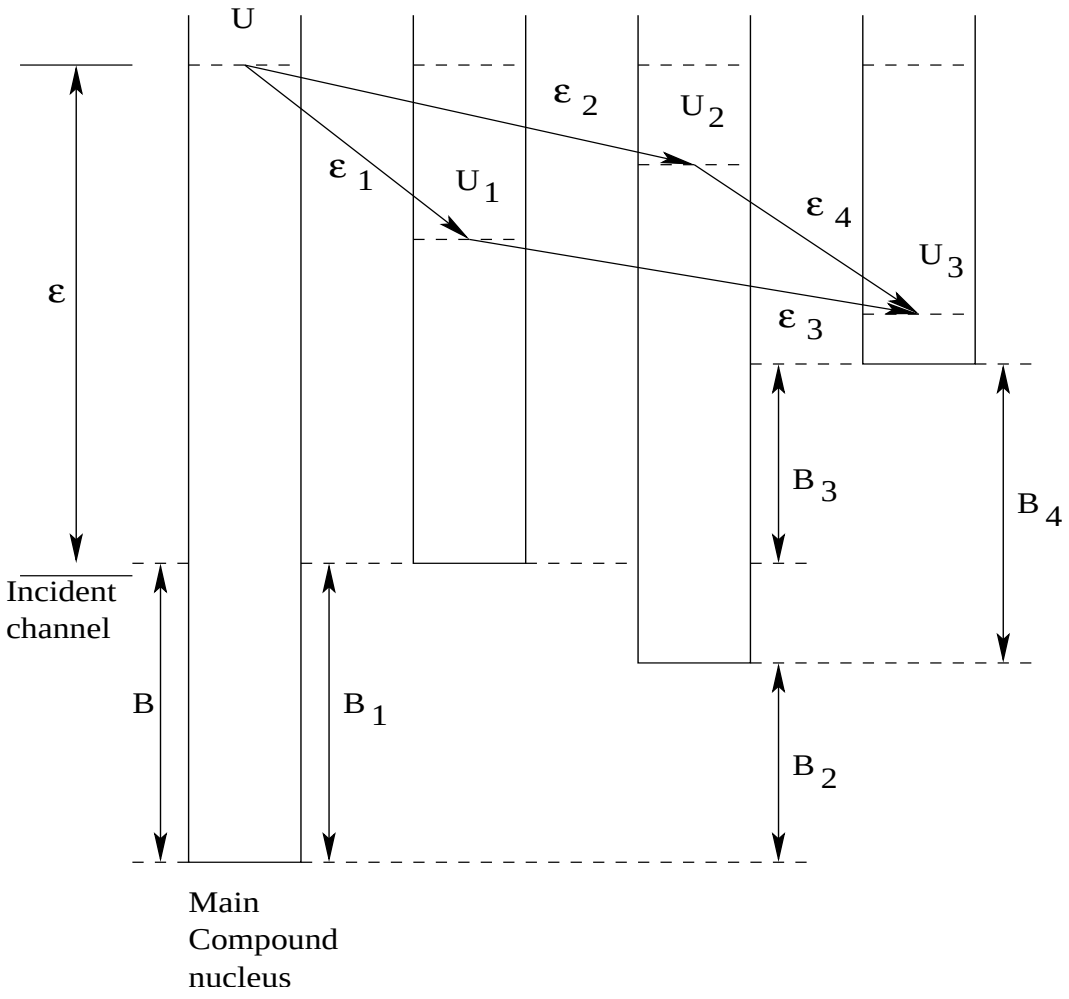

Figure 5.1: Schematic illustration of the energetics of reaction sequences.

where ε and ε' are center of mass energies of incoming and outgoing particles a and a', B_a and B'_a are binding energies of the particles relative to the compound system, i, I, p, and P are spins and parities associated with target or residual nucleus, and l is the orbital angular momentum. The primed quantities indicate the outgoing channel. For the reaction I (in state μ) $+s \rightarrow k + L$ (in state ν), with $I^\mu + s$ interacting with center-of-mass energy E (in MeV), the average cross section is given by

$$\sigma_{sk}^{\mu\nu}(E) = \frac{\pi \lambda\!\!\!^{-2}}{g_I^\mu g_s} \sum_{J,\pi} g_J \frac{T_s^\mu(J^\pi) T_k^\nu(J^\pi)}{T_{tot}(J^\pi)} W(J^\pi), \tag{5.2}$$

where the summation extends over all compound nuclear spins and parities J^π, μ and ν label the states in the target and product (= 0 for the ground state, 1 for the 1st excited state, etc.). The cross section has units of area, described by $\pi \lambda\!\!\!^{-2} = 0.6566(\hat{A}_s E)^{-1}$ barns, with $\hat{A}_s = (A_I A_s)/(A_I + A_s)$ the reduced mass in atomic mass units and E the center-of-mass energy in units of MeV. $\lambda\!\!\!^{-}$ is the wavelength, which is related to the wave number k in the target plus incident particle channel by $\lambda\!\!\!^{-} = 1/k$. The statistical weights are given by $g_y^x = (2J_y^x + 1)$. Items without superscripts refer to the compound nucleus. The coefficients W(J^π) are the width fluctuation corrections.

5.2 The STAPRE reaction code

The statistical model code STAPRE (STAatistical−PREequilibrium) has been used to model the cross sections [Uhl76] for $E_n = 1-20$ MeV. The physical models that have been included are discussed below. The version of the code used is STAPRE-H95 [Avr95]. Several modifications have been made, primarily to the level density routines.

5.2.1 Transmission coefficients

The transmission coefficients in the numerator of Eq. (5.2) are given by $T_s^\mu(J^\pi)$, which equals the total transmission function for forming the state J^π in the compound nucleus $I^\mu + s$ at energy E_s^μ. Similarly, $T_k^\nu(J^\pi)$ is the same as $T_s^\mu(J^\pi)$ but for the pair

$L^\nu + k$ at energy E_k^ν. Implicit in these definitions is a sum over all possible partial waves and channel spins, i.e.,

$$T_s^\mu(J^\pi) = \sum_{l,s} T_s^\mu(J^\pi, l, j), \tag{5.3}$$

where l is any partial wave number (orbital angular momentum) that can couple the state μ to the compound nuclear state having spin and parity J^π subject to quantum mechanical selection rules, and j is the vector sum of the spins J_I^μ and J_s. Hence j takes on all integer (or half-integer) numbers from $|J_I^\mu - J_s|$ to $J_I^\mu + J_s$.

T_{tot} represents the sum of transmission coefficients over all possible decay channels (i.e., for all particles and photons). The cross section for the formation of species L, regardless of its state ν, is obtained by summing Eq. (5.2) over all bound states ν of L for which the reaction is energetically allowed.

When evaluating these sums, if the energies of interest exceed the highest discrete excited state for which energy, spin, and parity are explicitly known, a nuclear level density formula must be employed. Specifically, the definitions for $T_j(J^\pi)$, $T_k(J^\pi)$, and $T_{tot}(J^\pi)$ must be modified, for example:

$$T_k(J^\pi) = \sum_{\nu=0}^{\omega} T_k^\nu(J^\pi) + \int_{\xi_L^\omega}^{\xi_L^{max}} \int_{J^\nu \pi^\nu} T_k^\nu(\xi_L^\nu, J^\pi)\rho(\xi_L^\nu, J^\nu, \pi^\nu) d\xi_L^\nu d\pi^\nu dJ^\nu,$$

where for the nucleus L, ξ_L^ω is the energy of the highest excited state, ω, of known energy, spin, and parity. $\xi_L^{max} = E_k^0 = E_s^0 + Q_{sk}$ is the maximum excitation energy available, while $\rho(\xi_L^\nu, J^\nu, \pi^\nu)$ is the density of states per unit energy and for spin and parity J^ν and π^ν at the excitation energy ξ_L^ν. The above integral approximates a summation and is subject to the same quantum mechanical restrictions implied in the definition of the transmission function.

The optical model

For the calculation of the particle (neutron and proton) transmission coefficients $T_k^\nu(\xi_L^\nu, J^\pi)$, the optical model developed by Koning and Delaroche [Kon03] has been used. Although the Koning-Delaroche parameters are tuned to fit data for many different species (see Tables 6 and 7 in Ref. [Kon03]), the use of the global nucleon-nucleon Optical Model Potential (OMP) gives a very satisfactory fit to measured total cross section data for neutrons and protons in the range of interest. The adopted potential depth parameters and Fermi energies for the neutron and proton global OMP are defined as in Section 5.2, Tables 10 and 11 of Ref. [Kon03]. The particle transmission coefficients were generated by the optical model code ECIS-95 [Ray96]. The coupled-channel calculations were performed in a spherical optical model mode.

Level densities

For this calculation, a modified version of the level density formulation of [Rau97] has been adopted. The level density is described by two different functions above and below a matching energy E_x, which are matched in magnitude and slope at E_x, as in Ref. [Gil65].

Above the matching energy, the back-shifted Fermi gas model

$$\rho(E) = \frac{exp(2\sqrt{aU})}{12\sqrt{2}a^{1/4}U^{5/4}\sigma}, \tag{5.4}$$

is used, where $U = E - \Delta$. Δ is the so called "pairing energy" or backshift parameter, and σ is the spin cut-off parameter. Rather than using a constant pairing energy or one with a fixed dependence on mass number, the pairing energy was determined from the nuclear binding energies, as in Ref. [Rau97]:

$$\begin{aligned} \Delta(Z,N) &= \Delta_p(Z,N) + \Delta_n(Z,N) \\ \Delta_p(Z,N) &= E^G(Z,N) \\ &- \frac{1}{2}E^G(Z-1,N) \\ &- \frac{1}{2}E^G(Z+1,N) \end{aligned} \tag{5.5}$$

$$\begin{aligned}\Delta_n(Z,N) &= E^G(Z,N) \\ &- \frac{1}{2}E^G(Z,N-1) \\ &- \frac{1}{2}E^G(Z,N+1).\end{aligned}$$

For odd N or Z, the pairing energies Δ_n or Δ_p are set to zero, respectively. The level density parameter a was taken to be

$$\begin{aligned}a(U,Z,N) &= \tilde{a}(A)\left(1+\delta W(Z,N)\frac{f(U)}{U}\right) \\ f(U) &= 1-\exp(-\gamma U) \\ \tilde{a} &= 0.1337A - 0.06571A^{2/3},\end{aligned} \tag{5.6}$$

with $\gamma = 0.04884$, and the $\delta W(Z,N)$ parameters are shell corrections given in Ref. [Mol95]. Finally, the spin-cutoff parameter σ in Eq. (5.4) is defined by

$$\sigma^2 = \lambda\sqrt{aU}A^{2/3}, \tag{5.7}$$

where $\lambda = 0.146$. This formulation of the level density has been shown to replicate known experimental resonance spacings at the neutron binding energy reasonably well.

Eq. (5.4) diverges as E approaches Δ. Thus, below the matching energy approximately given by $E_x = 2.5 + 150/A$, a constant temperature formula for the level density

$$\rho(E) = \frac{1}{T}\exp\left[\frac{E-E_0}{T}\right]\frac{1}{\sqrt{2\pi}\sigma}, \tag{5.8}$$

is used, where σ is defined as before, except that it is held constant below E_x. The parameters E_0 and T are uniquely determined by the condition that the two level density formulae match in magnitude and slope at E_x. Generally, this constant temperature formulation provides a reasonable fit to low-lying levels.

The level density is related to the state density by

$$\begin{aligned}\rho(E,J) &= \rho(E)\,f(E,J) \\ f(E,J) &= \frac{2J+1}{2\sigma^2}exp\left(\frac{-(J+1/2)^2}{2\sigma^2}\right),\end{aligned} \tag{5.9}$$

where J is the spin of the compound nucleus.

Photon transmission coefficients

For the calculation of the γ-ray transmission coefficients, a simple model where the transmission coefficient depends only on the multi-pole type (XL = E1, M1, E2, etc ...) and the transition energy ε is used. The transmission coefficient is related to the γ-ray strength functions $f^{\gamma}_{XL}(\varepsilon)$ by

$$T^{\gamma}_{XL}(\varepsilon) = 2\pi\varepsilon^{2L+1} f^{\gamma}_{XL}(\varepsilon). \tag{5.10}$$

The energy dependence of the strength function was determined using the GDR model with Lorentzian shapes. The transmission coefficients were then normalized by fitting the average total s-wave radiation width at the neutron binding energy [Uhl76].

Since the total s-wave radiation width at the neutron binding energy is generally measured only for stable isotopes plus a neutron, this value was estimated from the systematics for the unstable nuclei. The systematic values are determined by a least squares linear fit to experimental data, with separate systematics developed for even-Z even-N, even-Z odd-N, odd-Z even-N, and odd-Z odd-N compound nuclei. Since in the case of odd-Z even-N nuclei, no experimental s-wave data was available in the region of interest, the odd-Z odd-N systematic for all odd-Z nuclei was adopted. The systematics for the total s-wave radiation width used were

$$\begin{aligned} \texttt{Even Z, Even N:} \quad & 64.4N - 748 \\ \texttt{Even Z, Odd N:} \quad & 109N - 1410 \\ \texttt{Odd Z:} \quad & 165N - 3290 \end{aligned} \tag{5.11}$$

The experimental values were used whenever the measured average s-wave radiation width was available.

Nuclear structure data

For nuclear masses the experimental mass excess values of Ref. [Mol95] were adopted. Spin and parity assignments are from the Evaluated Nuclear Structure Data File [ens].

The nuclear structure data needed to model the γ-ray cascade in this study were adopted from the file BUDAPEST.DAT [rip98], with an additional evaluation performed by R. Bauer [Bau02]. Partial level schemes used for STAPRE calculations are shown in Figs. 5.2, 5.3, 5.4, and 5.5.

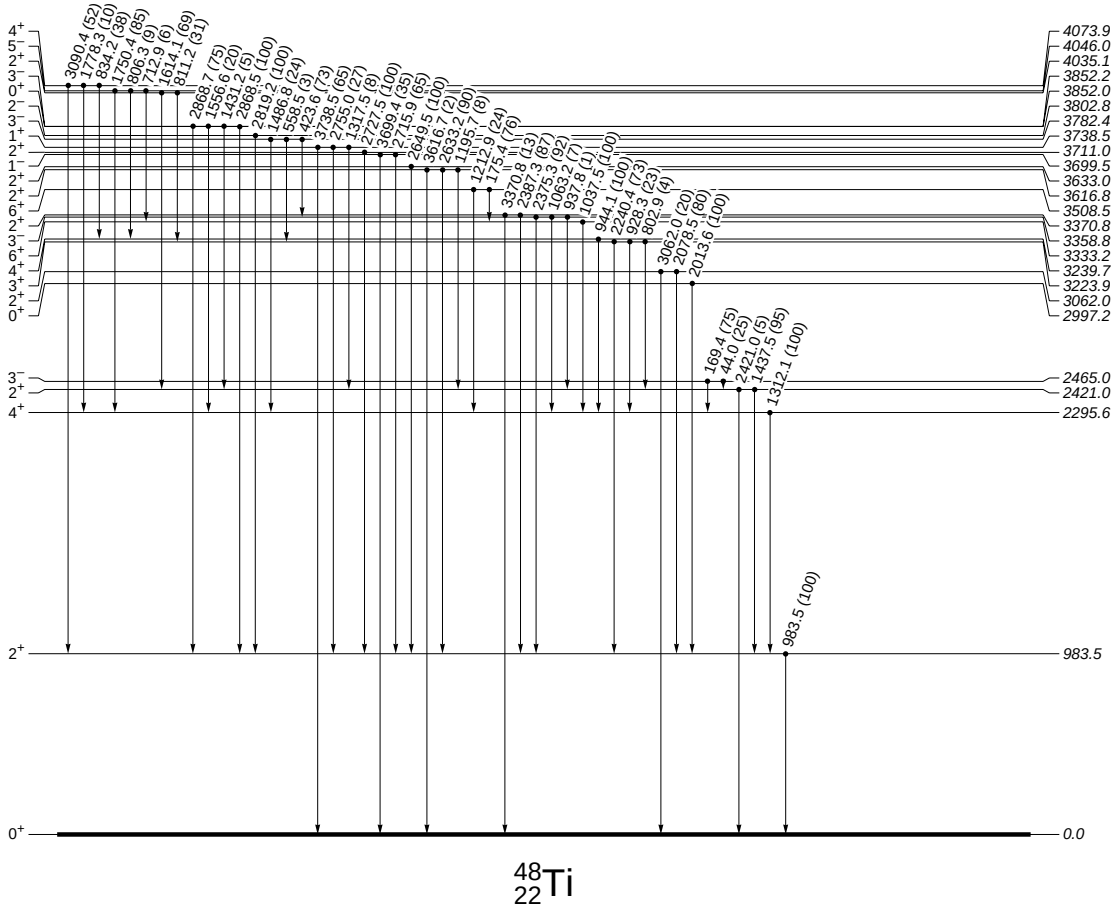

Figure 5.2: Adopted level scheme of ^{48}Ti for the STAPRE calculation.

5.2.2 Width fluctuation corrections

In addition to the ingredients required for Eq. (5.2), width fluctuation corrections (WFC) are employed as well. The correlation factors are defined with which all partial channels of incoming particle j and outgoing particle k, passing through an excited state (E, J, π), have to be multiplied. The major effect is to enhance the elastic channel and

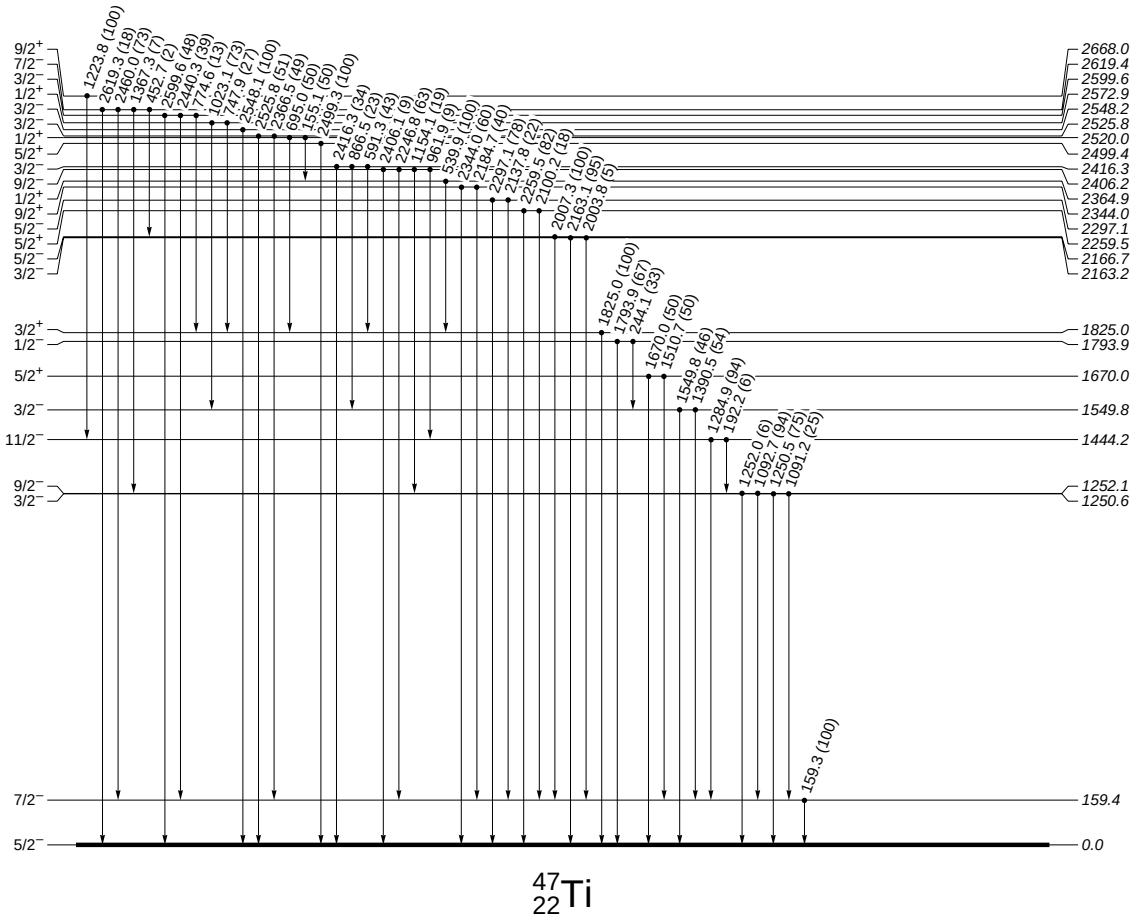

Figure 5.3: Adopted level scheme of ^{47}Ti for the STAPRE calculation.

accordingly decrease the other open channels. They are most often observed at or near channel opening energies when e.g., (p,γ) and (p,n) channels compete, and the weaker (p,γ) channel is enhanced. Above a few MeV excitation energy, when many competing channels are open, WFC's can be neglected.

The exact expression for the WFC, obtained with the Gaussian orthogonal ensemble (GOE) approach, requires the evaluation of a triple integral and to date has been considered much too costly to apply in nuclear cross section calculations. Several approximations have been developed; the most popular ones are the Moldauer model [Mol76], and the HRTW model [Hof75]. The Moldauer model of the WFC has been adapted in this case. For a detailed description of the full (GOE) treatment and a comparison with the Moldauer and

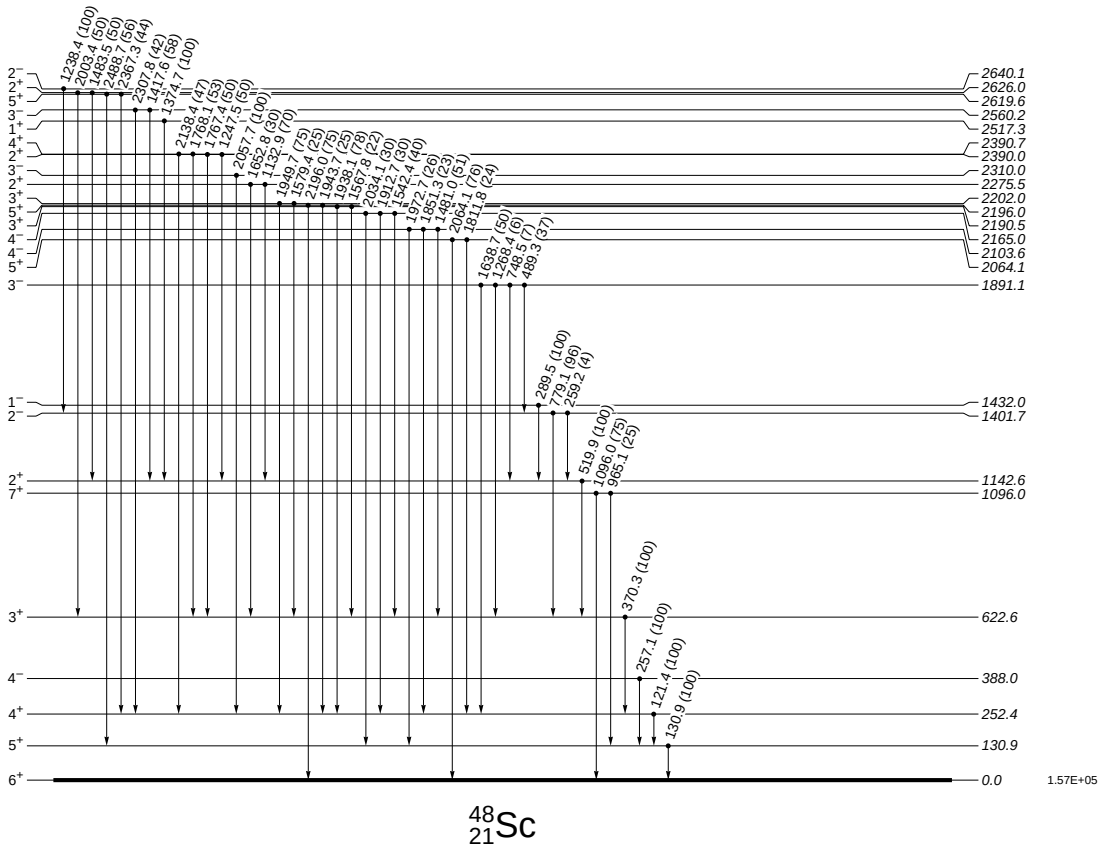

Figure 5.4: Adopted level scheme of ^{48}Sc for the STAPRE calculation.

HRTW approximation models mentioned above, see Chapter 2.

5.2.3 Preequilibrium processes

For excitation energies starting around 10 MeV, preequilibrium processes become important in (n,x) reactions. The preequilibrium cross section is subtracted from the total cross section of the first compound nucleus, and is usually unimportant for subsequent compound nuclei. Here we describe equilibration of the compound nuclear system in terms of a simple exciton model. In the preequilibrium stage of the reaction, particle or photon emission is assumed to be the only decay mode. For the equilibration portion of the first chance particle or photon, the Hauser-Feshbach formula Eq. (5.2) is applied. All subsequent (higher chance) processes are treated as sequential evaporation steps.

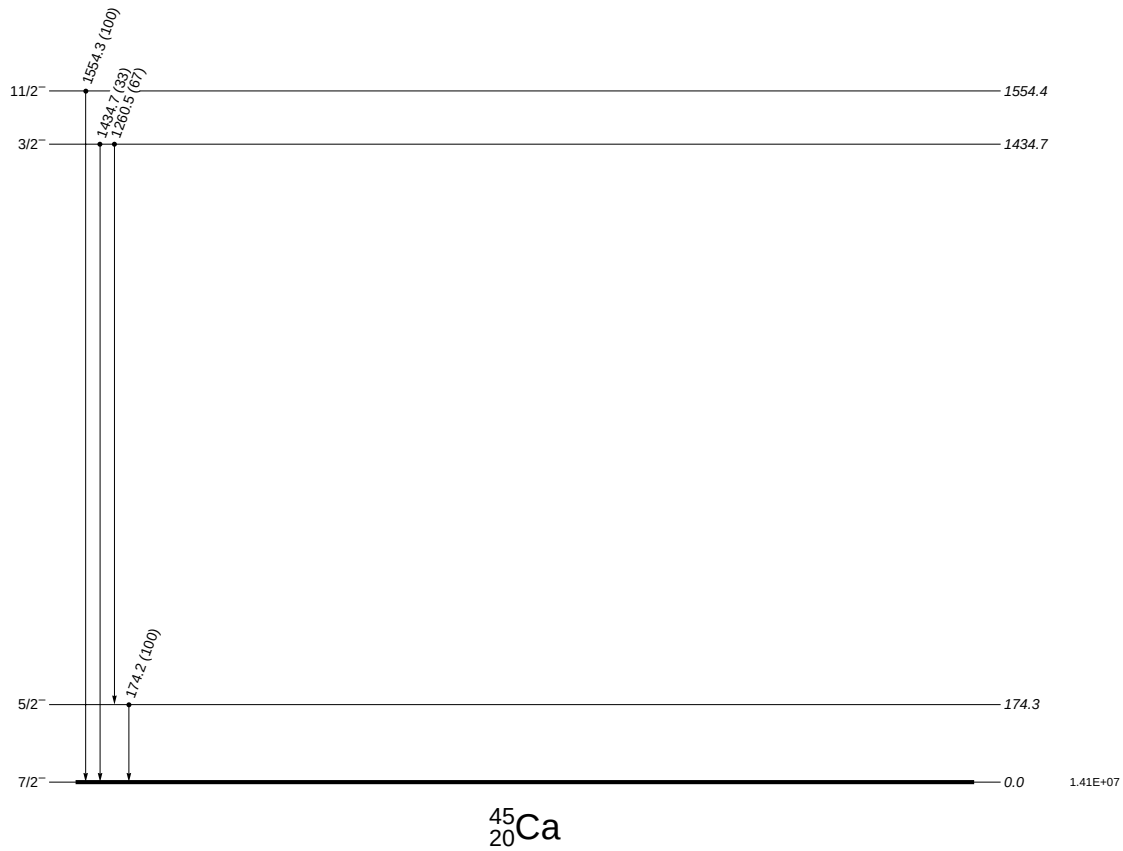

Figure 5.5: Adopted level scheme of ^{45}Ca for the STAPRE calculation.

A simple exciton model with an initial 2-particle 1-hole configuration is adapted. Average rates for internal transitions are related by the formulae of Williams [Wil70], corrected for the Pauli principle by Cline [Cli72], to the absolute square of the average effective matrix element $|M|$ of the residual interactions according to Eq. (7) of Ref. [Uhl76]. The dependence of $|M|^2$ on mass number and excitation energy is

$$|M|^2 = \langle FM \rangle A^{-3} E^{-1}. \tag{5.12}$$

A value of $\langle FM \rangle = 100$ provides reasonable agreement with the experimental cross section data in this region. This value for $\langle FM \rangle$ was applied in calculating the preequilibrium contribution to all cross sections in this study.

5.3 The GNASH reaction code

Cross sections for ^{48}Ti + n reaction were calculated using the statistical Hauser-Feshbach reaction code GNASH. A version of the GNASH code used for calculations was GN9CP0.MK dated February 1999 [You99]. GNASH implements Hauser-Feshbach theory in an open-ended sequence of reaction chains limited in number only by the memory and speed of the computer being utilized. Up to 6 types of radiation can be emitted from each compound system, so that a maximum of 60 reaction paths can be handled in a single calculation. The general method of calculation involves assuming that the reaction proceeds in a series of sequential two-body breakup processes. At each stage in the reaction, γ-ray and particle emission can occur and are computed using the Hauser-Feshbach theory which conserves angular momentum and parity. Width fluctuation and preequilibrium corrections including surface effects can be applied to the decay channels of the initial compound nucleus. Three model choices are available for continuum level densities and for γ-ray strength functions. The code has been used for calculations at energies as low as 0.1 keV and as high as 200 MeV. The models utilized are expected to be most applicable for energy range 1 keV to 150 MeV. Calculations are performed for ^{48}Ti + n reaction for neutron energies between 1 MeV to 120 MeV.

5.3.1 Transmission coefficients

All particle transmission coefficients are introduced into GNASH from an external input file that is obtained from either spherical or coupled-channel optical model calculations. Transmission coefficients depend on the orbital angular momentum and the total angular momentum. For calculations with incident neutrons or protons on nuclei that are strongly deformed such as rare earths and actinides, the coupled-channel optical model calculations with the ECIS code are used to obtain transmission coefficients. Spherical optical model transmission coefficients for GNASH calculations are determined with the CoH code by T.Kawano [Kaw05]. The CoH code solves a Schrödinger equation for a given

optical potential, and calculates the differential elastic scattering, reaction and total cross sections, transmission coefficients, for neutron, proton, deuteron, triton, and alpha-particle projectiles. Optical model parameters are taken from global phenomenological models. For neutrons and protons the Koning and Delorache [Kon03] parameters were used. The potential of Becchitti and Greenlees [Bec71] was used for tritons and deuteron and that of Lemos [Lem76] for α particles. The level density theory of Ignatyuk [Ign75] was utilized to model the statistical properties of excited nuclei. This theory is particularly appropriate for analysis at higher energies since it includes a damping shell effects in the level density parameter for increasing excitation energies. In this model the Fermi gas parameter is assumed to be energy dependent and given by the expression as a function of excitation energy U

$$a(U) = \alpha[1 + f(U)\delta W/U], \tag{5.13}$$

where α is the asymptotic value at higher energies. Shell effects are included in the term δW, which is determined via experimental masses and complemented with theoretical masses where necessary. Additional energy dependence in $a(U)$ occurs via the term $f(U)$, which is given by

$$f(U) = 1 - exp(-\gamma U), \tag{5.14}$$

where $\gamma = 0.05$ MeV was determined by Ignatuyk et al. [Ign75].

γ-ray transmission coefficients are calculated using one of several possible forms for γ-ray strength functions. The transmission coefficients for γ-ray emission are obtained from the Eq. (5.10). For γ-ray emission, the strength functions and photon transmission coefficients are obtained from the giant-resonance model of Kopecky and Uhl [Kop89]. The GNASH utilizes the generalized Lorentzian form to calculate the γ-ray strength function:

$$f_{E1}(E_\gamma T) = K_{E1}\left[\frac{E_\gamma \Gamma(E_\gamma)}{(E_\gamma^2 - E^2)^2 + E_\gamma^2 \Gamma(E_\gamma)^2} + \frac{0.7\Gamma 4\pi^2 T^2}{E^5}\right]\sigma_0 \Gamma \tag{5.15}$$

where $\Gamma(E_\gamma)$ is an energy-dependent damping width

$$\Gamma(E_\gamma) = \Gamma\frac{E_\gamma^2 + 4\pi^2 T^2}{E^2} \tag{5.16}$$

and T is the nuclear temperature given by

$$T = \sqrt{\frac{B_n - E_\gamma}{a}} \tag{5.17}$$

and K_{E1} is obtained by normalization to $2\pi < \Gamma_{\gamma 0} > / < D_0 >$ data. The standard giant dipole resonance parameters are calculated for ^{48}Ti, $\sigma_0 = 89.6$ mb, E = 19.32 MeV and $\Gamma = 5.80$ MeV. The quantities B_n and a are the neutron binding energy and Fermi gas level density parameter. For $M1$ radiation, resonance parameters are determined by $E = 41A^{-1/3}$ and $\Gamma = 4$ MeV. The excitation energy dependence of the γ-ray emission is included through the use of generalized Lorentzian forms for the $E1$, $M1$, and $E2$ strength functions.

5.3.2 Width fluctuation corrections

Width fluctuation corrections are applied to the GNASH calculation. The Moldauer model of WFC are employed.

5.3.3 Preequilibrium reactions

After calculation of the population of the first compound nucleus using the Hauser-Feshbach expressions, corrections for preequilibrium and direct reaction effects are made. The preequilibrium contribution calculations were performed using the exciton model as formulated by Kalbach in the code PRECO-B [Kal74]. The one adjustable parameter, the damping matrix element, was taken as 170 MeV^3, based on the comparison of composite neutron emission spectrum with (n,nx) spectrum at 14.1 MeV. Multiple preequilibrium emission was included using the model of Ref. [Cha94a], and does not include any adjustable parameters.

The exciton model assumes that, after the initial interaction between the incident particle and the target nucleus, the excited system can pass through a series of stages of increasing complexity before equilibrium is reached, and emission may occur from these stages, giving the preequilibrium particles. The different stages of complexity are classified

according to the number of particles and holes excited, and the exciton model calculations involve solving a series of master equations that describe the equilibration of an excited system through a series of two-body collisions producing more complex configurations of particle-hole pairs (excitons). The master equation is

$$\frac{dP(n,t)}{dt} = \lambda^+(n-2)P(n-2,t)+\lambda^-(n+2)P(n+2,t)-[\lambda^+(n)+\lambda^-(n)+W(n)]P(n,t), \quad (5.18)$$

where $P(n,t)$ is the probability that the excited nuclear system exists in the exciton state; n is number of excitons at time t, λ^+, λ^- is internal transition rates for $n \to n+2$ and $n \to n-2$, respectively and $W(n)$ is total particle emission rate from stage n summed over all outgoing particles and energies.

The initial condition for solution of these equations is

$$P(p,h,0) = \delta(p,p_0)\delta(h,h_0), \quad (5.19)$$

where the initial particle number is $p_0 = 2$ and initial hole number is $h_0 = 1$ for nucleon-induced reactions. The transition rates are calculated using Fermi's golden rule:

$$\lambda = \frac{2\pi}{\hbar} M^2 Y, \quad (5.20)$$

where M^2 is averaged squared matrix element for two-body interactions between specific initial and final states, and parametrized according to the systematics of Kalbach [Kal85] and Y is accessible phase space for the transition. To calculate the accessible phase space, the equidistant single-particle state density is used.

The emission rate for particles of type b and emission energy E is obtained by considering a detailed balance of the emission channel and the analogous absorption channel of particles b:

$$W_b(n,E) = \frac{(2s_b+1)}{\pi^2\hbar^3}\mu_b\sigma_b(\varepsilon)\varepsilon\frac{\omega(p-p_b,h,U)}{\omega(p,h,E)}Q_b(p), \quad (5.21)$$

where s_b, μ_b, p_b are the spin, reduced mass, and nucleon number of the emitted particle, U is the residual nucleus excitation energy, $\sigma_b(\varepsilon)$ is the inverse cross section evaluated at the

emission energy of b and $Q_b(p)$ is a factor that takes into account the distinguishability of neutrons and protons in the intranuclear cascade.

Finally, direct reactions for neutron inelastic scattering were included for scattering to the 2_1^+ states in ^{48}Ti using distorted-wave Born approximation theory. The deformation parameters were taken from the compilation given in the International Atomic Energy Agency Reference Input Parameter Library [rip98], and the neutron optical potential described above.

The above formalism for describing preequilibrium processes does not take into account angular momentum effects. For angular-momentum-dependent preequilibrium reactions, Chadwick et al. [Cha94b] developed an approach for estimating the spin dependences of the residual nuclei following preequilibrium decay as discussed in the Chapter 2. This approach is in parallel with the FKK quantum mechanical formalism, and gives a result for the spin distribution which is largely determined by the spin dependence of the preequilibrium particle-hole level density.

The spin distribution of residual nucleus for the preequilibrium reactions is calculated using the "cmc" program. A program "cmc" has been developed by T. Kawano [Kaw98] to calculate the multistep compound (MSC) and the multistep direct (MSD) processes by Feshbach-Kerman-Koonin theory. Since FKK theory is an extension of DWBA to the continuum state, the MSC reaction is assumed to have the same spin distribution for the resudual nucleus as for compound nucleus. The spin distribution of preequilibrium reactions in the residual nucleus is calculated with MSD for one-step process and the spin cut-off parameters of residual system were estimated. The spin cut-off parameters were incorporated into GNASH calculation, and γ-ray production cross sections were calculated. Results of the spin distribution calculations are given in the Chapter 6.

Chapter 6

Experimental results

6.1 Channel cross sections of ^{48}Ti + n reactions for E_n = 1 to 20 MeV

6.1.1 Partial γ-ray cross sections for E_n = 1 to 20 MeV

The main results in this section are: (i) the partial transition cross sections plotted in Figs. A.1–A.14, and (ii) the lower-limit estimates for the $(n, n'\gamma)$, $(n, 2n\gamma)$, $(n, p\gamma)$, and $(n, \alpha\gamma)$ channel cross sections plotted in Figs. 6.1, 6.2, 6.3, and 6.4, respectively, and (iii) channel cross sections inferred from combinations of the Hauser-Feshbach calculations and plotted in Figs. 6.5, 6.6, 6.7, and 6.8.

6.1.2 Calculations using the STAPRE reaction code

Partial γ-ray cross sections for the ^{48}Ti+n reaction have been calculated using the Hauser-Feshbach code STAPRE for neutron energies up to 20 MeV. More detailed descriptions of the inputs are in Section 5.1. The calculation includes the preequilibrium processes for the first emitted particle and produces activation cross sections as well as population cross sections for isomeric states and production cross sections for γ rays from low-lying discrete excited states. The discrete level schemes for reaction channels were taken from

ENSDF [ens]. For the present calculation, discrete low-lying excited levels up to an excitation energy of 4.074 MeV were included for the inelastic channel, and up to energy 2.682 MeV for the (n,2n) channel. Levels up to $E_x = 2.729$ MeV are included for the (n,p) channel, and up to $E_x = 1.554$ MeV for the (n,α) channel. Partial level schemes used for STAPRE calculations are shown in Figs. 5.2, 5.3, 5.4, and 5.5.

6.1.3 Lower-limit estimates

A lower limit on the ^{48}Ti(n,n$'\gamma$)^{48}Ti cross section was obtained from the data measured with the GEANIE array by summing the partial γ-ray cross sections for transitions directly populating the ground state of ^{48}Ti. Explicitly, the estimated lower-limit cross section for the inelastic channel is (see Fig. 4.11)

$$\sigma(n, n'\gamma) \equiv \sigma_\gamma(983.5) + \sigma_\gamma(2421.0) + \sigma_\gamma(3371.2) + \sigma_\gamma(3699.1) + \sigma_\gamma(3738.0), \tag{6.1}$$

where individual partial γ-ray cross sections are labeled by their energies and are listed in Appendix A. The sum in Eq. (6.1) is plotted as a function of incident neutron energy in Fig. 6.1, and compared with the STAPRE predictions shown using the solid line. Both experimental and theoretical partial sums are in excellent agreement for 1 MeV to 20 MeV. Similarly a lower-limit on the ^{48}Ti(n,2nγ)^{47}Ti cross section is given by the sum of measured partial γ-ray cross sections,

$$\begin{aligned} \sigma(n, 2n\gamma) &\equiv \sigma_\gamma(159.4) + \sigma_\gamma(1251.5) + \sigma_\gamma(1549.9) + \sigma_\gamma(1739.9) \\ &+ \sigma_\gamma(1825.1) + \sigma_\gamma(2259.3) + \sigma_\gamma(2297.0). \end{aligned} \tag{6.2}$$

This sum is plotted in Fig. 6.2. From threshold to $\approx$ 15 MeV, the experimental sum is in a very good agreement with the calculated partial sum. Above $\approx$ 15 MeV the calculated sum overpredicts the experimental one.

For charged particle emission channels, lower-limit estimation of the cross sections for ^{48}Ti(n,pγ)^{48}Sc and ^{48}Ti(n,$\alpha\gamma$)^{45}Ca reactions were based on the transition from the first excited state to ground state measured with GEANIE. The lower-limit plots for the

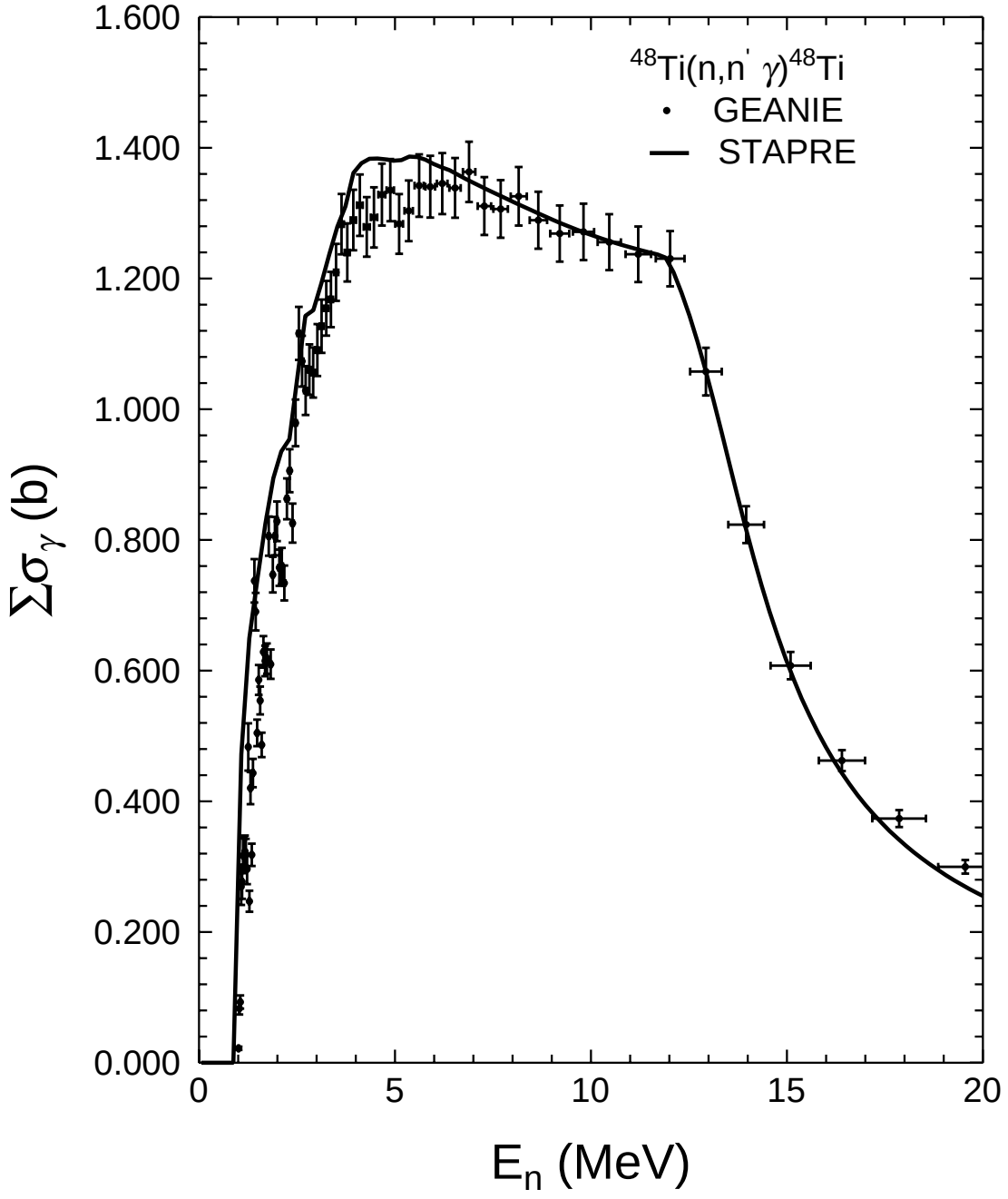

Figure 6.1: Lower limit for the ^{48}Ti(n,n$'\gamma$)^{48}Ti reaction cross section, deduced from a sum of γ-ray cross sections and compared to the STAPRE prediction.

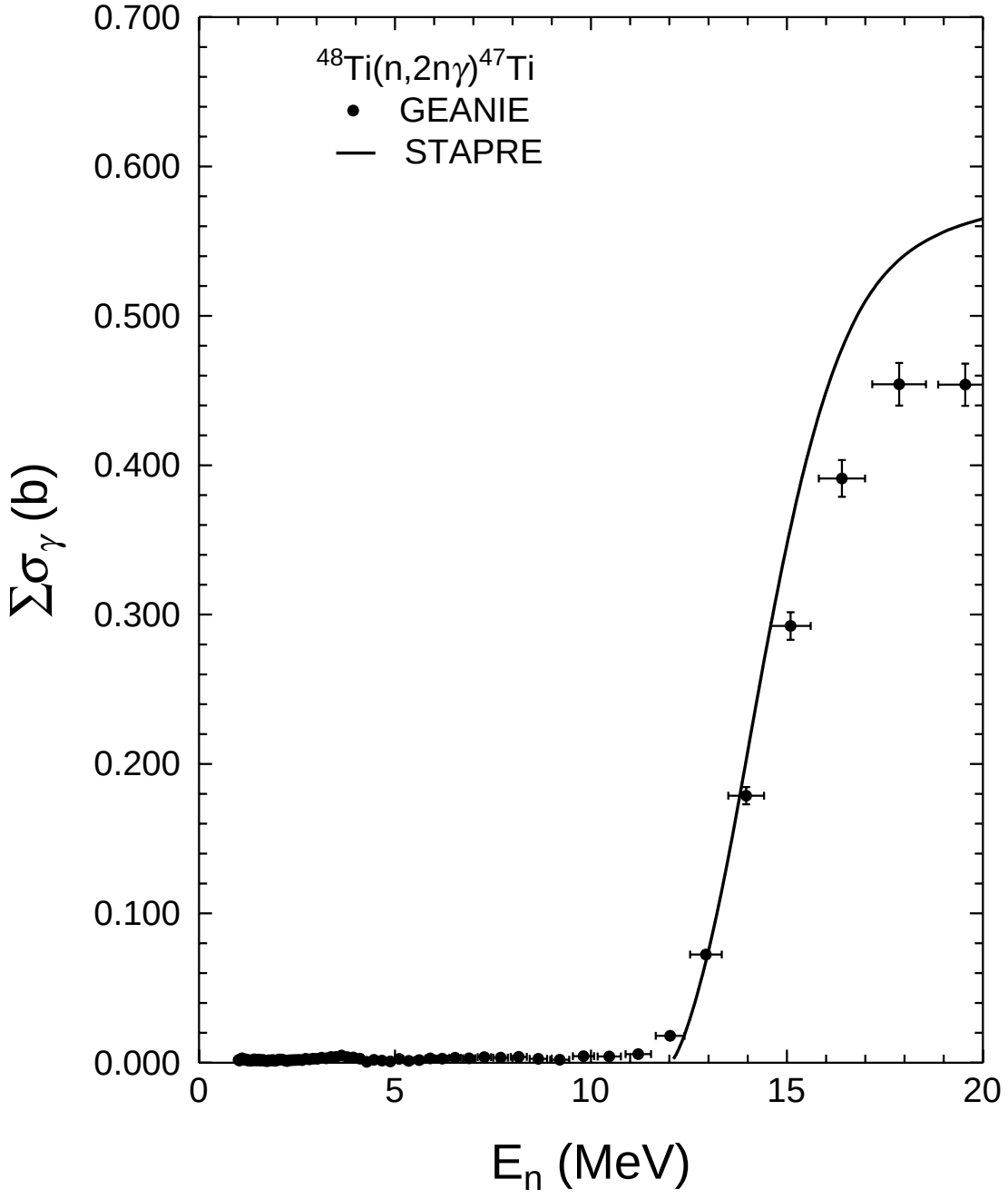

Figure 6.2: Lower limit for the ^{48}Ti(n,2nγ)^{47}Ti reaction cross section, deduced from a sum of γ-ray cross sections and compared to the STAPRE prediction.

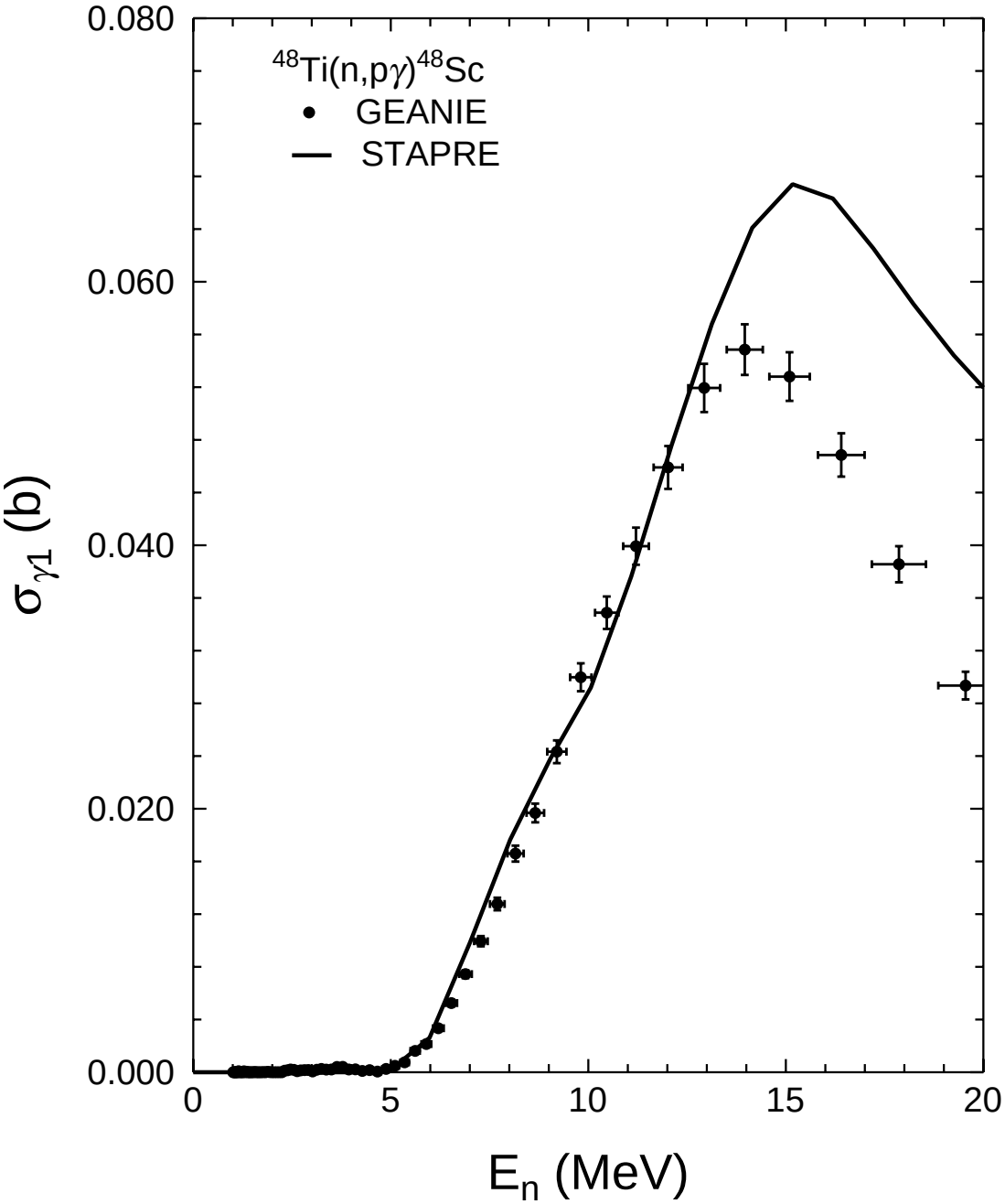

Figure 6.3: Lower limit for the ^{48}Ti(n,pγ)^{48}Sc reaction cross section, based on a single γ-ray cross section and compared to the STAPRE prediction.

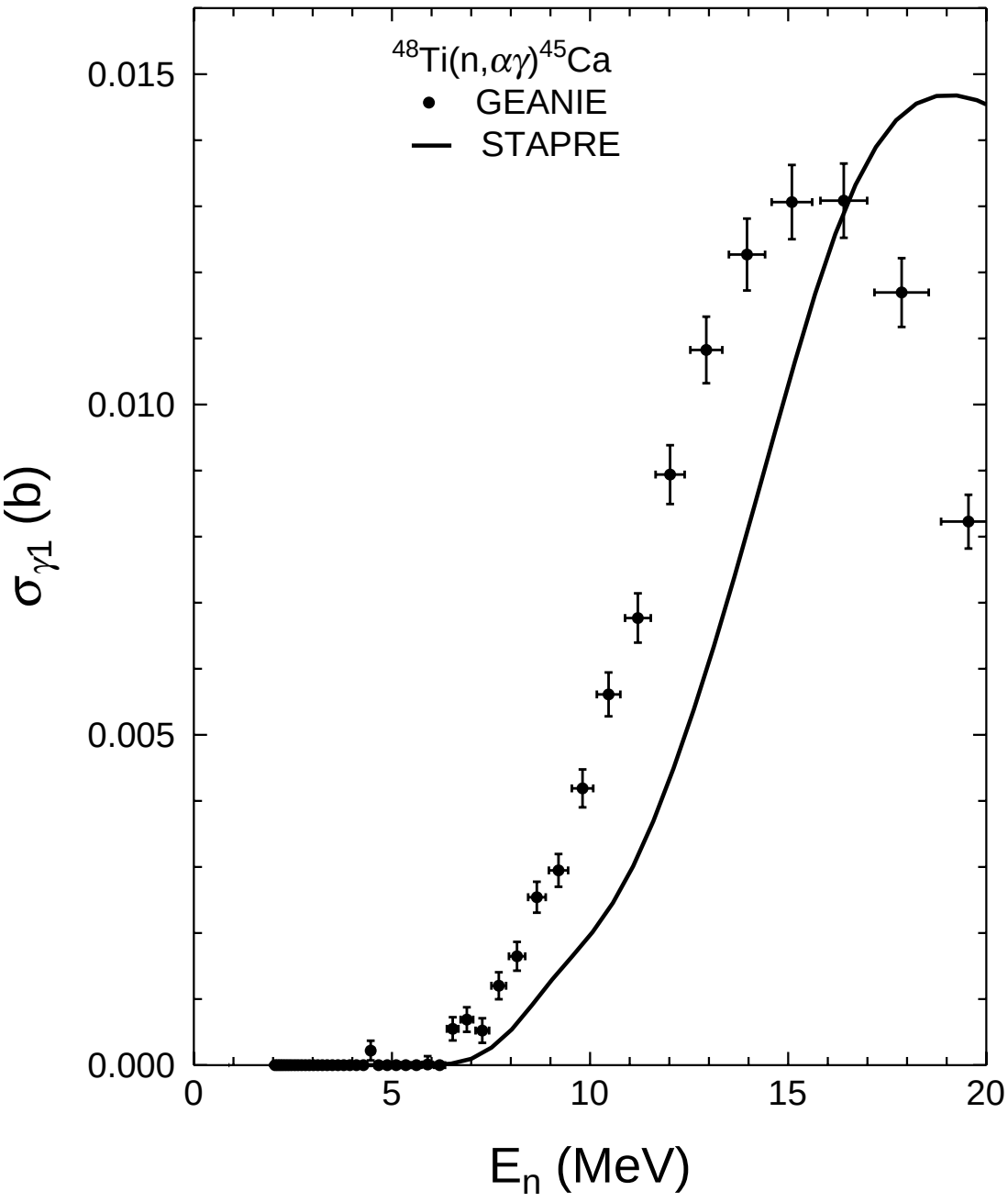

Figure 6.4: Lower limit for the ^{48}Ti(n,$\alpha\gamma$)^{45}Ca reaction cross section, based on a single γ-ray cross section and compared to the STAPRE prediction.

^{48}Ti(n,pγ) and ^{48}Ti(n,$\alpha\gamma$) reactions are shown in Figs. 6.3 and 6.4. For the (n,pγ) channel, the experimental partial cross section agrees very well with the calculated partial cross section from threshold to $\approx$ 13 MeV. Above this energy the calculated partial cross section overpredicts the measured partial cross section. On the other hand, the calculated partial cross section underpredicts the measured partial cross section for the (n,$\alpha\gamma$) channel below 15 MeV.

Systematic uncertainties which contribute to the total error are listed in the Table. 6.1.

Table 6.1: Systematic uncertainties which contribute to the total error. The quantities in the first column are defined in Eq. (4.9) with the subscripts *pl* and *cx* denoting planar and coaxial detectors, respectively. The relative uncertainties are listed in the second column, and a brief description of how these uncertainties were determined is given in the third column.

Quantity	Uncertainty (%)	Origin
a_s	0	unknown, but assumed small
ϵ_{fc}	0.42	ref. [McN99]
f_{pl}, f_{cx}	3.0	ref. [McN99]
α_γ	6.0	ref. [McN99]
ϵ_{pl}	4.8	calculated average of individual detector efficiencies
ϵ_{cx}	4.8	calculated average of individual detector efficiencies

6.1.4 Channel cross sections combined with Hauser-Feshbach model calculations

The individual partial cross sections have been combined to produce an experimental lower limit on the ^{48}Ti(n,n$'$)^{48}Ti, ^{48}Ti(n,2n)^{47}Ti, ^{48}Ti(n,p)^{48}Sc, and ^{48}Ti(n,α)^{45}Ca cross sections. These lower limits were combined with the Hauser-Feshbach calculations to produce a model-dependent estimate of the cross sections using the following equation:

$$\sigma_{reaction}^{deduced} = \sum_i \sigma_{\gamma_i}^{measured} \times \frac{\sigma_{reaction}^{calculated}}{\sum_i \sigma_{\gamma_i}^{calculated}}, \tag{6.3}$$

where $\sigma_\gamma^{measured}$ is measured with GEANIE, and $\sigma_\gamma^{calculated}$ is calculated using the STAPRE code. The cross sections obtained in this manner are shown in Figs. 6.5, 6.6, 6.7, and 6.8. We assume that while the calculation may not reproduce the details of the absolute magnitudes of the cross sections, it can accurately model the relative partitioning of the cross sections among the discrete γ rays.

6.2 Partial γ-ray cross sections for E_n = 1 to 200 MeV

The ability to perform neutron cross section measurements over a wide range of neutron energies ranging from a few MeV up to several hundred MeV provides a unique opportunity to test sophisticated reaction modeling codes. In the neutron energy up to several hundred MeV, a region is entered where preequilibrium reactions are the dominating reaction mechanism; this region has not been well explored with the neutron-induced reactions [Gar00]. The observation of 13 different isotopes in the present work provides a demanding test of reaction model calculations, and is the first study in this mass region to extract γ-ray excitation functions for many different reaction channels over the wide range of neutron bombarding energies. In addition to the comparisons with the STAPRE reaction code, the results of the present work were also compared with the GNASH reaction code calculations. The GNASH code employs Hauser-Feshbach calculations with preequilibrium and direct reaction contributions. Both calculations are sensitive to the accuracy of the level schemes. In some cases, incomplete knowledge of the level scheme, such as missed strong feeding transitions, incorrect branching ratios etc., introduces a bias into the calculations. This is generally not a serious problem for even-even, or most odd nuclei in the region of ^{48}Ti. Model predictions with a Hauser-Feshbach code such as GNASH are challenging since, for a good agreement with experimental results, theoretical descriptions must correctly predict the overall break-up channel cross sections and must correctly predict the angular momentum transfers and γ-ray cascades in the residual nuclei.

Including ^{48}Ti, a total of 13 different isotopes were observed for which excitation

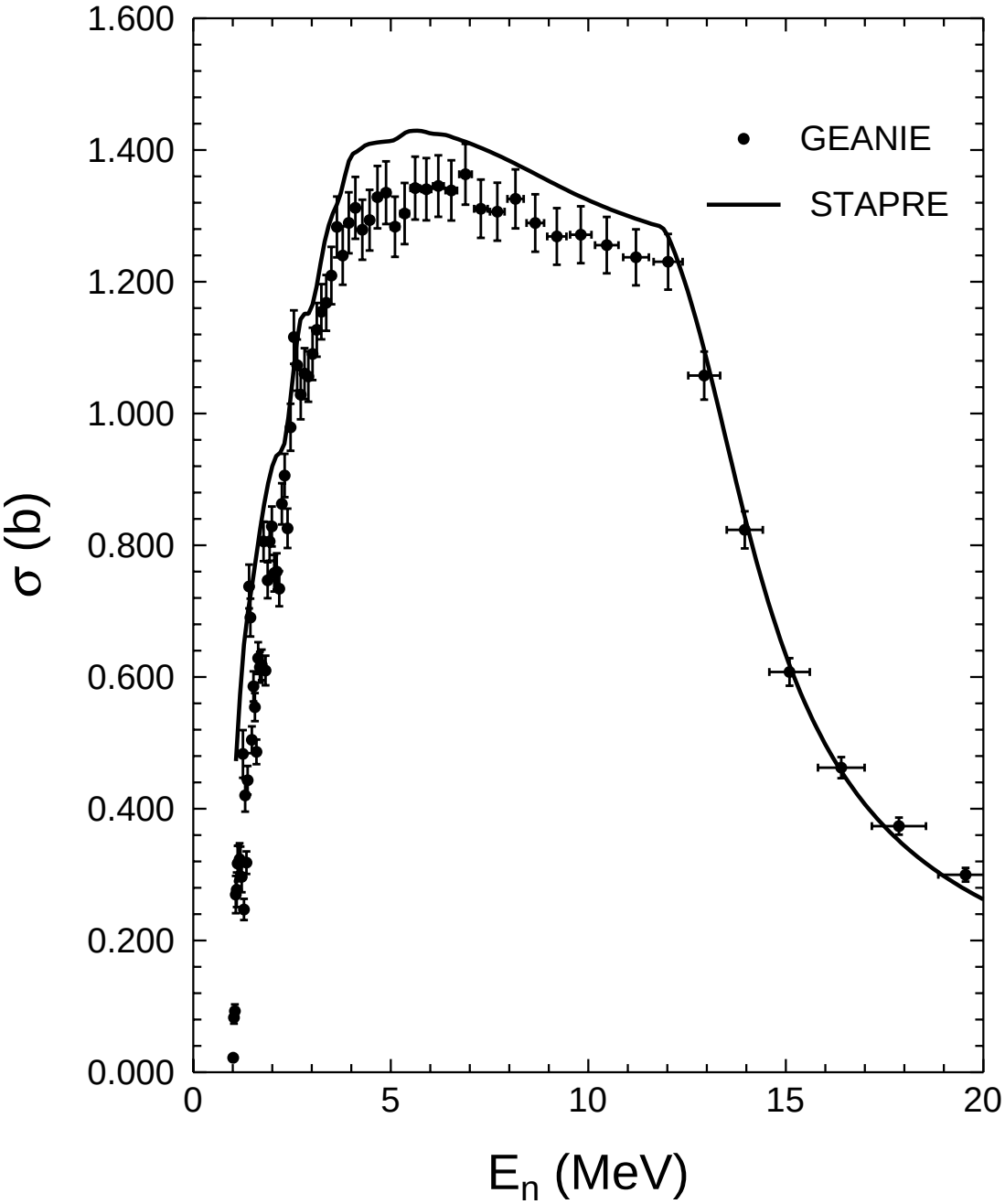

Figure 6.5: Deduced cross section for the ^{48}Ti(n,n$'$)^{48}Ti reaction compared to the STAPRE prediction.

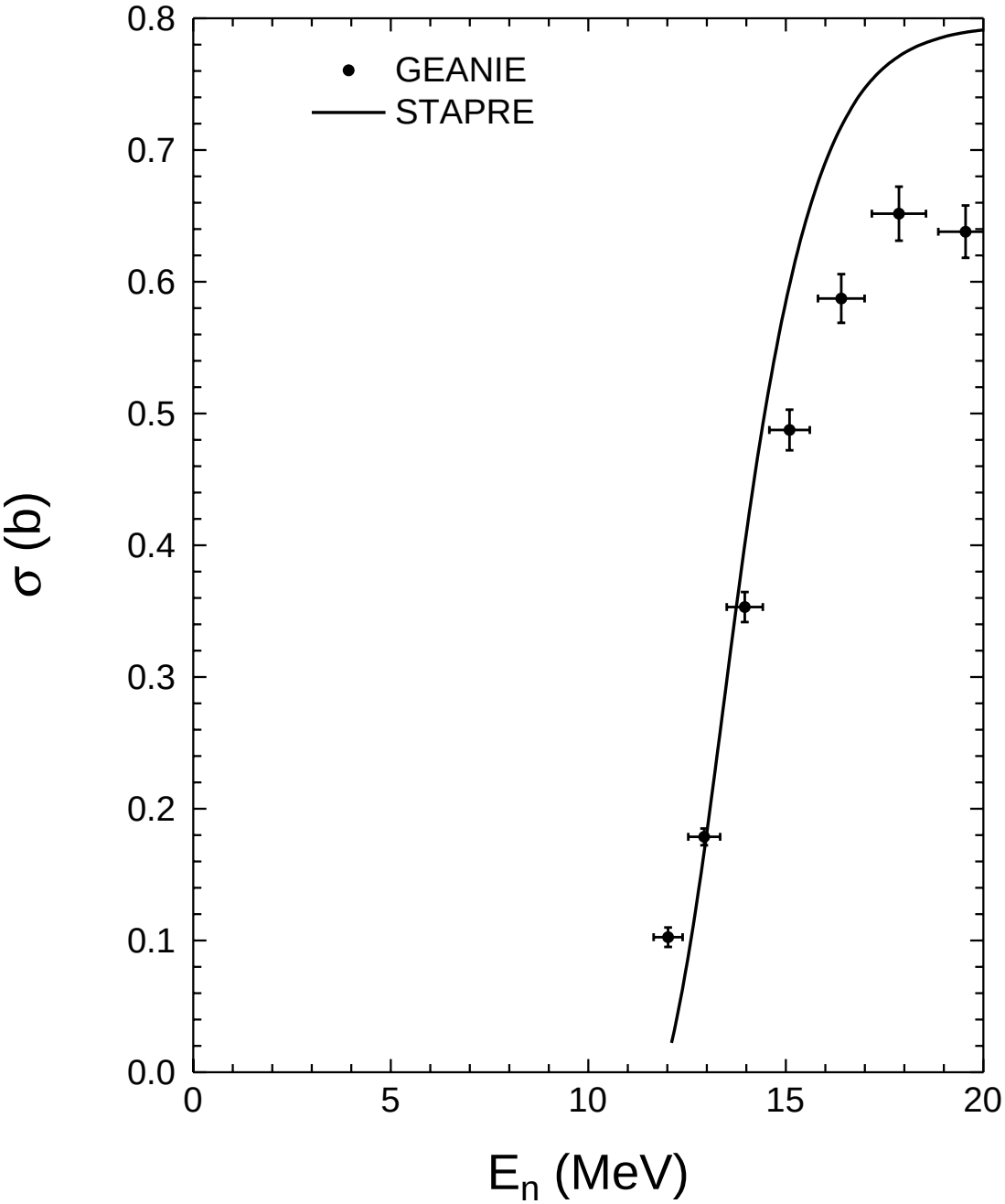

Figure 6.6: Deduced cross section for the ^{48}Ti(n,2n)^{47}Ti reaction compared to the STAPRE prediction.

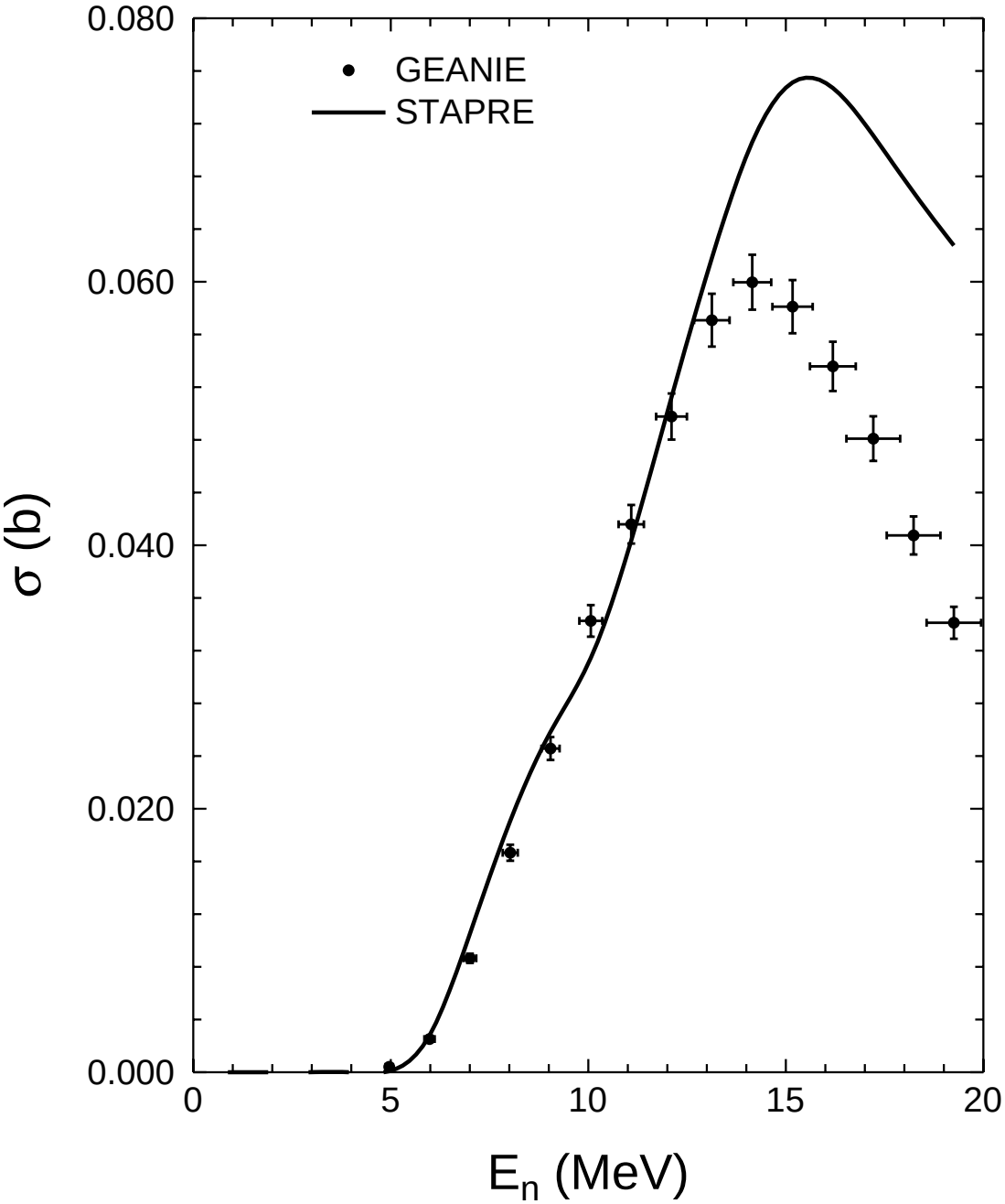

Figure 6.7: Deduced cross section for the ^{48}Ti(n,p)^{48}Sc reaction compared to the STAPRE prediction.

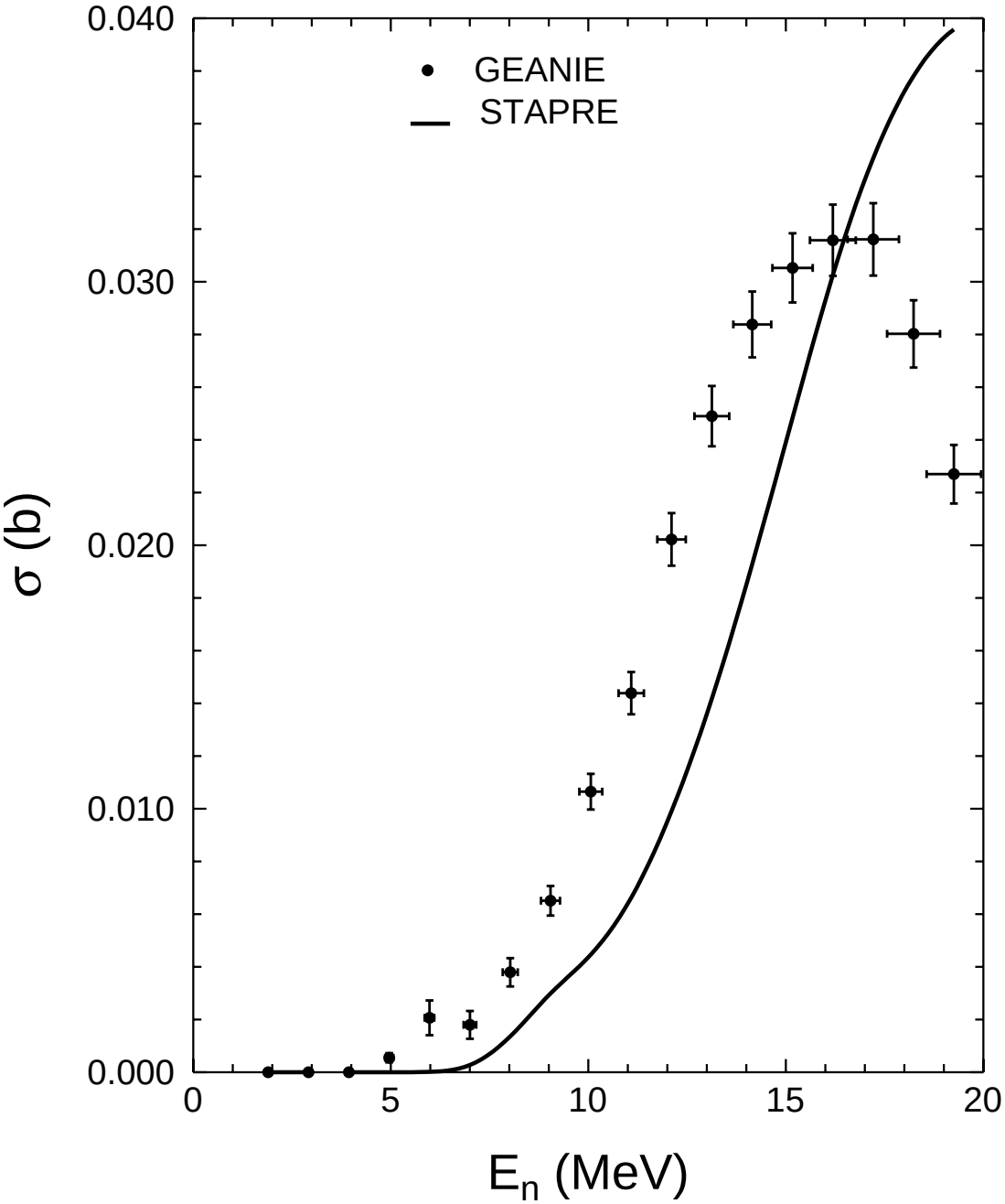

Figure 6.8: Deduced cross section for the ^{48}Ti(n,α)^{45}Ca reaction compared to the STAPRE prediction.

functions could be extracted, the lightest being ^{42}Ca via the $(n, \alpha 4n)$ reaction channel.

The Ti isotopes

A total of four Ti isotopes were observed from ^{48}Ti to ^{45}Ti. The experimental partial cross sections for individual γ-rays are compared with the GNASH calculations for these nuclei in Figs. 6.9-6.11. The overall agreement was excellent, especially for $(n, n'\gamma)$ channel neutron energy up to 20 MeV. There are some discrepancies, particularly for the $(n, 2n\gamma)$ reaction channel. The measured $(n, n'\gamma)$ cross section for the 983-keV 2^+ to $0^+ g.s.$ transition in ^{48}Ti (which represents most of the total inelastic cross section) is considerably higher than calculated for neutron energies above 25 MeV (see Fig. 6.9). Much of this discrepancy may be due to multiple-scattering effects in the data. Such an underprediction of calculation occurred in the several previous works for ^{207,208}Pb$(n, xn\gamma)$ [Von94], ^{92}Mo$(n, xnypz\alpha\gamma)$ [Gar00], and ^{196}Pt$(n, xnyp\gamma)$ [Tav01] investigated using the GEANIE array or similar detectors. Most of the transitions in $(n, n'\gamma)$ reaction channel are in excellent agreement with theoretical calculations.

Transitions in the $(n, 2n\gamma)$ reaction channel are shown in Fig. 6.10. For a transition between the first excited state and the ground state in ^{47}Ti the calculation overpredicts the experimental data above the threshold energy. In this energy region, the preequilibrium reaction plays an important role. Unlike this overprediction, the GNASH calculation underpredicts the transitions between $11/2^-$ to $7/2^-$, $3/2^+$ to $5/2^- g.s.$ levels. The reason for this discrepancy is unknown. The excitation functions for the lighter Ti isotopes, shown in Fig. 6.11, are in good overall agreement with the GNASH calculations, both in shape and magnitude. For ^{45}Ti, the cross sections do not fall as rapidly as the calculations suggest. However, it is satisfying that the portion of the excitation function dominated by the compound processes are well reproduced.

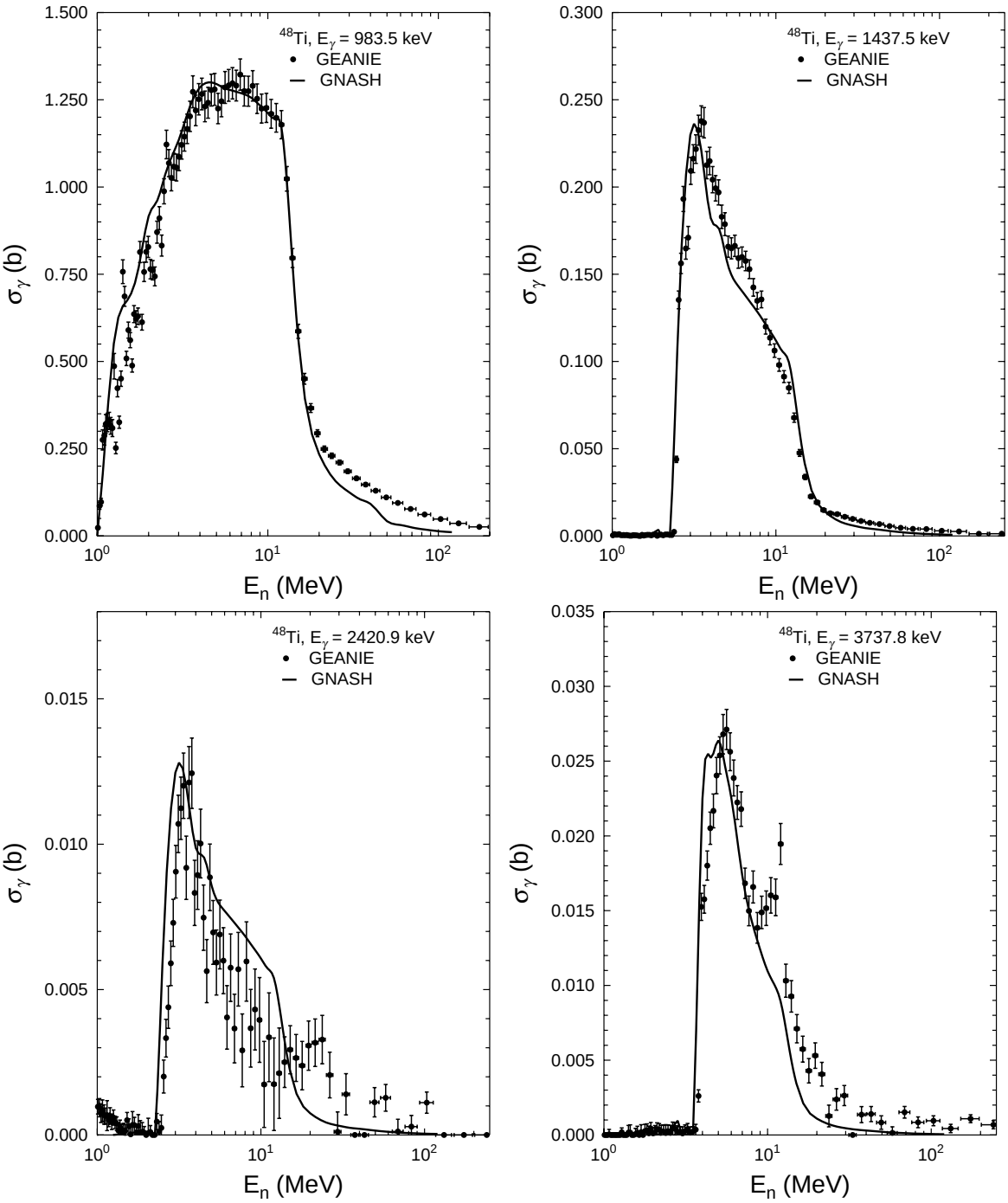

Figure 6.9: Partial γ-ray cross sections for E_γ = 983-keV, 1437-keV, 2421-keV, and 3737-keV transitions in the $(n, n'\gamma)$ reaction for neutron energies between 1 to 200 MeV. These are transitions between 2_1^+ to $0_1^+ g.s.$, 2_2^+ to 2_1^+, 2_2^+ to $0_1^+ g.s.$, and 1_1^+ to $0_1^+ g.s.$ states, respectively. Comparison with the GNASH predictions are shown.

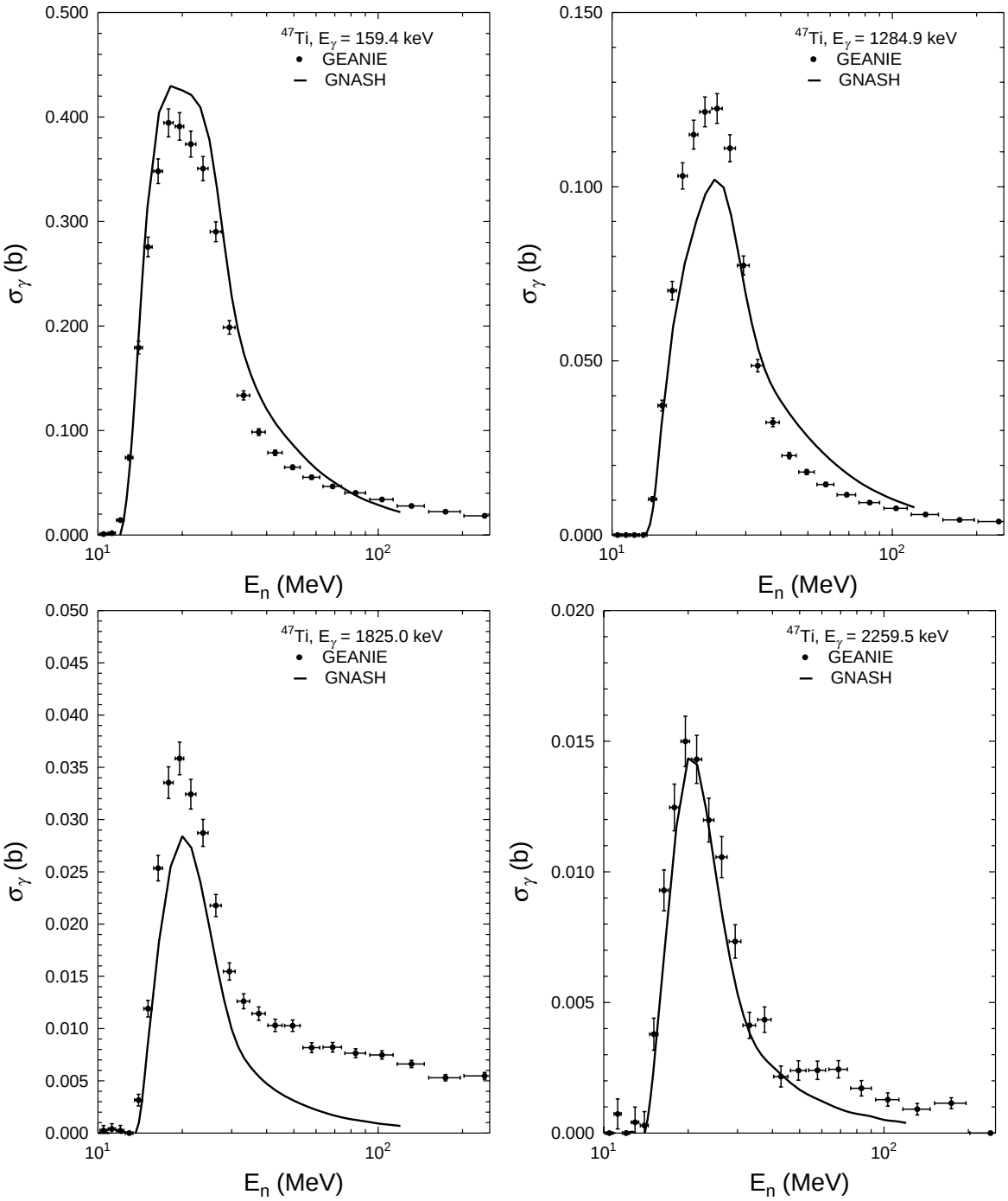

Figure 6.10: Partial γ-ray cross sections for E_γ = 159-keV, 1285-keV, 1825-keV, and 2260-keV transitions in the $(n, 2n\gamma)$ reaction for neutron energies between 1 to 200 MeV. These are transitions between $7/2^-$ to $5/2^- g.s.$, $11/2^-$ to $7/2^-$, $3/2^+$ to $5/2^- g.s.$, and $5/2^+$ to $5/2^- g.s.$ states, respectively. Comparison with the GNASH predictions are shown.

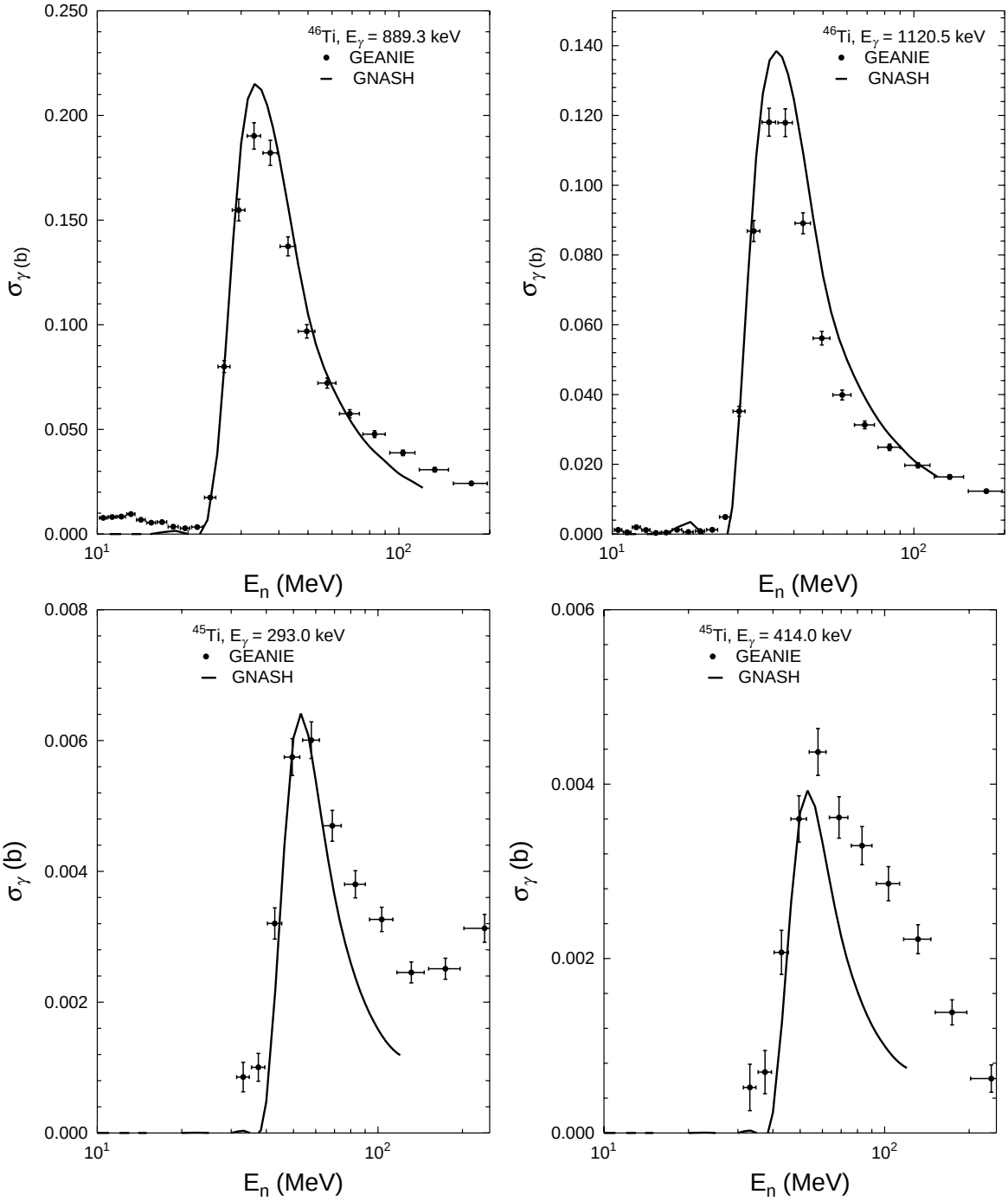

Figure 6.11: Partial γ-ray cross sections for E_γ = 889-keV, 1120-keV transitions in the $(n, 3n\gamma)$ reaction and E_γ = 293-keV, 414-keV transitions in the $(n, 4n\gamma)$ reaction for neutron energies between 1 to 200 MeV. These are transition between 2_1^+ to $0^+ g.s.$, 4_1^+ to 2_1^+ states in ^{46}Ti and $3/2_1^+$ to $3/2_1^-$, $5/2_1^+$ to $3/2_1^+$ states in ^{45}Ti. Comparison with the GNASH predictions are shown.

The Sc isotopes

The Sc isotopes from ^{48}Sc, via (n,p) channel, to ^{44}Sc, via $(n,4np)$ channel, were observed to be strongly populated in the reaction. Cross sections for transition in Sc nuclei are shown in Figs. 6.12–6.14. As can be seen in Fig. 6.12, the excitation functions for the (n,p) channel are in good agreement with the GNASH predictions. The excitation functions show the typical behavior characteristic of a charged-particle-exit channel, i.e., near the threshold, the excitation functions rise slower than those of the neutron exit channel. This is due to the Coulomb barrier for the evaporation of charged particles. While the (n,p) Q value is -3.21 MeV, most of the ^{48}Sc γ rays are not observed until ≈ 5 MeV, indicating that approximately 2 MeV of the excitation energy is required before protons can be evaporated.

^{47}Sc is the heaviest Sc isotope where composite particles could be emitted the compound system of ^{48}Ti. The difference in the thresholds between the (n,d) and (n,np) reactions is 2.27 MeV. Shown in Fig. 6.13 are results for transitions in the ^{47}Sc and ^{46}Sc nuclei. Since none of the prompt γ rays are observed below the (n,np) threshold of 11.7 MeV, there is no positive evidence of deuteron emission at low neutron bombarding energies. The observed transition between $3/2^-_1$ to $7/2^- g.s.$ levels in ^{47}Sc was over two orders of magnitude higher than the model prediction. In the experiment, this line is located close to the "neutron bump" therefore it might have been contaminated by it. It is apparent upon inspection of Fig. 6.13 that there is a good agreement for the positive-parity states, but poorer agreement for the negative-parity states.

Excitation functions for transitions from the lightest Sc nuclei observed in the present work, ^{45}Sc and ^{44}Sc, are shown in Fig. 6.14. Of interest are the threshold behavior of the excitation functions in that they increase more slowly than the calculations predict. For ^{44}Sc, the calculated excitation function is much narrower than the observed one. In the excitation function for the transition between 4^+_1 to $2^+ g.s.$ in ^{44}Sc, the peak below the threshold must be a contamination peak from some other isotopes.

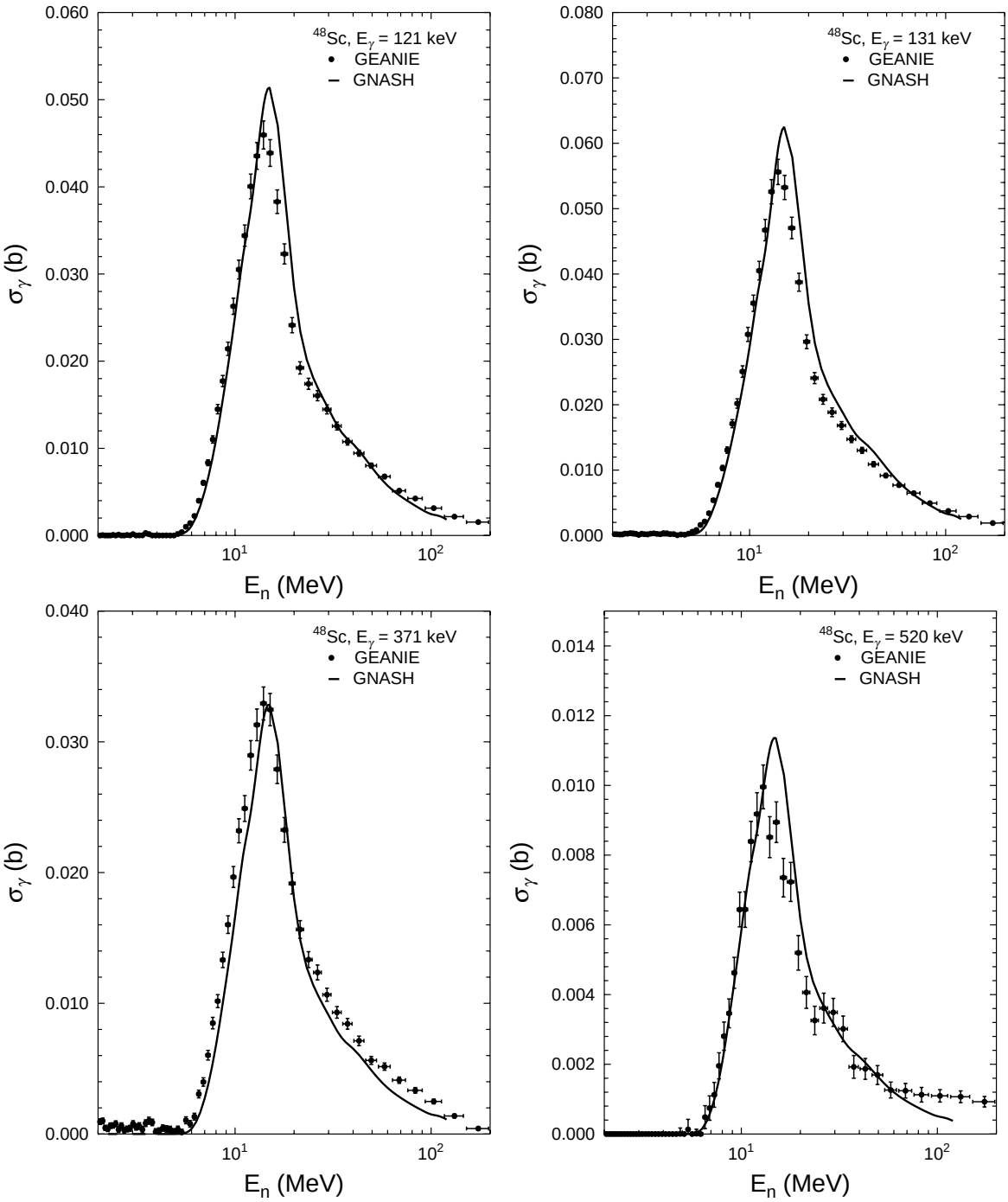

Figure 6.12: Partial γ-ray cross sections for E_γ = 121-keV, 131-keV, 371-keV, and 520-keV transitions in the $(n, p\gamma)$ reaction for neutron energies between 1 to 200 MeV. These are transitions between 4_1^+ to 5_1^+, 5_1^+ to $6^+ g.s.$, 3_1^+ to 4_1^+, and 2_1^+ to 3_1^+ states, respectively. Comparison with the GNASH predictions are shown.

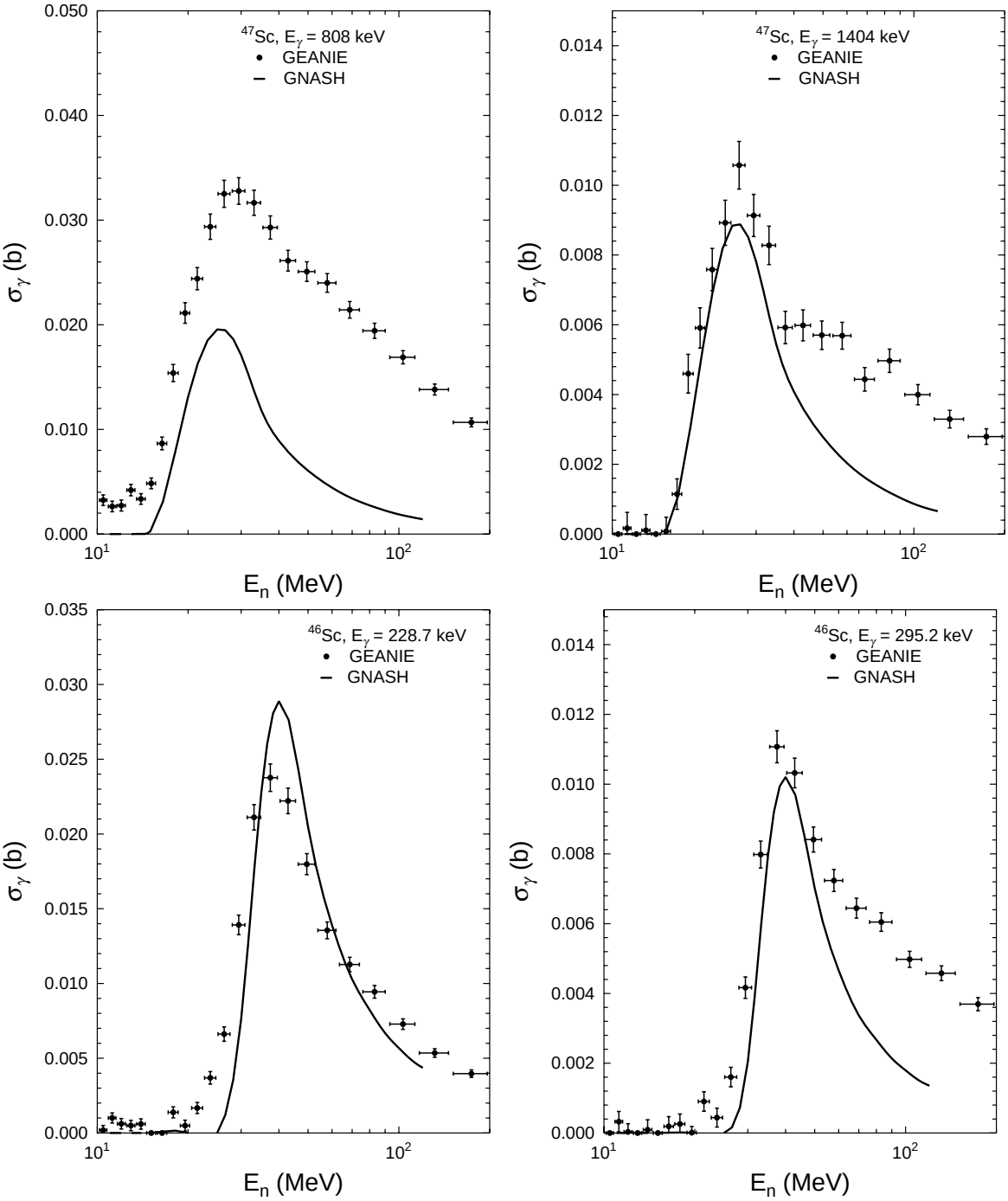

Figure 6.13: Partial γ-ray cross sections for E_γ = 808-keV, 1404-keV transitions in the $(n, np\gamma)$ reaction and E_γ = 228-keV, 295-keV transitions in the $(n, 2np\gamma)$ reaction for neutron energies between 1 to 200 MeV. These are transitions between $3/2^-_1$ to $7/2^- g.s.$, $5/2^+_1$ to $7/2^- g.s.$ states in ^{47}Sc and 5^+_1 to 6^+_1, 3^-_1 to 2^-_1 states in ^{46}Sc, respectively. Comparison with the GNASH predictions are shown.

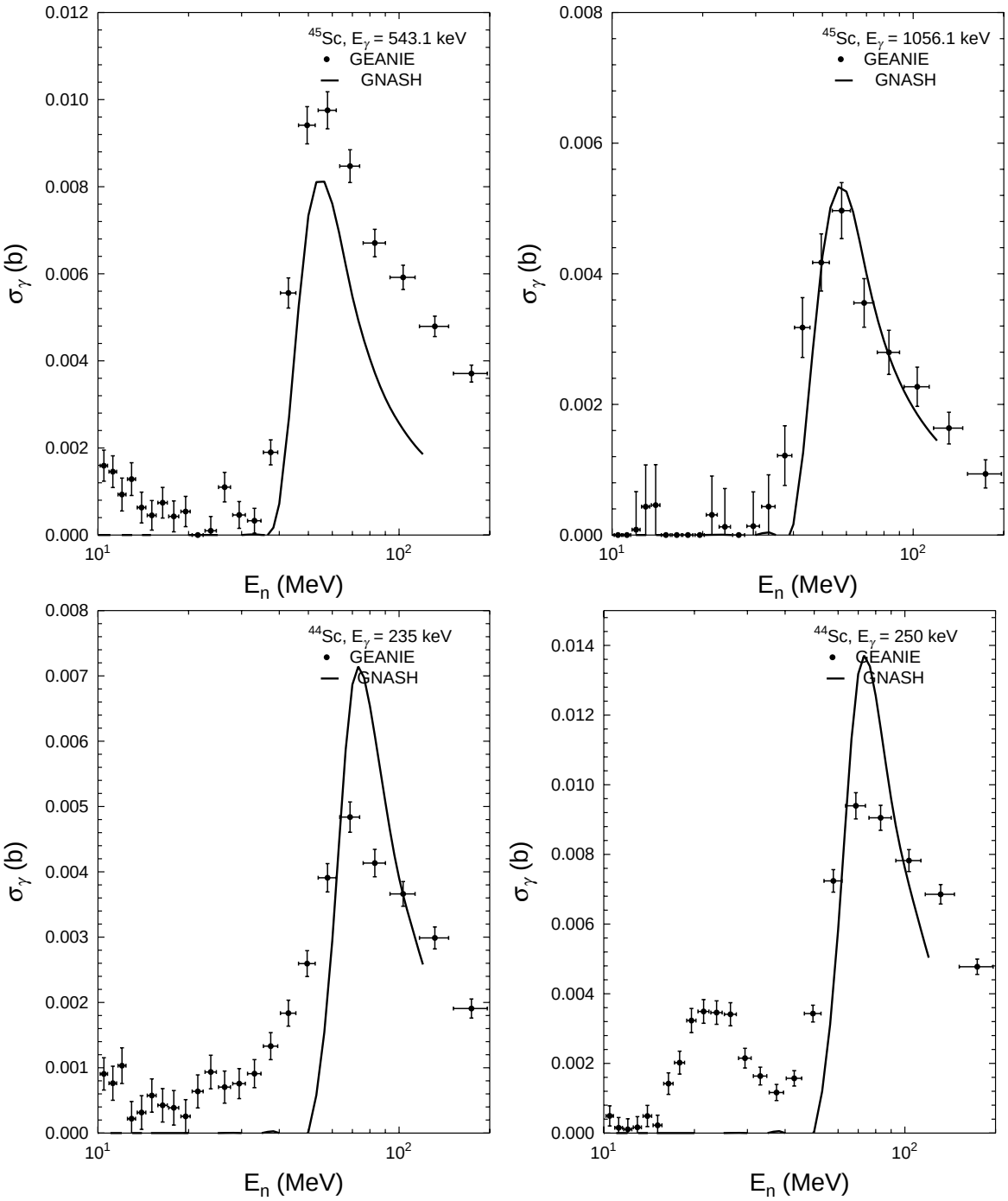

Figure 6.14: Partial γ-ray cross sections for E_γ = 543-keV, 1056-keV transitions in the $(n, 3np\gamma)$ and E_γ = 235-keV, 350-keV transitions in the $(n, 4np\gamma)$ reaction for neutron energies between 1 to 200 MeV. These are transitions between $5/2_1^+$ to $7/2^- g.s.$, $11/2_1^+$ to $7/2_1^+$ states in ^{45}Sc and 2_1^- to $2^+ g.s.$, 4_1^+ to $2^+ g.s.$ states in ^{44}Sc, respectively. Comparison with the GNASH predictions are shown.

The Ca isotopes

Excitation functions for γ rays from the Ca isotopes, ranging from ^{45}Ca to ^{42}Ca, are shown in Figs. 6.15−6.16. In general, the calculations are in good agreement with the experimental excitation functions, especially the shape of the curve. The curves show a definite double-humped structure, which is attributed to an α emission at low neutron energies followed by contributions from $2p2n$ emission for higher neutron energies. The actual threshold for an α emission channel is higher than the kinematic threshold due to a Coulomb barrier. Shown in Fig. 6.15 are excitation functions for transitions assigned to ^{45}Ca and ^{44}Ca. In the first panel, the calculation for the 174-keV $5/2^-$ to $7/2^-$ ground state transition is underpredicted. Changing the default level density parameters may change the predictions. For the 4^+ to 2^+ and 2^+ to 0^+ transitions in the $(n, n\alpha/3n2p)$ channel, the adjustment of the level density parameters may improve the predictions of the $(n, n\alpha)$ channel, but at the expense of the good description of the $(n, 3n2p)$ channel. Fig. 6.16 displays the excitation functions observed for transitions that are assigned to ^{43}Ca and ^{42}Ca. The shapes of the cross sections for transitions in high particle multiplicity reactions are reproduced reasonably well. It is interesting to note that the cross sections still have an observable dip between the $(n, xn\alpha)$ and $[n, (x+2)n2p]$ channels.

6.3 Spin distribution of the preequilibrium reactions

In this work, the spin distribution of the preequilibrium reactions in the residual nucleus is calculated using the quantum mechanical theories by Feshbach, Kerman, and Kooning (FKK) with the multistep direct (MSD) approach. The MSD one-step process for preequilibrium reactions are calculated using the "cmc" code. For this calculation, the multistep compound (MSC) spin distribution is assumed be the same as the compound residual nucleus spin distribution. The transferred spin distribution in preequilibrium reactions is calculated for incident neutron energies 15 MeV, 20 MeV, 25 MeV, 30 MeV, and 35 MeV for ^{48}Ti target. As an example, some of the calculated spin distributions are

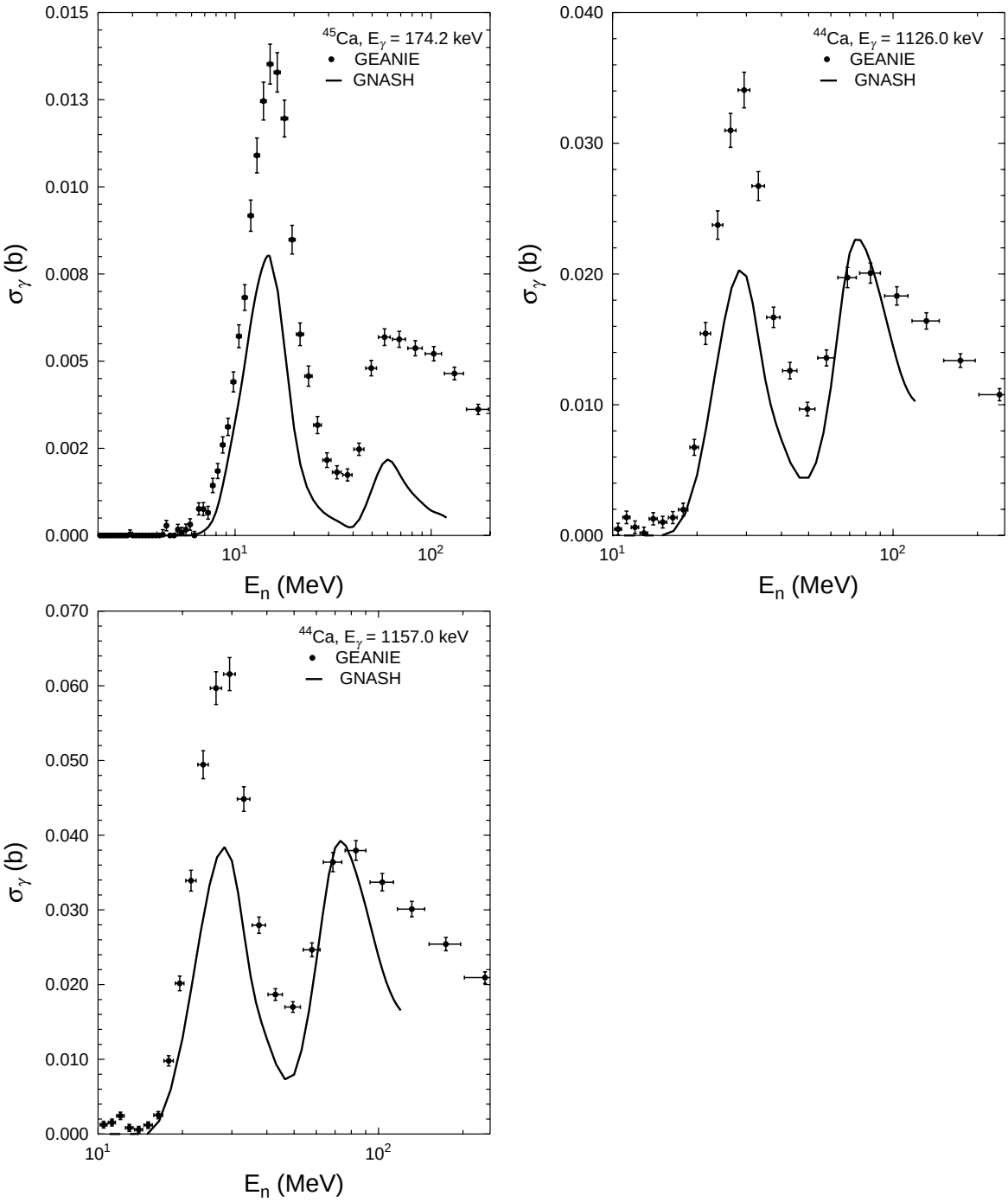

Figure 6.15: Partial γ-ray cross sections for $E_\gamma = 174$-keV transition in $(n, \alpha/2n2p\gamma)$ reaction and $E_\gamma = 1126$-keV, 1157-keV transitions in $(n, n\alpha/3n2p\gamma)$reaction for neutron energies between 1 to 200 MeV. Transitions between $5/2^-_1$ to $7/2^- g.s.$ in ^{45}Ca and 4^+_1 to 2^+_1, 2^+_1 to $0^+ g.s.$ in ^{44}Ca, respectively, compared with GNASH predictions.

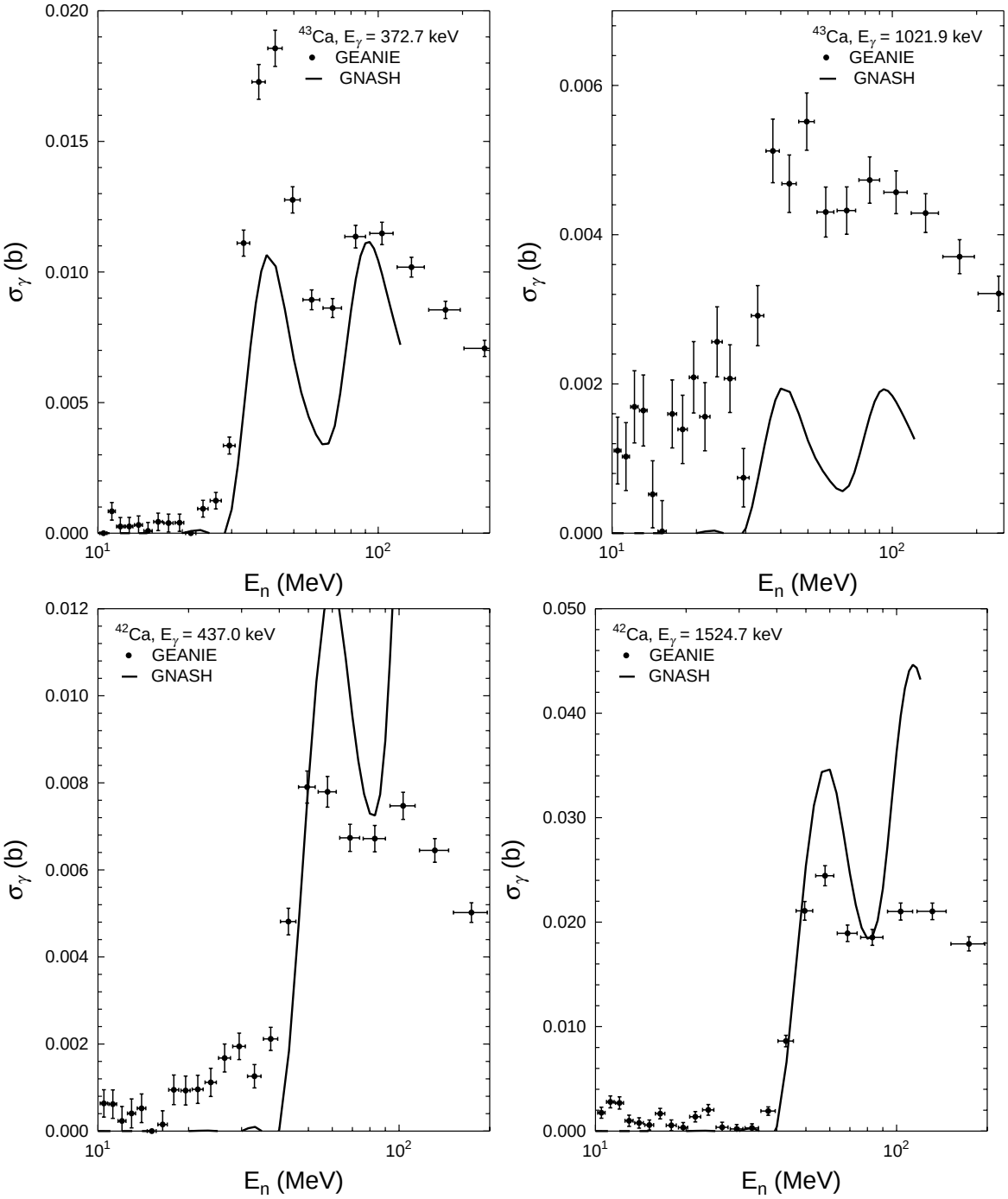

Figure 6.16: Partial γ-ray cross sections for E_γ = 373-keV, 1021-keV transitions in $(n, 2n\alpha/4n2p\gamma)$ reaction and E_γ = 437-keV, 1525-keV transitions in $(n, 3n\alpha/5n2p\gamma)$ reaction for neutron energies between 1 to 200 MeV. Transitions between $5/2_1^-$ to $7/2^- g.s.$, $5/2_1^+$ to $5/2_1^-$ in ^{43}Ca and 6_1^+ to 4_1^+, 2_1^+ to $0^+ g.s.$ in ^{42}Ca, respectively, compared with GNASH predictions.

shown in Figs. 6.17−6.20 for the incident neutron energy 20 MeV. The histograms are the transferred spin populations calculated using the FKK MSD one-step calculation. In order to incorporate the spin distribution into the GNASH code the histograms need smoothing, therefore histograms of the spin distribution are fitted by the function given by Eq. (2.42) and the spin cut-off parameters are obtained from the fit. The spin cut-off parameters of residual system are shown in the Fig. 6.21. The calculated spin distribution using the FKK-MSD are incorporated into the GNASH input used for weighting of level density in the continuum region where the preequilibrium component is important. Using these inputs, the γ-ray production cross sections were calculated. Throughout this work, this calculation is referred to as GNASH-FKK.

For the (n, n') channel, the effect on the three transitions is investigated. First, in Fig. 6.22 the 2^+ to 0^+ transition is shown; both GNASH and GNASH-FKK show good agreement with the experimental data and are lower than the data for $E_n \geq 15$ MeV. The difference in the spin distribution for these two calculations is not readily apparent in the case of this low spin transition. The second case is the 4^+ to 2^+ transition in the same channel shown in Fig. 6.23. In this case, the GNASH predictions are somewhat higher than the experimental result for $E_n = 6 - 11$ MeV. More importantly, the GNASH-FKK is much strongly suppressed compared to the GNASH and experimental data. Similarly, for the 6^+ to 4^+ transition in the (n, n') channel shown in Fig. 6.24, the GNASH-FKK is suppressed at all neutron energies indicating the effect of preequilibrium reaction.

For the $(n, 2n)$ channel, the transition from the first excited state to the ground state is considered. The GNASH-FKK predictions are in much better agreement with data than the GNASH prediction.

In order to demonstrate the effect of the difference in spin distribution in the two calculations, the ratios of the partial γ-ray cross section for 6^+ to 4^+ and the total inelastic scattering are considered in Fig. 6.27. The ratio predicted using the GNASH without taking into account the preequilibrium reaction, is clearly in disagreement with data, i.e., while data decreases with increasing neutron energy, the GNASH prediction keep increasing.

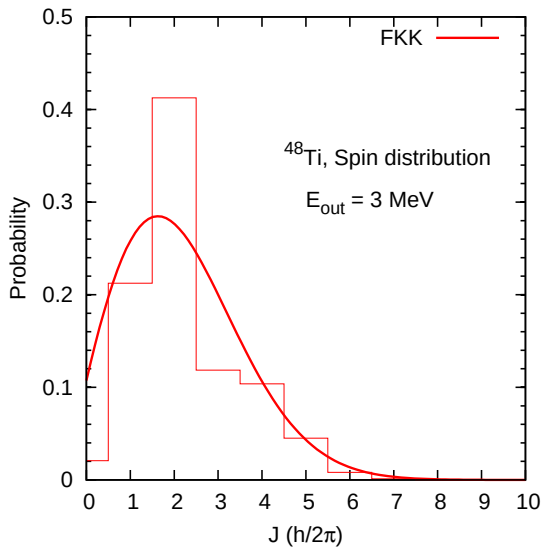

Figure 6.17: Spin distribution of the ^{48}Ti + n reaction for incident neutron energy of 20 MeV and outgoing neutron energy of 3 MeV

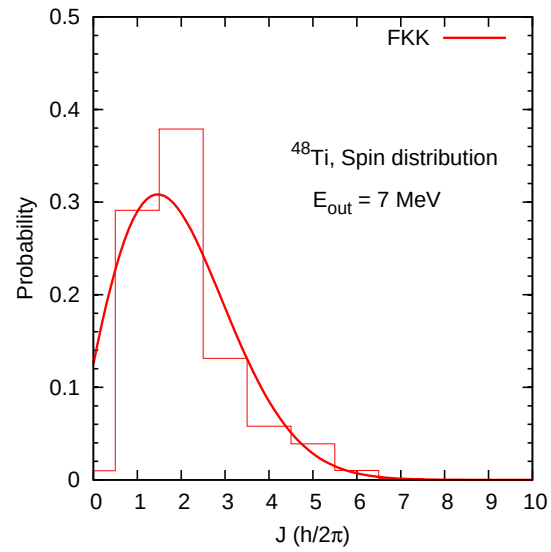

Figure 6.18: Spin distribution of the ^{48}Ti + n reaction for incident neutron energy of 20 MeV and outgoing neutron energy of 7 MeV

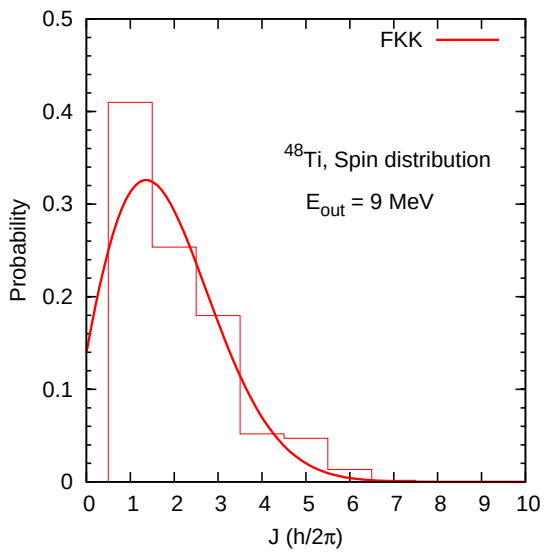

Figure 6.19: Spin distribution of the ^{48}Ti + n reaction for incident neutron energy of 20 MeV and outgoing neutron energy of 9 MeV

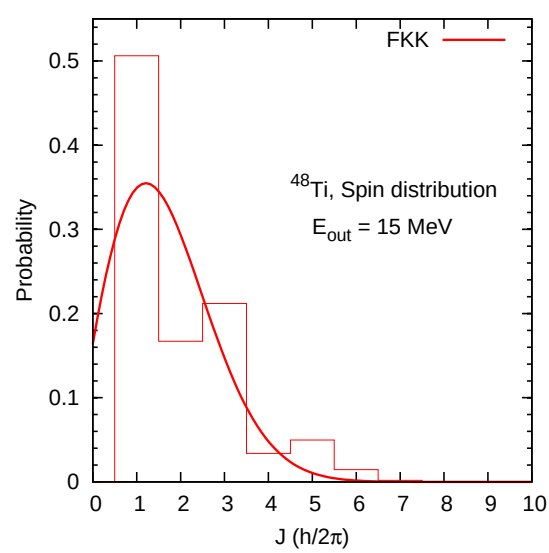

Figure 6.20: Spin distribution of the ^{48}Ti + n reaction for incident neutron energy of 20 MeV and outgoing neutron energy of 15 MeV

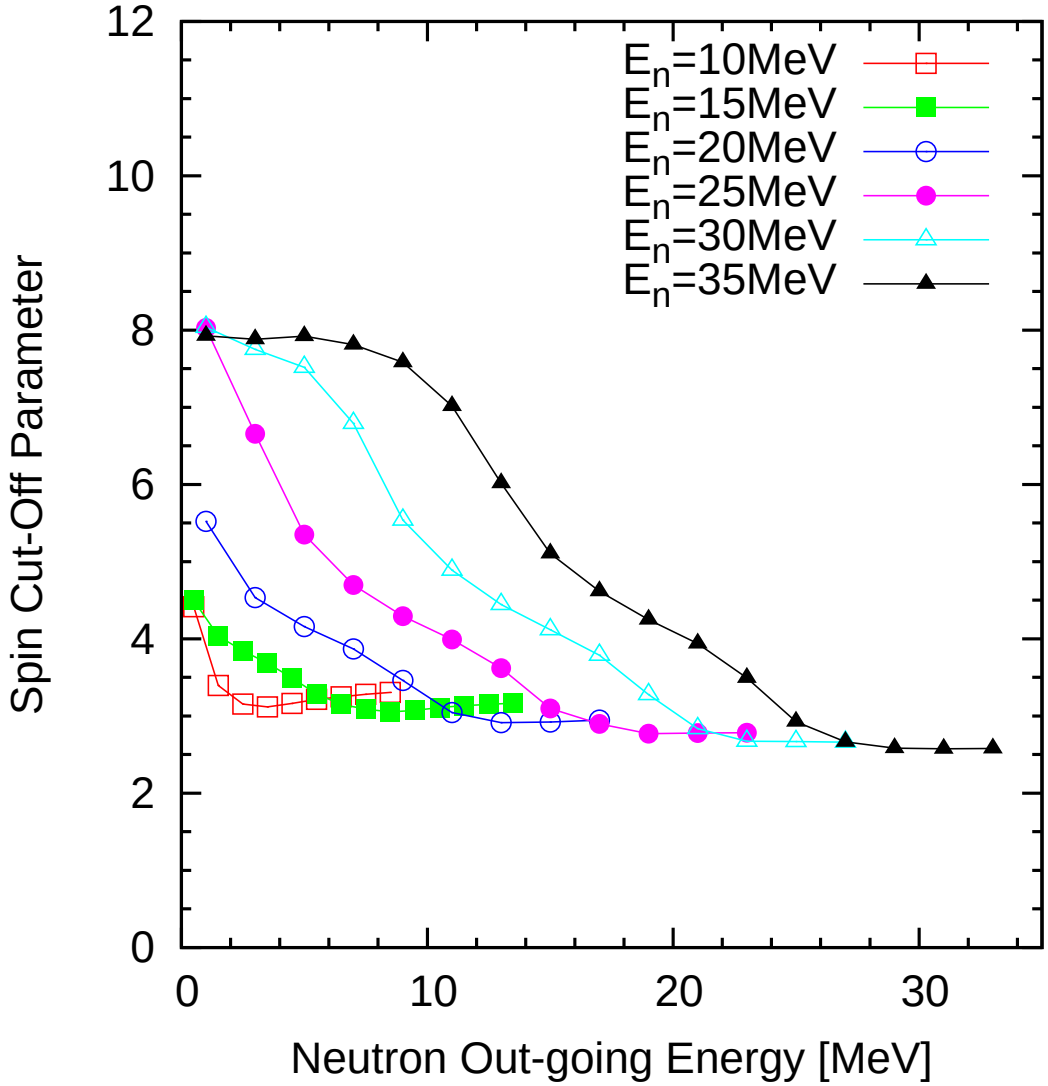

Figure 6.21: Spin cut-off parameters

After inclusion of the spin distribution calculated using the preequilibrium effects, the ratio is more similar to the data. The difference in magnitude may be improved by further development of the model. The same ratio between the 4^+ to 2^+ transition cross section and the total inelastic cross section is shown Fig. 6.26. The calculations of the GNASH and GNASH-FKK are similar in shape with the measured ratio. But GNASH prediction tends to increase in with increasing neutron energies, while the experimental data tend to be constant at increasing neutron energy. When the spin distribution in the preequilibrium reaction is included, the ratio is much more closer to experimental data. This clearly demonstrates the importance of including the effect of preequilibrium reactions.

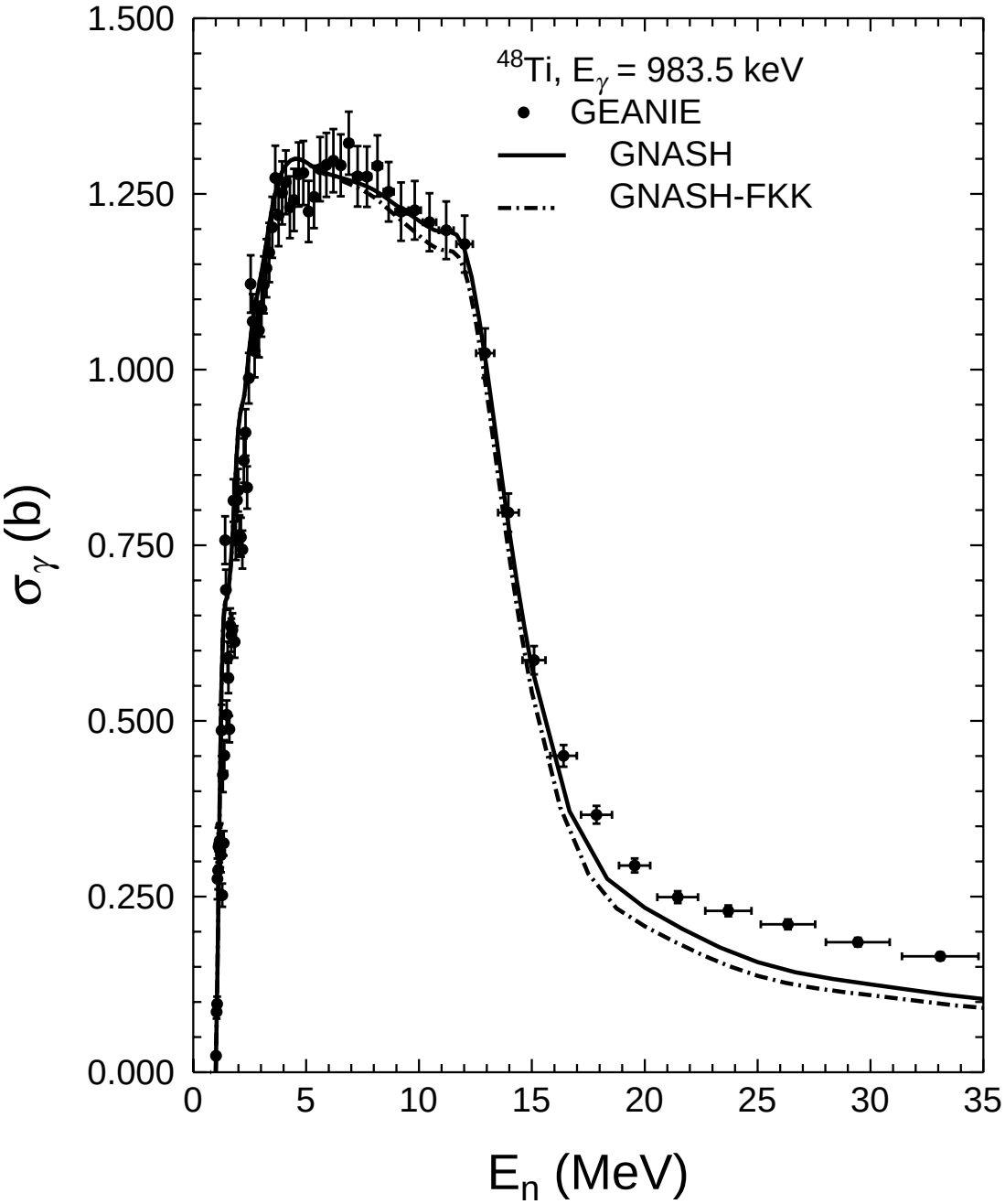

Figure 6.22: Partial cross section for $E_\gamma = 983$-keV transition between 2^+ to 0^+ in yrast band of ^{48}Ti. The experimental data compared with GNASH and GNASH-FKK calculations.

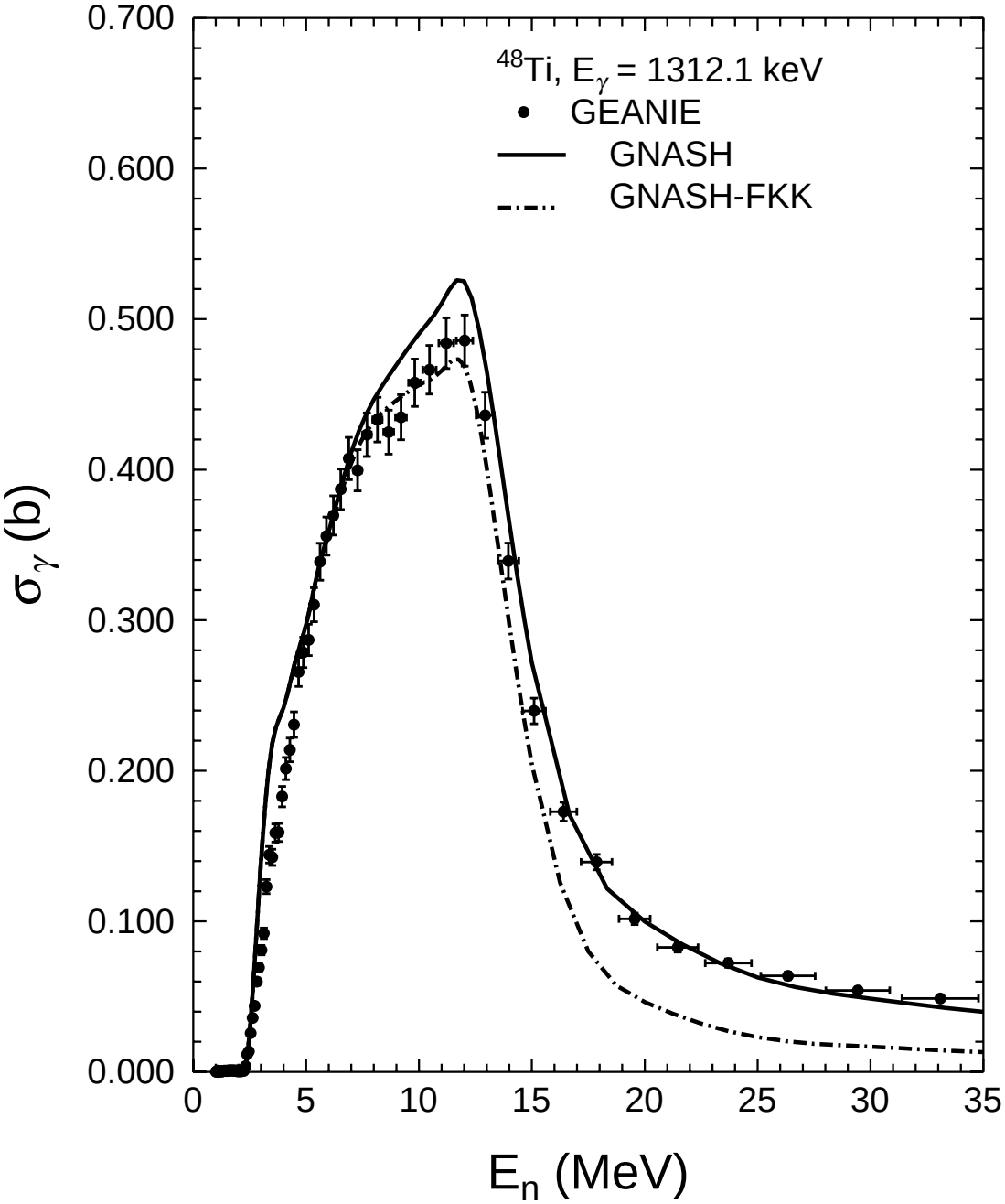

Figure 6.23: Partial cross section for E_γ = 1312-keV transition between 4^+ to 2^+ in yrast band of ^{48}Ti. The experimental data compared with GNASH and GNASH-FKK calculations.

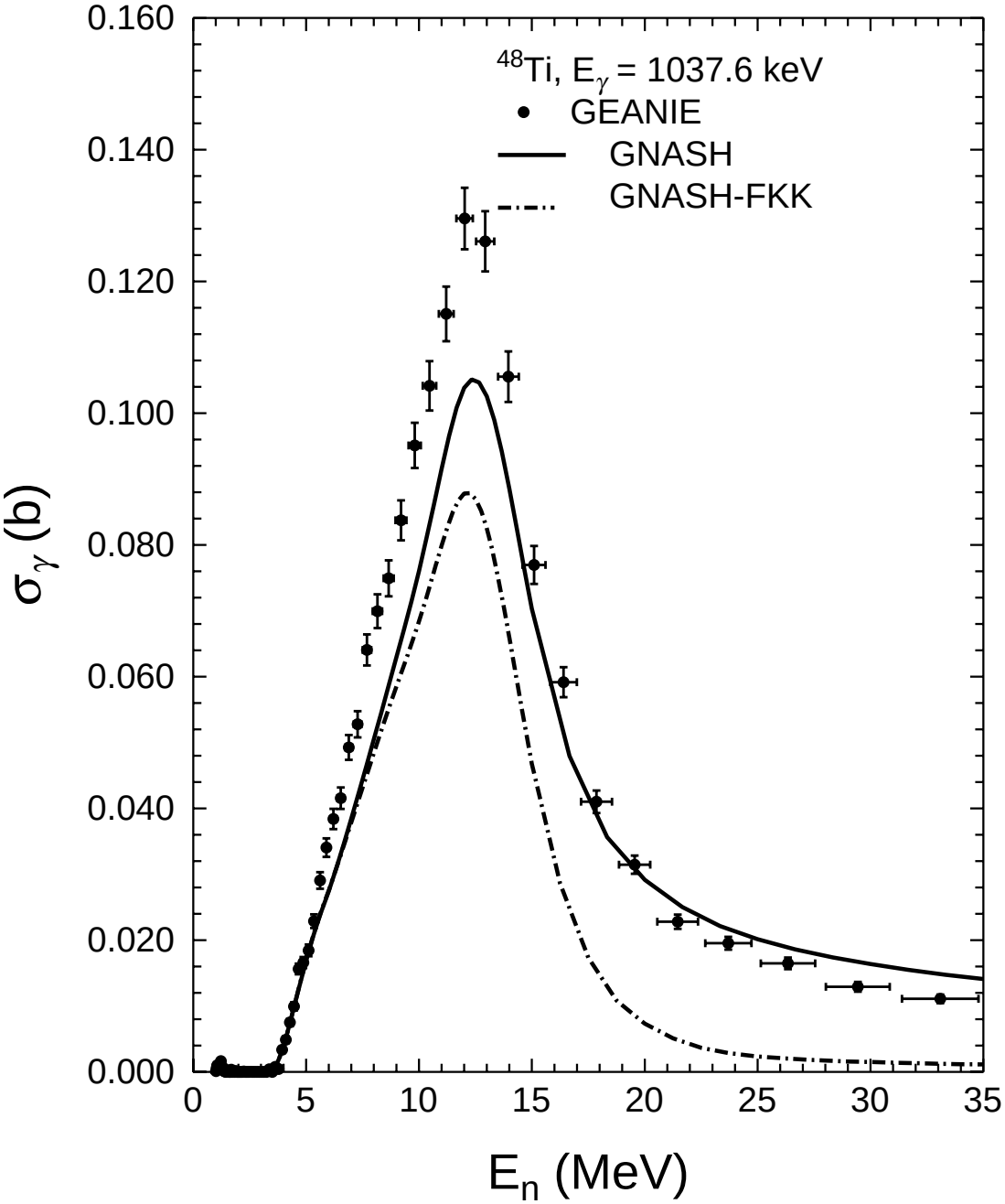

Figure 6.24: Partial cross section for E_γ = 1037-keV transition between 6^+ to 4^+ in yrast band of ^{48}Ti. The experimental data compared with GNASH and GNASH-FKK calculations.

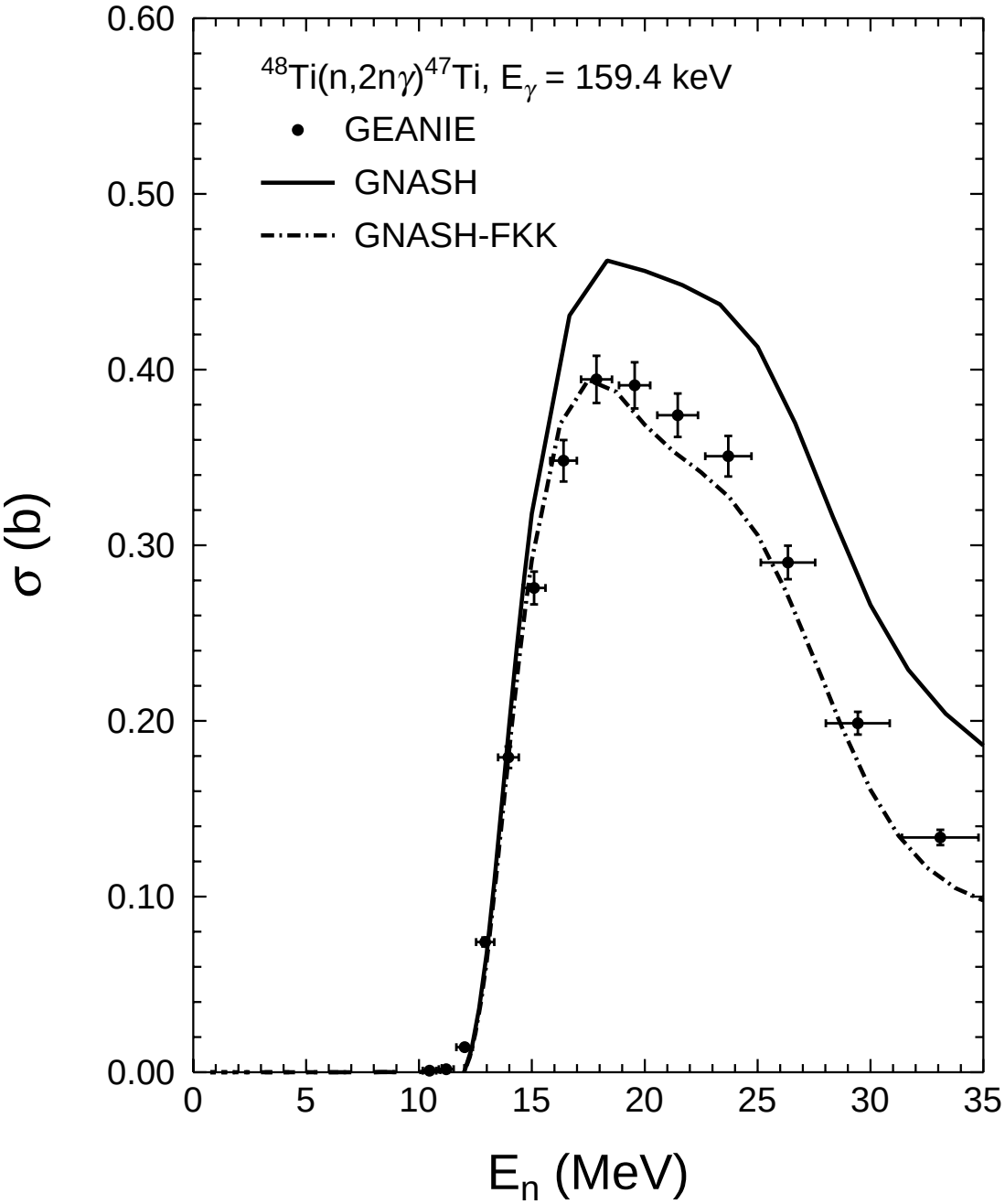

Figure 6.25: Partial cross section for yrast band transition in $(n, 2n\gamma)$ reaction. The experimental data compared with GNASH and GNASH-FKK calculations.

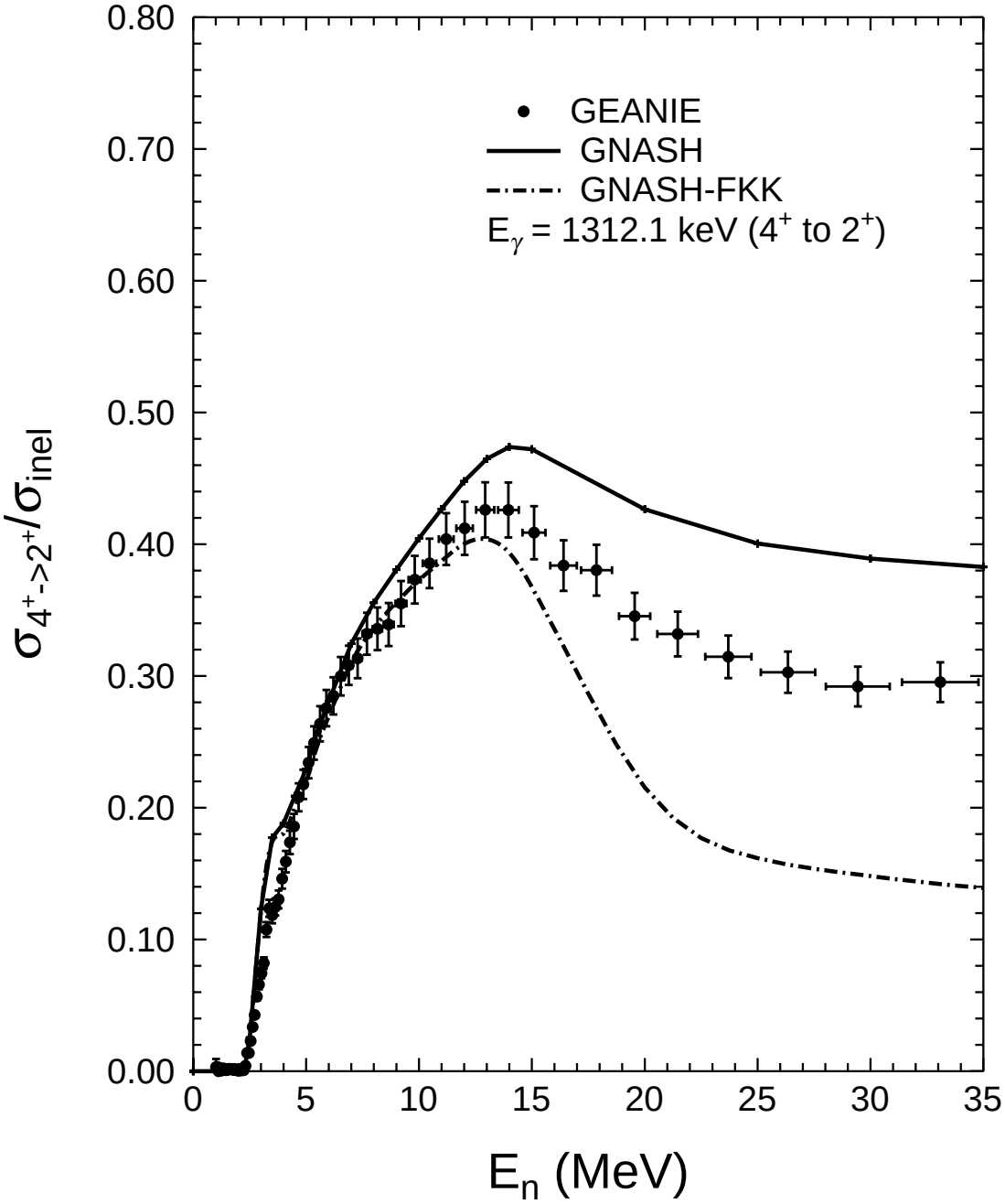

Figure 6.26: Ratio of the partial cross section for 4^+ to 2^+ yrast transition and the total inelastic cross section.

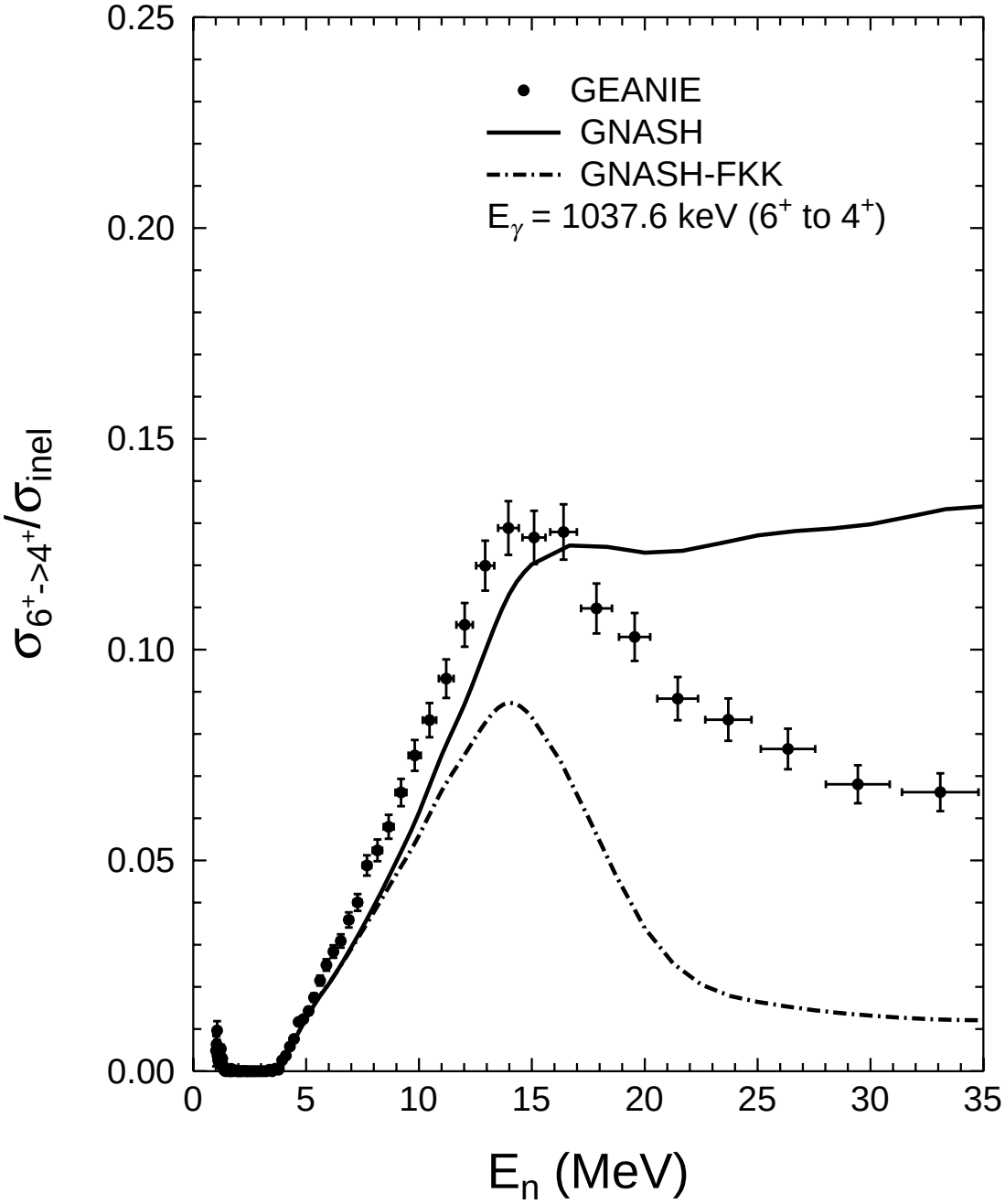

Figure 6.27: Ratio of the partial cross section for 6^+ to 4^+ yrast transition and the total inelastic cross section.

Chapter 7

Summary

7.1 Conclusion

Excitation functions of prompt γ rays produced in the n+^{48}Ti reaction have been measured using the GEANIE spectrometer at the LANSCE/WNR facility. The individual γ-ray yields have been converted to partial transition cross sections as a function of incident neutron energy by accounting for neutron flux, sample thickness, deadtime corrections, detector and fission chamber efficiencies, and internal conversion processes. The partial cross sections for γ rays decaying directly to the ground states of ^{48}Ti and ^{47}Ti have been summed separately to obtain lower limits of the ^{48}Ti(n,n$'\gamma$)^{48}Ti and ^{48}Ti(n,2nγ)^{47}Ti reaction cross sections, respectively. The lower limits for the ^{48}Ti(n,npγ)^{48}Sc and ^{48}Ti(n,n$\alpha\gamma$)^{45}Ca reaction cross sections have been also obtained based on the γ ray decaying directly to the ground state from the first excited state. These lower limits are combined with calculations of the STAPRE reaction code to deduce the channel cross sections for neutron energies between 1 to 20 MeV. Also the experimental data are presented for neutron energies up to 200 MeV. γ rays from a total of 13 different isotopes were observed and prominant partial γ-ray cross sections were extracted. These partial γ-ray cross sections are compared with the calculations of the GNASH reaction code.

The spin distribution of the preequilibrium process in ^{48}Ti + n reactions was cal-

culated for the first time with the quantum mechanical theory of Feshbach, Kerman, and Kooning (FKK). The FKK one-step process was included for the multistep direct (MSD) reaction to account for the preequilibrium effect and the spin cut-off parameters of residual system were estimated. The FKK spin distribution of preequilibrium was incorporated into GNASH calculation and the γ-ray production cross sections were calculated and compared with experimental data. The difference of including spin distribution with and without preequilibrium effects is found to be significant. The probability of γ transition from a high spin state is strongly suppressed because of the preequilibrium spin distribution.

The statistical properties of preequilibrium reactions are best studied for heavy nuclei far from shell closure where the number of nucleons interacting will be large, thus giving rise to sufficient single particle distributions. This will allow easy coupling of different angular momentum states which in turn will allow smoother calculated FKK spin distributions. More studies of preequilibrium reactions using heavier nuclei is therefore suggested.

Bibliography

[Akk90] J. M. Akkermans and A. J. Koning, Phys. Lett. **B 234**, 417 (1990).

[Aud95] G. Audi and A. H. Wapstra, Nucl. Phys. **A595**, 408 (1995).

[Avr95] M. Avrigeanu and V. Avrigeanu, "IPNE-Bucharest report", Technical Report NP-86-1995, 1995, http://www.nea.fr/abs/html/iaea0971.html.

[Axe62] P. Axel, Phys. Rev. **126**, 671 (1962).

[Bau02] R. Bauer, 2002, private communication.

[Bec71] F. D. Becchetti and G. W. Greenlees, in *Polarization Phenomena in Nuclear Reactions*, edited by H. H. Barschall and W. Haeberli, page 682, University of Wisconsin Press, Madison, 1971.

[Bec97] J. A. Becker and R. O. Nelson, Nucl. Phys. News Int. **7**, 11 (1997).

[Bel96] T. Belgya, G. Molnar, and S. W. Yates, Nucl. Phys. **A607**, 43 (1996).

[Ber63] H. W. Bertini, Phys. Rev. **131**, 1801 (1963).

[Bla79] J. M. Blatt and V. F. Weisskopf, *Theoretical Nuclear Physics*, Dover Publications, Inc., 1979.

[Bla96] M. Blann, Phys. Rev. **C54**, 1341 (1996).

[Boh36] N. Bohr, Nature **137**, 344 (1936).

[Boh75] A. G. Bohr and B. R. Mottelson, *Nuclear Structure*, volume II, Benjamin, London, 1975.

[Bon91] R. Bonetti, M. B. Chadwick, P. E. Hodgson, B. V. Carlson, and M. S. Hussein, Phys. Rep. **202(4)**, 171 (1991).

[Bri55] D. M. Brink, Ph.D. thesis, Oxford University, 1955.

[Bri86] J. F. Briesmeister, "A General Monte Carlo Code for Neutron and Photon Transport", Technical Report LA-7396-M-Rev.2, LANL, 1986.

[Car00] B. V. Carlson, in *Workshop on Nuclear Data and Nuclear Reactors: Physics, Design and Safety*, ICTP, Trieste, 2000.

[Cha89] M. B. Chadwick, Ph.D. thesis, Oxford University, 1989.

[Cha94a] M. B. Chadwick, P. G. Young, D. C. George, and Y. Watanabe, Phys. Rev. **C50**, 996 (1994).

[Cha94b] M. B. Chadwick, P. G. Young, P. Oblozinsky, and A. Marcinkowski, Phys. Rev. **C49**, R2885 (1994).

[Cli72] C. K. Cline, Nucl. Phys. **A 195**, 353 (1972).

[Coc94] C. Coceva, Nuovo Cimento **107 A**, 85 (1994).

[Dov72] C. B. Dover, R. H. Lemmer, and F. J. W. Hahne, Ann. of Phys. **70**, 458 (1972).

[end91] "Cross Section Evaluation Working Group", Technical Report BNL-NCS-17451 (ENDF-201), 1991.

[ens] Evaluated Nuclear Structure Data File, BNL, US Dept. of Energy, http://www.nndc.bnl.gov/nndc/ensdf.

[Fes80] H. Feshbach, A. K. Kerman, and S. Koonin, Ann. Phys. (NY) **125**, 429 (1980).

[Gad81] E. Gadioli, E. Gadioli-Erba, J. J. Hogan, and K. I. Burns, Z. Phys. **A 301**, 289 (1981).

[Gad92] E. Gadioli and P. E. Hodgson, *Pre-Equilibrium Nuclear Reactions*, Clarendon Press, Oxford, 1992.

[Gar00] P. E. Garrett et al., Phys. Rev. **C 62**, 054608 (2000).

[Gil65] A. Gilbert and A. G. W. Cameron, Can. J. Phys. **43**, 1446 (1965).

[Gri66] J. J. Griffin, Phys. Rev. Lett. **74**, 478 (1966).

[Her84] M. Herman, A. Marcinkowski, and K. Stankiewicz, Nucl. Phys. **A430**, 69 (1984).

[Hil03] S. Hilaire, C. Lagrange, and A. J. Koning, Ann. of Phys. **306**, 209 (2003).

[Hod97] P. E. Hodgson, E. Gadioli, and E. G. Erba, *Introductory Nuclear Physics*, Clarendon Press, Oxford, 1997.

[Hof75] H. M. Hofmann, J. Richert, J. W. Tepel, and H. A. Weidenmüller, Ann. of Phys. **90**, 403 (1975).

[Ign75] A. V. Ignatyuk, G. N. Smirenkin, and A. S. Toshin, Sov. J. Nucl. Phys. **21**, 255 (1975).

[Kad83] S. G. Kadmenskij, V. P. Markushev, and V. I. Furman, Sov. J. Nucl. Phys. **37**, 165 (1983).

[Kal74] C. Kalbach, "PRECO Program for Calculating Preequilibrium Particle Energy Spectra", Technical Report DRh-N/BE/74/3, Centre d'Etudes Nucleaires de Saclay Rapport Interne, 1974.

[Kal85] C. Kalbach, Phys. Rev. **C32**, 1157 (1985).

[Kaw98] T. Kawano, in *1997 Symposium on Nuclear Data, Nov., 27-28, 1997*, volume JAERI-Conf 98-003, page 312, JAERI, TOKAI, 1998.

[Kaw05] T. Kawano, 2005, private communication.

[Ker70] J. Kern, Nucl. Instr. Methods **79**, 233 (1970).

[Kon91] A. J. Koning and J. M. Akkermans, Ann. Phys. (N.Y.) **208**, 216 (1991).

[Kon03] A. J. Koning and J. P. Delaroche, Nucl. Phys. A **713**, 231 (2003).

[Kop89] J. Kopecky and M. Uhl, Phys. Rev. **C 41**, 1941 (1989).

[Lem76] O. Lemos, "Diffusion Elastique de Particules Alpha de 21 a 29.6 MeV sur des Noyaux de la Region Ti-Zn", Technical Report Series A, No. 136, Orsay report, 1976.

[Lis90] P. W. Lisowski, C. D. Bowman, G. J. Russell, and S. A. Wender, Nucl. Sci. Eng. **106**, 208 (1990).

[McN99] D. P. McNabb, "Uncertainty Budget and Efficiency Analysis for the ^{239}Pu(n,2nγ) Partial Reaction Cross-Section Measurements", Technical Report UCRL-ID-139906, LLNL, 1999.

[Mol61] P. A. Moldauer, Phys. Rev. **123**, 968 (1961).

[Mol76] P. A. Moldauer, Phys. Rev. **C14**, 764 (1976).

[Mol80] P. A. Moldauer, Nucl. Phys. **A 344**, 185 (1980).

[Mol95] P. Moller, J. R. Nix, W. D. Myers, and W. J. Swiatecki, Atomic Data and Nuclear Data Tables **59**, 185 (1995).

[Nel04] R. O. Nelson, in *Proceedings of the International Conference on Nuclear Data for Science and Technology*, American Institute of Physics, 2004, http://t16web.lanl.gov/nd2004/index.php.

[Nis88] H. Nishioka, H. A. Weidenmüller, and S. Yoshida, Ann. Phys. (NY). **183**, 166 (1988).

[nud] National Data Center, Information extracted from the NuDat database, http://www.nndc.bnl.gov/nudat2.

[Pos81] H. Postma, Phys. Rev. **C 24**, 2322 (1981).

[qto] T-2 Nuclear Information Service, LLNL, http://t2.lanl.gov/data/qtool.html.

[Rad95] D. C. Radford, Nucl. Instrum. Methods Phys. Res. **A361**, 297 (1995).

[Rau97] T. Rauscher, F. K. Thielemann, and K. L. Kratz, Phys. Rev. **C56**, 1613 (1997).

[Ray96] J. Raynal, in *Proceedings of the Specialists' Meeting on the Nucleon Nucleus Optical Model up to 200 MeV*, Bruyeres-le-Chatel, France, 13-15 November, 1996, http://www.nea.fr/html/science/om200/raynal.pdf.

[rip98] "Handbook for calculations of nuclear reaction data", Reference Input Parameter Library, 1998, IAEA-TECDOC-1034.

[Tam82] T. Tamura, T. Udagawa, and H. Lenske, Phys. Rev. **C26**, 379 (1982).

[Tav01] E. Tavucku et al., Phys. Rev. **C 64**, 054614 (2001).

[Uhl76] M. Uhl and B. Strohmaier, "IRK-Vienna Report", Technical Report IRK-76/01, 1976.

[Von94] H. Vonach et al., Phys. Rev. **C 50**, 1952 (1994).

[Wen93] S. A. Wender et al., Nucl. Instrum. Methods Phys. Res. A **336**, 226 (1993).

[Wes93] H. I. West, R. G. Lanier, and M. G. Mustafa, "Excitation Functions for the Nuclear Reactions on Titanium Leading to the Production of ^{48}V, ^{44}Sc, and ^{47}Sc, by Proton, Deuteron and Triton Irradiations at 0-35 MeV", Technical Report UCRL-ID-223882, LLNL, 1993.

[Wil70] F. C. J. Williams, Phys. Lett. **31B**, 184 (1970).

[Wil71] F. C. Williams, Nucl. Phys. **A166**, 231 (1971).

[You] W. Younes, "The XGAM peak-fitting program", Manuscript in preparation.

[You99] P. G. Young, E. D. Arthur, and M. B. Chadwick, in *Nuclear Reaction Data and Nuclear Reactors - Physics, Design, and Safety - Vol.1*, edited by A. Gandini and G. Reffo, pages 227–404, World Scientific, Singapore, 1999.

[You00] W. Younes et al., "The ^{235}U(n,2nγ) Yrast Partial Gamma-Ray Cross Sections: A Report on the 1998 and 1999 GEANIE Data and Analysis Techniques", Technical Report UCRL-ID-140313, LLNL, 2000.

[You01] W. Younes et al., "Transition from asymmetric to symmetric fission in the ^{235}U(n, f) reaction", Phys. Rev. C **64**, 054613 (2001).

[You03] W. Younes et al., "The analysis of ^{75}As$(n, xn\gamma)$ Cross Sections", Technical Report UCRL-ID-154061, LLNL, 2003.

Appendix A

Partial γ ray cross sections

This appendix presents the partial cross sections of the individual γ rays included in the estimation of the reaction channel cross sections discussed in the Section 6.1.

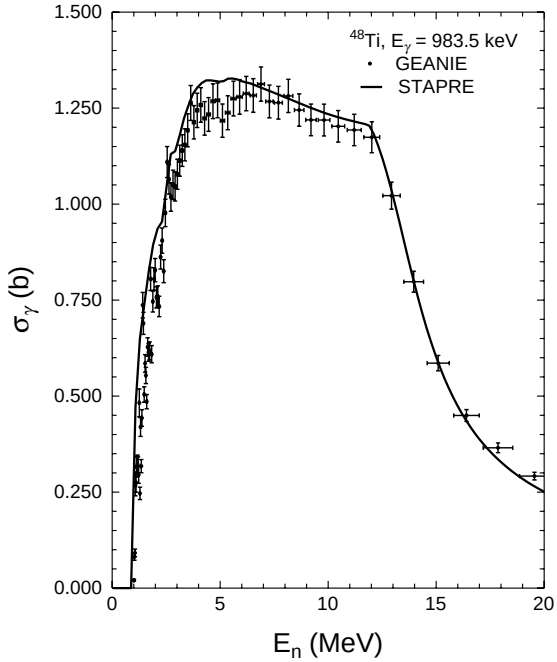

Figure A.1: Partial cross section for the E_γ = 983.5-keV transition in ^{48}Ti, extracted from coax data. The data are compared to a STAPRE prediction.

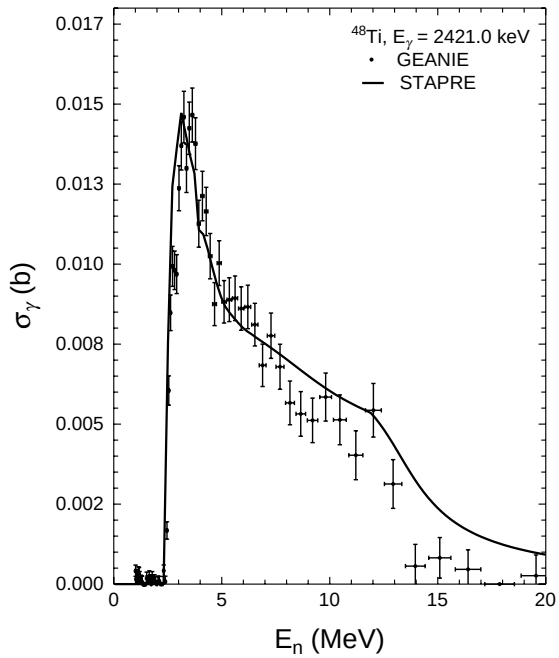

Figure A.2: Partial cross section for the E_γ = 2421.0-keV transition in ^{48}Ti, extracted from coax data. The data are compared to a STAPRE prediction.

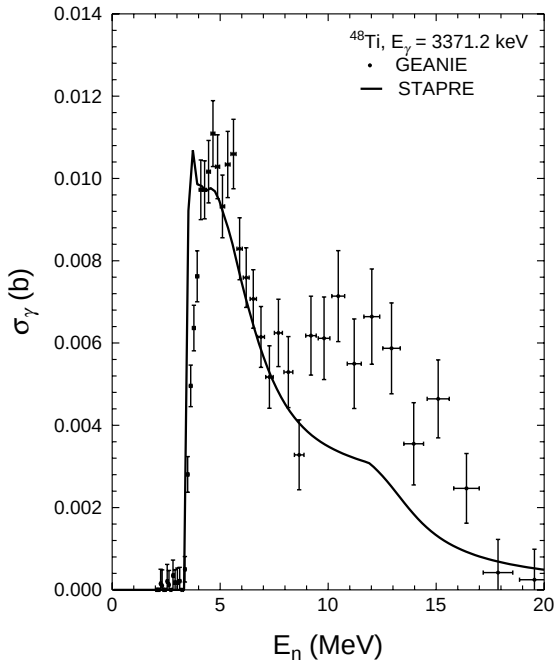

Figure A.3: Partial cross section for the E_γ = 3371.2-keV transition in ^{48}Ti, extracted from coax data. The data are compared to a STAPRE prediction.

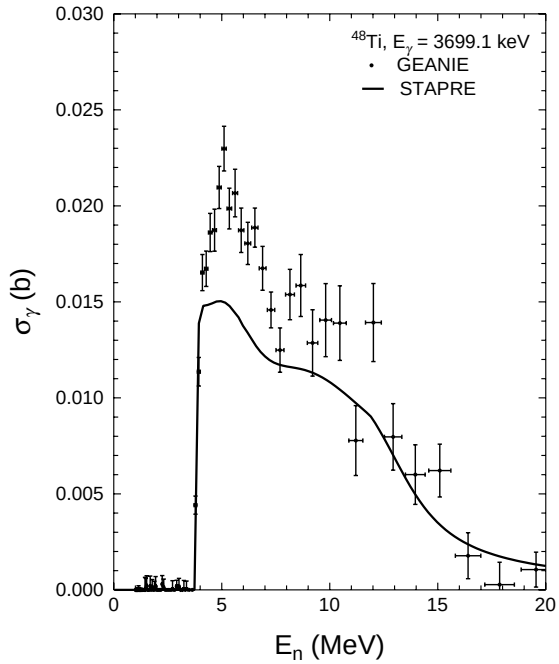

Figure A.4: Partial cross section for the E_γ = 3699.1-keV transition in ^{48}Ti, extracted from coax data. The data are compared to a STAPRE prediction.

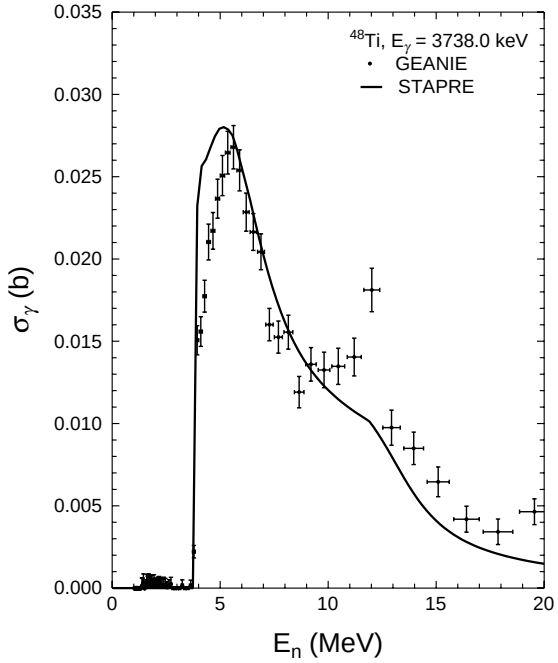

Figure A.5: Partial cross section for the E_γ = 3738.1-keV transition in ^{48}Ti, extracted from coax data. The data are compared to a STAPRE prediction.

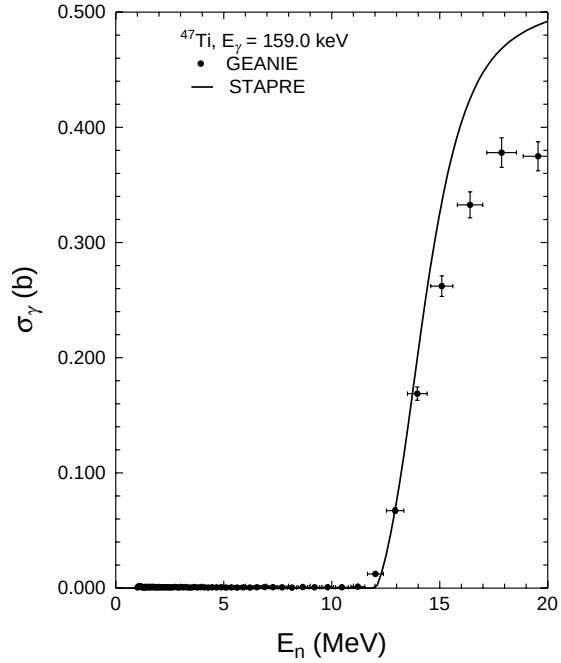

Figure A.6: Partial cross section for the E_γ = 159.4-keV transition in ^{47}Ti, extracted from planar data. The data are compared to a STAPRE prediction.

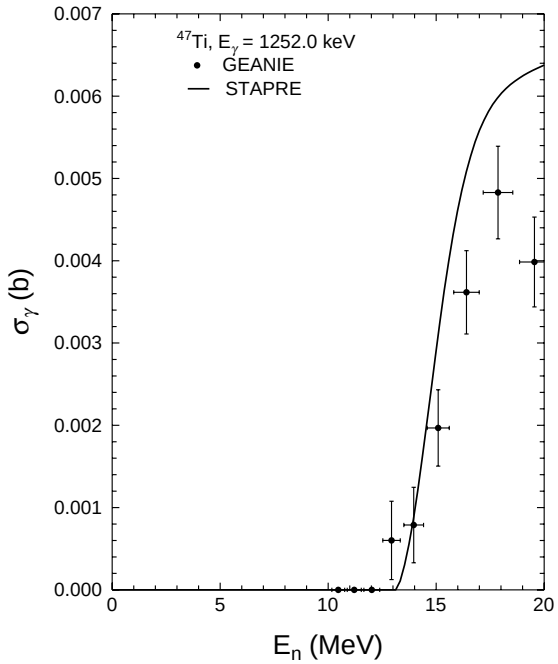

Figure A.7: Partial cross section for the E_γ = 1251.5-keV transition in ^{47}Ti, extracted from coax data. The data are compared to a STAPRE prediction.

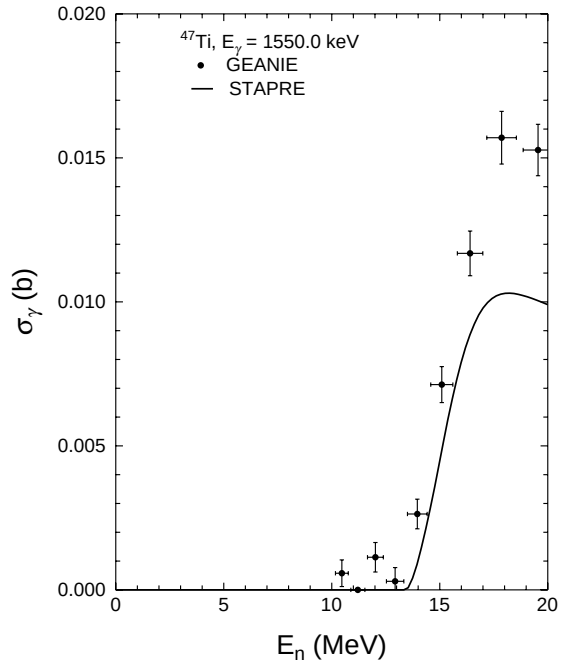

Figure A.8: Partial cross section for the E_γ = 1549.9-keV transition in ^{47}Ti, extracted from coax data. The data are compared to a STAPRE prediction.

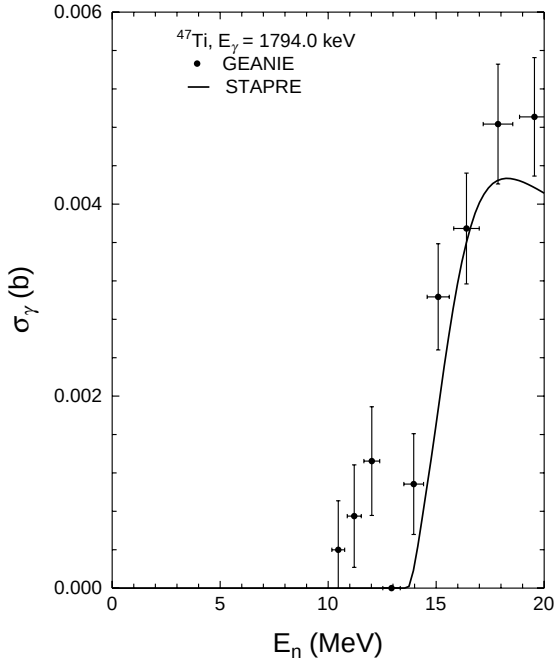

Figure A.9: Partial cross section for the E_γ = 1793.9-keV transition in ^{47}Ti, extracted from coax data. The data are compared to a STAPRE prediction.

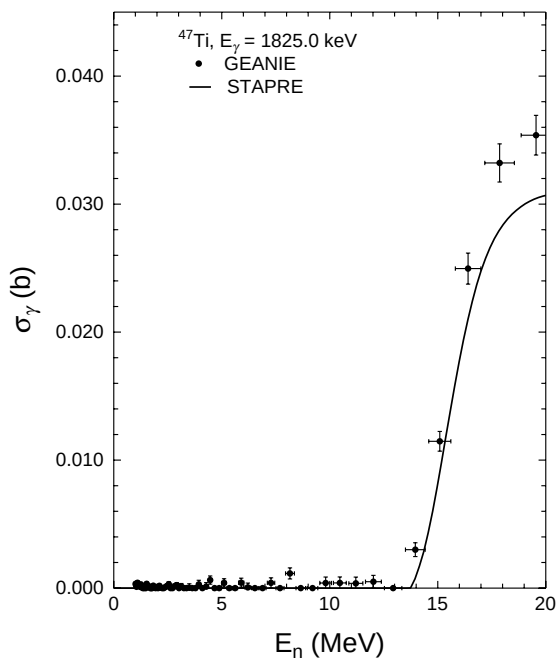

Figure A.10: Partial cross section for the E_γ = 1825.1-keV transition in ^{47}Ti, extracted from coax data. The data are compared to a STAPRE prediction.

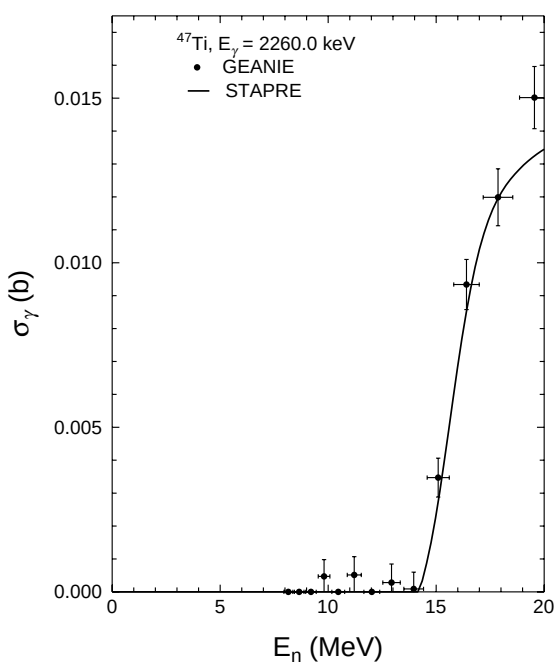

Figure A.11: Partial cross section for the E_γ = 2259.3-keV transition in ^{47}Ti, extracted from coax data. The data are compared to a STAPRE prediction.

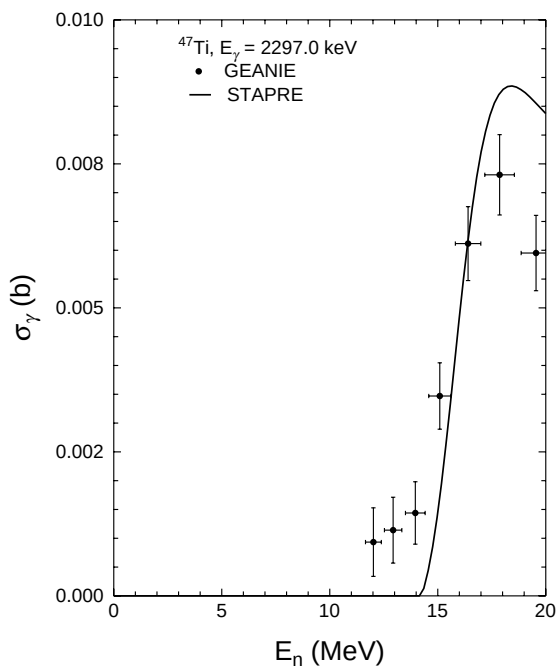

Figure A.12: Partial cross section for the E_γ = 2297.0-keV transition in ^{47}Ti, extracted from coax data. The data are compared to a STAPRE prediction.

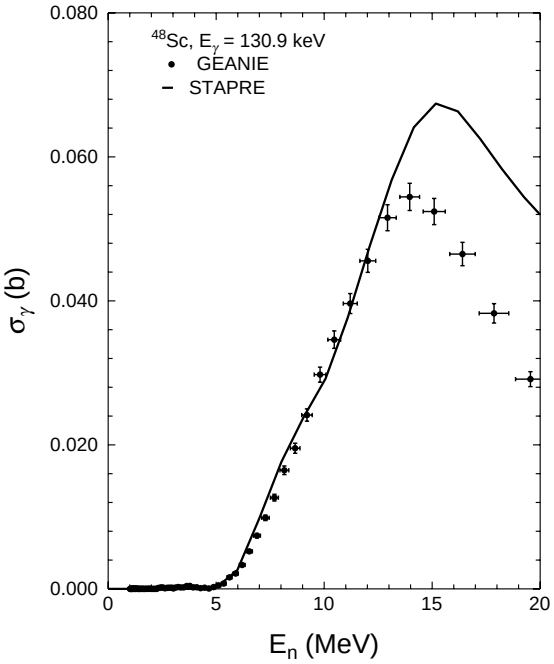

Figure A.13: Partial cross section for the $E_\gamma = 130.9$-keV transition in ^{48}Sc, extracted from planar data. The data are compared to a STAPRE prediction.

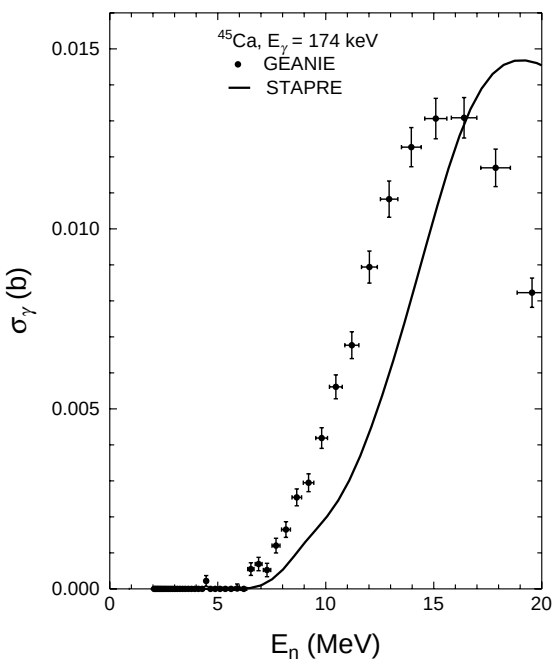

Figure A.14: Partial cross section for the $E_\gamma = 174.3$-keV transition in ^{45}Ca, extracted from planar data. The data are compared to a STAPRE prediction.